Tectonic and Climatic Controls on Continental River Systems

by

Samuel L. Goldberg

A.B. Earth and Planetary Sciences, Harvard University, 2016

Submitted to the Department of Earth, Atmospheric, and Planetary Sciences
in partial fulfillment of the requirements for the degree of

Doctor of Philosophy

at the

Massachusetts Institute of Technology

September 2021

Author .....
Department of Earth, Atmospheric, and Planetary Sciences
August 12, 2021

Certified by: .....
J. Taylor Perron
Professor of Geology
Thesis Supervisor

Accepted by: .....
Robert D. van der Hilst
Schlumberger Professor of Earth and Planetary Sciences
Head of Department

Tectonic and Climatic Controls on Continental River Systems

by

Samuel L. Goldberg

Submitted to the Department of Earth, Atmospheric, and Planetary Sciences
on August 12, 2021,
in Partial Fulfillment of the Requirements for the Degree of
Doctor of Philosophy in Geology

ABSTRACT

Erosion by rivers is the dominant driver of topographic change over much of Earth's terrestrial surface, and sets the pace of change for other landscape processes. In this thesis, I explore the complexities of landscapes evolving under fluvial processes. I address questions of how rivers respond to climate, geologic substrate, and tectonics across scales, how landscape disequilibrium results from changing tectonic and climatic forces, and implications of landscape evolution for past human settlement. In the first chapter, I use a process model of river erosion that includes sediment transport feedbacks to show that climate controls the degree to which rock type affects erosion through transport limitations, with arid regions showing a much weaker dependence on rock type than humid regions. This complexity is not captured by typical models of river erosion. In the second chapter, I study the unusual case of the Rio Casiquiare, an ongoing river capture of the Amazon River from the Rio Orinoco. I use this case study to show that large lowland rivers with slope asymmetry across drainage divides reorganize their planform geometry towards a more equilibrated state, and in doing so can create perennial interbasin connections for centuries or longer. In the third chapter, I show that large lowland Amazon rivers have been quickly responsive to cyclical Quaternary climate changes, and as a result have repeatedly incised and aggraded with successive wettings and dryings of the region. In the fourth chapter, I use remote-sensing imagery and machine-learning classification to identify spatial patterns and distributions of ancient settlements, and find that they are almost universally located at the bluff edge at the interface between uplands and floodplains; this is an example of the ways in which geologic and environmental history can influence human society. These studies advance our knowledge of landscape evolution towards a more realistic understanding of the complexities of the natural world and its constant change.

Thesis Supervisor: J. Taylor Perron
Title: Professor of Geology

ACKNOWLEDGMENTS

All of my thesis chapters are the result of fruitful collaboration with colleagues, in addition to my thesis advisor J. Taylor Perron who advised me on all chapters. Chapters 1 and 2 were written with Maya F. Stokes, with Chapter 2 an equal collaboration. Chapter 3 benefitted from first-hand observations of the Amazon by Morgan J. Schmidt. Chapter 4 reflects extensive field research by Morgan Schmidt, Michael Heckenberger, the Kuikuro Assocation, and colleagues, as well as contributions by Luiz Leal Gomez and Joshua Himmelstein towards the classification algorithms.

In addition to the chapters presented here, I also was fortunate to carry out a Paleozoic paleoclimate study with Kristin Bergmann, Seth Finnegan, and Ted Present. I am grateful to Kristin and the rest of the Bergmann lab for welcoming me into their group and allowing me to pretend to be a deep-time geologist.

My Ph.D. was primarily funded by the MIT Praecis Presidential Fellowship, EAPS Patrick Hurley Fellowship, and the NASA Earth and Space Science Fellowship. I received additional support from Saudi Aramco, US Army Research Office, and the MIT-Air Force AI Accelerator. The Amazon project out of which grew Chapters 3 and 4 was funded by MIT Abdul Latif Jameel Water and Food Systems Lab (J-WAFS).

I thank Maya Stokes and Marjorie Cantine for being my office-mates until Covid scattered us, for letting me be your field assistants all along the Appalachian orogeny, and for showing me the path through grad school. I also thank the other members of the Perron group past and present who were my geomorphology community these past five years.

I am grateful to my thesis committee (Taylor Perron, Kristin Bergmann, Leigh Royden, Dan Rothman, and Greg Tucker) for their insightful critiques and helpful guidance over the course of my Ph.D., and for the refreshing perspectives they offered on my work.

Finally, I thank my wife Kate Carter and the rest of my family for getting me to this point and supporting me along the way.

TABLE OF CONTENTS

Introduction

Earth's terrestrial landscape is shaped by the interplay among tectonic uplift, erosion, and deposition. Rivers are governed by their climatic, geologic, and tectonic context, which combine to create the observable landscape. The natural world is infinitely complex and cannot be fully described by any model; there are many complexities of landscape evolution that are readily apparent from natural systems but are not captured by existing models. In this thesis, I explore such examples, relating to the interactions among different factors influence bedrock river incision, the mechanisms by which large rivers rearrange their planform geometry, the response of continent-scale river systems to cyclical climate change, and the influence of landscape history on human society.

In the first chapter, I investigate the implications of a river incision model that incorporates feedbacks of sediment transport in erosional rivers that are commonly not considered in such models. In particular, I focus on the sediment cover effect, in which deposits of sediment shield river beds from erosion, which acts as a negative feedback on erosion. I show that this feedback can mute the influence of rock type on erosion rate and topography, and is generally stronger in arid regions than humid regions. I test this prediction against topography in contrasting climatic settings, and find a strong dependence of topography on rock type in humid regions but a much weaker dependence in arid regions. This finding consistent with a transition towards transport-limited behavior with increasing aridity, such that climate modulates the effect of rock type on river incision. Climate and rock type are commonly thought to be two of the major factors influencing bedrock erosion; this example shows that these two factors can interact in complex, non-linear ways that are not captured by the simple stream power erosion law.

In the second chapter, I examine the unusual example of the Rio Casiquiare, a river in South America that originates as a distributary of the Rio Orinoco, then flows as a tributary of the Rio Negro into the Amazon basin, thus flowing across a drainage divide and forming a perennial hydrologic connection between two of the largest river basins on Earth. I use a combination of topographic analysis and field measurements from the US Army to show that this bifurcation is unstable, and that the Rio Casiquiare will eventually completely divert the flow of the upper Rio Orinoco into the Amazon basin due to its steeper slope. This system at the present-day represents an ongoing, as yet incomplete river capture. I further place this capture in the context of other past drainage rearrangements, showing that it is part of a coherent trend of northward expansion of the Amazon basin driven by the topographic disequilibrium engendered by the rise of the Andes and the integration of the transcontinental Amazon River. This case study illuminates the mechanisms by which large river systems reorganize their planform geometry towards greater topographic equilibrium, where adjacent river basins feature equal slopes across drainage divides. This process can create perennial interbasin hydrologic connections for at least centuries, with hydrologic and biogeographic implications.

In the third chapter, I continue my study of the Amazon basin, but focusing on climatically-driven disequilibrium rather than tectonics-induced changes. Lowland alluvial rivers such as the large Amazonian rivers are commonly modeled by the concept of the equilibrium "graded profile," in which river slope and discharge everywhere are such that sediment transport capacity exactly matches the upstream sediment supply, in this case from the rapidly eroding Andes mountains. However, the Amazon basin received far less precipitation during the last glacial phase than today, and evidence suggests that the pattern of dry glacials and wet interglacials has persisted for at least a million years. As a result, the rivers of the Amazon have

experienced repeated changes to runoff and discharge, and potentially to sediment supply as well, meaning that the concept of a steady-state graded profile is likely overly simplistic. I use a simple theoretical model to estimate a response timescale for alluvial rivers from empirical measurements, which I apply to a set of gauging stations throughout the Amazon basin. I find that many of the Amazon rivers have response timescales less than the 100,000 year period of glacial cycles, indicating that they can keep up with cyclical climate changes, and as a result have repeatedly aggraded and incised towards a changing equilibrium state. This high responsivity is in contrast to other large rivers, and is the result of the exceptionally high runoff and discharge of the Amazon basin. The present-day rivers have incised by several tens of meters since maximum aggradation, creating high and abrupt river terraces in an otherwise low-relief landscape. These bluffs cleanly separate seasonally inundated floodplains from emergent uplands, despite annual stage variation of 5-10 m.

In my final chapter, I explore the implications of the resulting landscape structure for human society and past human settlement in the Amazon. Amazonian dark earth (ADE) is anomalously fertile, carbon-rich soil found in the Amazon in close association with pre-Columbian archaeological artifacts, indicating human creation. It is thought that ADE enabled large, complex societies that would otherwise be beyond the carrying capacity of the naturally occurring nutrient-poor tropical soils. Deposits of ADE are typically found and studied by labor-intensive fieldwork and excavation. As a result, compilations of known ADE locations likely exhibit substantial sampling biases, hindering systematic analysis. I use globally available satellite remote sensing imagery to detect and identify ADE deposits through its signature in the tree canopy. Using ground-truthed training data from field measurements and a machine-learning classifier, I produce a land-cover classification map of the Xingu Indigenous Territory that

highlights predicted ADE locations. Consistent with local field investigations, I find that ADE deposits are overwhelmingly located on uplands along the bluff edges adjacent to the floodplains, indicating a strong role for landscape structure in controlling locations of human settlement. I also use the map of predicted ADE to estimate the total area of ADE deposits and the carbon sequestration potential of these soils as a result of past human activities.

These studies each investigate an example of the complexities by which landscapes evolve in the dynamic Earth system, and advance our process understanding of how river systems to environmental conditions and environmental change beyond existing models. With each additional layer of complexity, we move towards a more complete understanding of the processes by which Earth's surface has attained its present form and will continue to change in the future.

References

Gilbert, G. K. (1877). *Geology of the Henry Mountains*. Washington, D.C.

Hack, J. T. (1957). Studies of longitudinal stream profiles in Virginia and Maryland. *USGS Professional Paper*, *249*(B), 97.

Hack, J. T. (1973). Stream-profile analysis and the stream-gradient index. *Journal of Research of the US Geological Survey*, *1*(4), 421–429.

Howard, A. D., & Kerby, G. (1983). Channel changes in badlands. *Geological Society of America Bulletin*, *94*, 739–752.

Leopold, L. B., & Maddock, T. (1953). The Hydraulic Geometry of Stream Channels and Some Physiographic Implications. *Geological Survey Professional Paper*, *252*, 1–57.

Montgomery, D. R., & Dietrich, W. E. (1992). Channel Initiation and the Problem of Landscape Scale. *Science*, *255*(5046), 826–830. https://doi.org/10.1126/science.255.5046.826

Snyder, N. P., Whipple, K. X., Tucker, G. E., & Merritts, D. J. (2000). Landscape response to tectonic forcing: Digital elevation model analysis of stream profiles in the Mendocino triple junction region, northern California. *Geological Society of America Bulletin*, *112*(8), 1250–1263.

1. Climate modulates the influence of rock type on bedrock river incision

Abstract

Contrary to the common assumption that rock type is a primary control on landscape evolution. tock type appears to influence topography strongly in some landscapes but only weakly in others. We show that this can result from differences in climate. Models of bedrock river incision predict a negative feedback in which faster erosion produces a higher sediment load that covers the bed and inhibits erosion. This feedback should be stronger in arid settings, where rivers struggle to convey their sediment load. We therefore predict that the ability of rivers in arid regions to erode bedrock depends mainly on how much of the bed they can expose through sediment transport rather than on rock properties. We test this prediction with numerical simulations and with topographic analysis of the Oregon Coast Range, Nevada Basin and Range, and Appalachian Mountains as case studies in contrasting climatic settings. We find a strong dependence of topography on lithology in humid settings, with basins in igneous or metamorphic rocks systematically and significantly steeper than those in sedimentary rocks. Conversely, in an arid setting we find a much weaker dependence of topography on rock type. This difference is consistent with our theory and suggests that climate controls the extent to which rock type influences erosion and topography. The sediment cover effect may thus explain the unclear relationship between rock type and erosion rate in global data compilations.

1.1. Introduction

Bedrock erosion by rivers is the main process that sculpts topography on much of Earth's unglaciated land surface (1). Three major factors governing river erosion are the topographic relief built by tectonics, which sets a river channel's slope; climate and runoff, which govern river discharge; and the mechanical strength of the bedrock being eroded (2–10). However, the

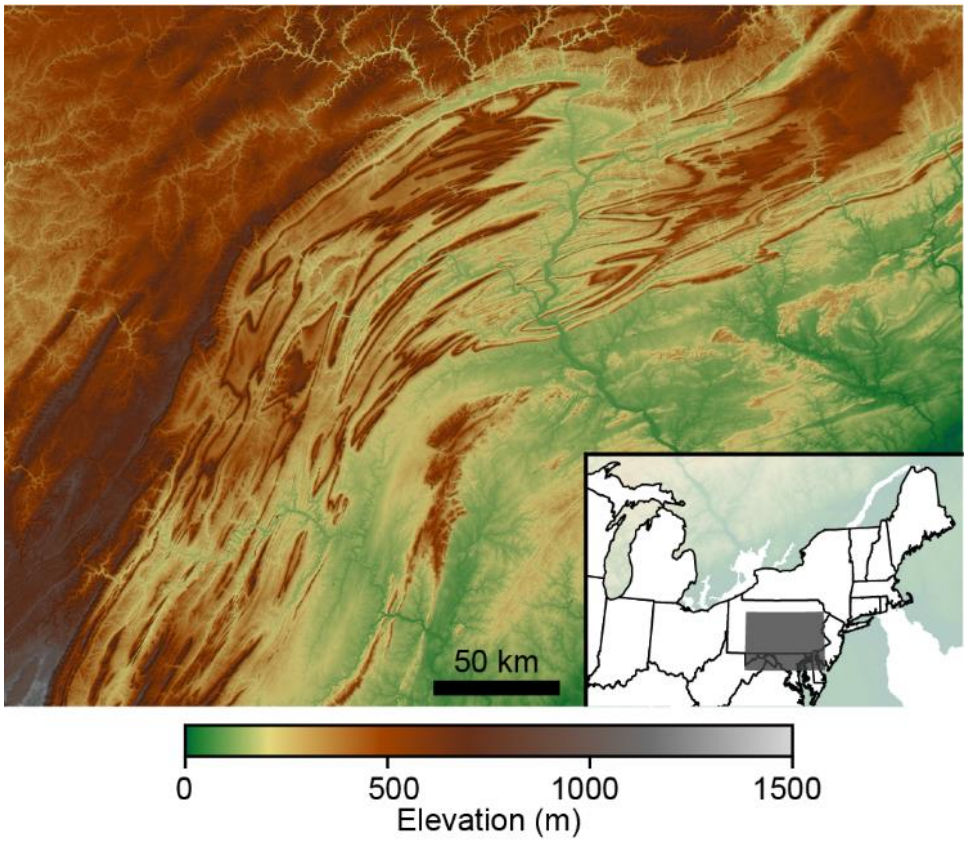

Figure 1.1: Color-shaded relief map of the Appalachian Valley and Ridge province in Pennsylvania, US (see inset for location). The linear ridges and valleys coincide with alternating beds of siliciclastic and carbonate rocks that have different erodibilities.

relative importance of these factors is debated. The effect of lithology (rock type and properties)is apparent in landscapes such as the Appalachian Valley and Ridge province, where contrasting rock units create steep ridges in less erodible units and gentle valleys in more erodible units (Figure 1.1) (11). This topographic imprint of lithologic heterogeneity emerges from the slope dependence of erosion rate. For two river basins of differing substrates to erode at the same rate, the basin with more resistant rock must be steeper. However, other landscapes, such as the Colorado River system in Utah and Arizona, show no clear relationship between channel slope and rock type (12), and global compilations generally do not show a clear trend (13, 14).

Erosional rivers are commonly divided into two regimes – detachment-limited, in which the river's ability to erode is limited by the ability to detach material from bedrock by mechanisms such as abrasion or plucking, and transport-limited, in which the river's ability to erode depends on its ability to entrain and transport the eroded material as sediment (15). However, most natural river systems in erosional environments display characteristics of both end-member behaviors (15, 16). Channel beds typically exhibit patches of both sediment and bare bedrock, indicating that the transport, entrainment, and deposition of sediment likely exerts an influence on bedrock erosion in most natural channels.

In this study, we explore the relative importance of climate and rock type in determining a river's ability to erode bedrock. We focus on the implications of a fluvial incision model that incorporates sediment transport feedbacks, allowing for both detachment- and transport-limited behavior as well as transitional behavior in which both processes play limiting roles. We use a combination of theory, numerical modeling, and topographic analysis to assess how sediment transport feedbacks affect the importance of rock type for bedrock incision and topography in humid and arid regions.

1.2. Theoretical model for fluvial erosion and sediment transport

Deposits of sediment on the bed of an erosional river shield the bedrock from erosion. This cover effect can create a negative feedback on bedrock erosion through interactions among erosion rate, sediment supply, and sediment cover (2, 17–20) (Figure 1.2). Specifically, an increase in erosion rate causes an increase in the sediment flux from upstream, which increases the bed sediment cover, which in turn acts to decrease the erosion rate. When the bed is mostly shielded by sediment, small changes in sediment transport can cause large relative changes in the

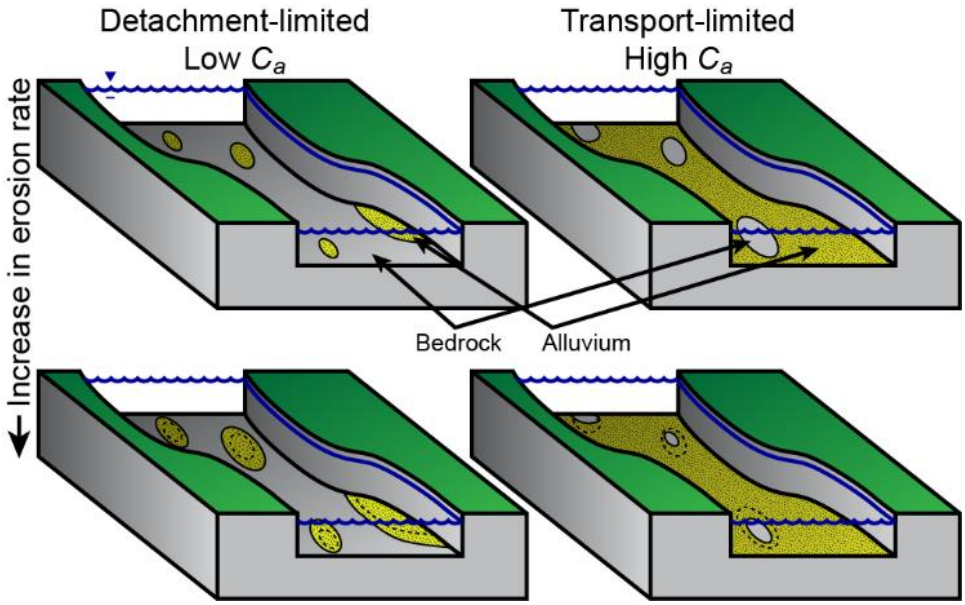

Figure 1.2: Conceptual diagram illustrating sediment transport feedbacks on erosion rate through sediment cover. Yellow areas represent sediment cover and gray areas represent bedrock. In the detachment-limited case (left side), most of the bedrock is exposed and the change in exposed bedrock area with an increased erosion rate (and therefore increased sediment supply) is comparatively small. In the transport-limited case (right side), most of the bedrock is covered and an increase in erosion rate and sediment supply causes a large fractional change in the area of bedrock exposed.

amount of bedrock exposed, making the feedback especially strong. In this scenario, erosion of the bedrock substrate is largely transport-limited, depending primarily on the degree of bed exposure and the river's ability to transport away the eroded material, rather than on its ability to detach material from the bed. As an implication of this feedback, we hypothesize that erosion rate is largely insensitive to rock type in transport-limited channels, as long as transport capacity does not depend strongly on lithology. Conversely, when most of the bedrock is exposed on the riverbed, the sediment cover feedback is weaker and erosion is largely detachment-limited, allowing greater influence of rock type.

We quantify these processes and feedbacks with a modified version of the common stream power erosion law (5, 6), to which we add an additional term that represents how sediment cover inhibits erosion (2, 18):

$$E = K_r Q_w^m S^n (1 - C_a). \quad (1)$$

In this equation, E represents the erosion rate of a river channel [L/T], Q_w is the volumetric water discharge [L^3/T], S is the channel slope [-], C_a is the areal fraction of the bed covered by sediment [-], and m and n are exponents, typically with the ratio $m/n \approx 0.5$. K_r is the rock erodibility coefficient [L^{1-3m}/T^{1-m}], reflecting material properties of the bedrock, channel geometry, hydraulic flow resistance, and erosional processes. The term $1 - C_a$ implies that only the fraction of the bedrock surface exposed to the flow can erode at any one time (e.g. (2, 18)).

Several models have been proposed to relate the sediment cover fraction C_a to sediment flux or thickness; we consider three of these models (2, 17, 18) (see Materials and Methods). Importantly, all three of these models feature an increase in sediment cover with increasing sediment flux, providing a negative feedback on erosion (Figure 1.2). In some cases, low sediment flux can inhibit erosion due to a lack of material to abrade the bed (the "tools effect") (2, 19), such that sediment flux acts as a positive feedback on erosion. Although our model does not account for this positive feedback, the tools effect is only dominant if sediment flux is much less than transport capacity. Such rivers are in the detachment-limited regime and thus their erosion rates will depend strongly on rock properties and they will not exhibit the effects of transport limitation we model. Moreover, most natural river systems are probably cover-limited rather than tools-limited (19). Thus, the negative feedback we model is likely relevant to the majority of Earth's rivers.

By substituting expressions for sediment transport as a function of discharge and slope into the sediment cover models and relating the water discharge to the upstream drainage area A [L^2] (Materials and Methods), we show how each of these models for C_a can be combined with the stream power erosion law to yield a simplified erosion law,

$$E = K_{\text{eff}} A^m S^n, \quad (2)$$

in which the effective erodibility coefficient K_{eff} incorporates all the parameters and processes that relate a channel's erosion rate to its drainage area and slope. This coefficient thus encodes rock properties, channel geometry, the runoff ratio *r* relating discharge to drainage area, the erosional processes that influence the intrinsic erodibility K_r, and the sediment transport processes that govern the degree of sediment cover. Each of the three models for sediment cover yields a corresponding expression for K_{eff} in terms of other model parameters (Materials and Methods), but all three expressions for K_{eff} predict a continuous transition from detachment-limited to transport-limited river incision as sediment cover increases. Any negative feedback between sediment flux and erosion rate will produce this spectrum of behavior; the details of the sediment cover model are not important. This continuum can be quantified with a dimensionless number $N = \tau_T/\tau_D$, defined as the ratio of a transport timescale τ_T to a detachment timescale τ_D. This number describes the relative strength of transport limitation; the exact form depends on the particular model for sediment cover (see Materials and Methods).

In the end-member case of detachment-limited incision, sediment flux is far less than transport capacity and $\tau_T \ll \tau_D$, so the river can efficiently transport away eroded sediment. As a result, sediment cover in this scenario is negligible, leaving most of the bed exposed to erosion, and the effective erodibility depends on the strength of the bedrock and the runoff (*r*), defined as the discharge per unit drainage area [L/T]: $K_{\text{eff}} \approx K_r r^m$. This dependence of erosion on lithology explains Valley and Ridge-style topography (Figure 1.1). Conditions that lead to detachment-limited behavior are those that favor sediment transport relative to bedrock erosion, such as high runoff, which enables efficient transport of eroded material, or the presence of resistant bedrock that inhibits erosion.

In the case of transport-limited incision, sediment flux is close to transport capacity and $\tau_T \gg \tau_D$, so the river struggles to transport away eroded sediment. Sediment covers most of the bed in this scenario, and the erosion rate approaches a limit equal to the sediment transport capacity divided by the drainage area. As a result, K_{eff} depends weakly or not at all on rock strength (and therefore K_r) and instead depends mainly on sediment transport parameters (see Materials and Methods). The erosion rate is kept at the limiting value by the negative sediment cover feedback, such that changes in rock strength are compensated by changes in sediment cover. Thus, in a landscape with transport-limited rivers, two adjacent basins with differing rock types but otherwise similar conditions can have identical effective erodibilities (K_{eff}). Conditions favoring transport-limited behavior are those that inhibit sediment transport relative to erosion, such as low runoff or easily erodible bedrock. Between the end-member cases of purely detachment-limited and transport-limited erosion, both rock strength and sediment transport parameters influence the erosion rate, with their relative influence governed by a system's place on the continuum between the two extremes, as measured by τ_T/τ_D.

Given that runoff strongly influences where a river falls on the spectrum between detachment-limited and transport-limited conditions, we hypothesize that climate controls how strongly rock type influences topography, provided that sediment transport capacity is insensitive to the underlying lithology. In a humid climate, harder, more resistant rock should yield steeper channels and higher topographic relief than softer, more erodible rock, but this difference in steepness and relief should diminish with increasing aridity due to the increasing importance of the sediment cover feedback.

Our theoretical model does not explicitly account for time-variable discharge or erosion thresholds. Most sediment transport and erosion occur during high flows, and it is the degree of

bedrock exposure during these events that is likely the primary control on erosion and sediment transport feedbacks. Thus, the runoff coefficient *r* in our model is meant to represent the runoff rate corresponding to channel-forming flows. Although arid regions tend to exhibit greater flow variability and intermittency than humid regions (10), it is likely that time-integrated runoff during channel-forming flows generally scales with average precipitation, and thus average precipitation is likely to be a useful proxy for sediment transport capacity (21).

1.3. Numerical simulations

We test the prediction that climate modulates lithology's influence on topography by performing numerical simulations of landscapes with variable lithology under a range of climates (see Materials and Methods for details of numerical implementation and all parameters). The model domain consists of an uplifting block to the right of a stable basin, with a fixed base-level

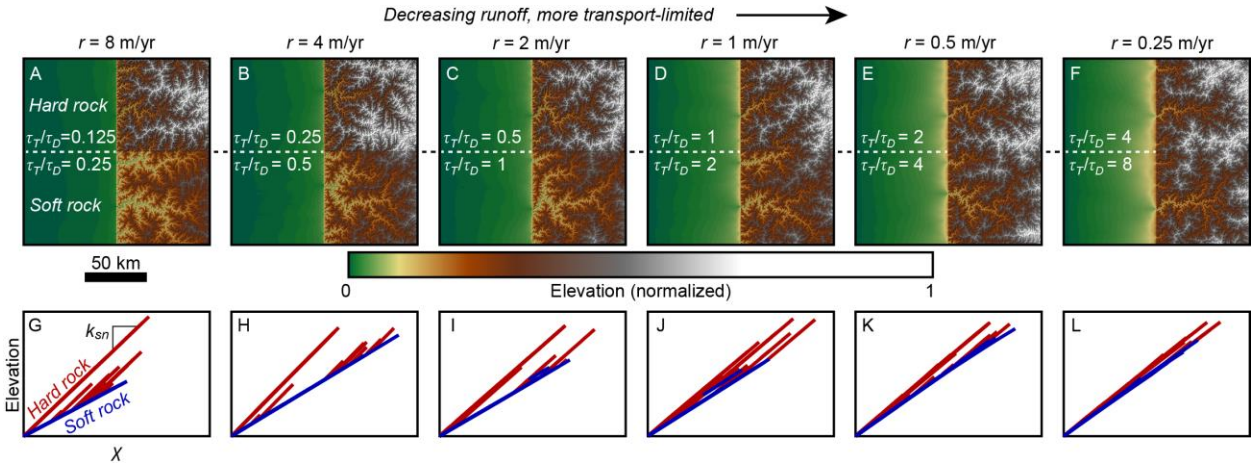

Figure 1.3: Numerical simulation results. A-F: Each panel shows a different model simulation after 70 Myr. All parameters are the same for each except for the runoff coefficient *r*. Plots show relief-shaded color-scaled topography. The elevation color scale is normalized to the maximum elevation in each panel; the total relief scales inversely with runoff due to increasing K_{eff} with increasing runoff. G-L: χ-elevation plots of the river networks corresponding to the topography above, with red lines denoting hard rock (upper half of domain) and blue lines denoting soft rock (lower half of domain). Red lines branching off of blue lines represent tributaries crossing the rock-type boundary. The slope of the lines is the steepness index.

boundary at the left edge. To simulate lithologic heterogeneity, we made the lower half of the model domain twice as erodible (K_r twice as large) as the upper half. The effect of sediment cover on bedrock channel incision is described by implementing the SPACE model (18). We performed six simulations using the same initial condition and model parameters except for the runoff coefficient *r*, which we varied from 0.25 to 8 m/yr to simulate the effect of different climatic conditions. The resulting simulations span the range of detachment-limited to transport-limited behavior, with the sediment cover fraction C_a ranging from 0.1 in the highest-runoff simulation to 0.9 in the lowest-runoff simulation.

After 70 Myr the model topography was essentially at steady state with constant overall relief, although a static steady state was never achieved due to autocyclic behavior of the sediment transport processes (22). The variable effect of lithology on landscape morphology is readily apparent (Figure 1.3). In simulations with high runoff and $\tau_T/\tau_D < 1$ (e.g. Figure 1.3A), the lithologic boundary at the center of the domain marks a clear topographic break between steeper and higher-relief topography in harder rock and gentler topography in softer rock. This is also apparent in χ-transformed river profiles (Figure 1.3G; Materials and Methods), which show that rivers in hard rock have substantially lower effective erodibility than those in soft rock. As runoff decreases, this topographic boundary fades, as does the steepness contrast in the river profiles. In simulations with the lowest runoff and $\tau_T/\tau_D > 1$ (Figure 1.3F, 3L), the boundary is nearly imperceptible in the topography or river profiles. Although all six simulations share the same twofold difference in the bedrock erosion coefficient K_r between harder and softer bedrock, the increased sediment cover that accompanies more transport-limited conditions means that the effective erodibility K_{eff} only differs by 11% at the lowest runoff value (Fig. 3F, 3L); this difference goes up to 80% for the highest runoff value (Fig. 3A, 3G). This numerical experiment

illustrates how climate-dependent sediment transport capacity can, in principle, control the extent to which rock strength influences topography. Our theoretical analysis (Materials and Methods) demonstrates that this effect is a general feature of a negative feedback between erosion and sediment flux, and is not unique to the SPACE model we use here.

1.4. Topographic analysis

We further test this hypothesis against real-world topography by comparing the Oregon Coast Range and the Nevada Basin and Range, two regions of the contiguous United States that represent end-member climatic settings. The spatially averaged mean annual precipitation (MAP) is 2.1 m in the Oregon Coast Range and 0.3 m in the Nevada Basin and Range. Both regions have experienced recent tectonic activity: the Oregon Coast Range is uplifting due to tectonic convergence along the western North American margin, and the Basin and Range is an extensional tectonic province in which individual ranges have been uplifted relative to the adjacent basins.

The small number of measured erosion rates in both regions precludes calculating and comparing effective erodibility K_{eff} for large numbers of basins. We therefore focus on the channel steepness index, $k_{sn} = SA^{\theta}$, as a proxy for effective erodibility, as illustrated in Fig. 3G-L. The steepness index is a measure of channel slope normalized for drainage area that generally scales with unit stream power (4, 23). The exponent θ, termed the concavity, accounts for the widely observed inverse scaling between slope and drainage area, and is typically close to 0.5. If we take $\theta = m/n$ from our generalized erosion law (Eq. 2), we can express the law in terms of the steepness index:

$$E = K_{\text{eff}}(k_{sn})^{n} . \quad (3)$$

Assuming uniform uplift and erosion rates, differences in K_{eff} among drainage basins should manifest as an inverse relationship with the steepness index – lower K_{eff} should cause steeper basins (red lines in Fig. 3G-L). Under these conditions, our climate hypothesis predicts that rivers in wetter climates should exhibit larger differences in steepness between rock types with different erodibility, whereas rivers in drier climates should have more uniform steepness across rock types.

To test this prediction, we measured the steepness index of hundreds to thousands of basins between 5 and 30 km^2 in area in each region (see Materials and Methods). This approach averages over regional and local variability in erosion rate. In Oregon, we divide basins into categories of igneous (primarily Eocene basalt of the Siletz River and Tillamook Volcanics) and siliciclastic sedimentary (primarily Eocene marine sandstone and siltstone of the Tyee formation) (Figure 1.4B). In Nevada, there are large numbers of basins in both volcanic (primarily Tertiary felsic tuff and rhyolite) and plutonic (primarily Mesozoic and Tertiary granite) igneous lithologies; we separate the two igneous categories. Nevada additionally features siliciclastic sedimentary rocks (Figure 1.4E) as well as carbonate sedimentary rocks not present in Oregon. We hypothesize that siliciclastic sedimentary rocks are more erodible than granitic or basaltic rocks due to differences in their physical properties and their lower tensile strength (24). The volcanic rocks present in Nevada are largely poorly lithified felsic tuffs, so we do not expect them to be as strong as granitic or basaltic rocks. Given our general hypothesis that different rock types should have a stronger effect on topography in wetter climates and a weaker effect in drier climates, we predict a substantial difference in the steepness of river basins between basaltic and siliciclastic sedimentary rocks in the Oregon Coast Range, but a smaller difference between granitic and siliciclastic sedimentary rocks in the Nevada Basin and Range.

Comparing the distributions of channel steepness among lithologies and between regions, we find that in the Oregon Coast Range, basins in igneous rocks (primarily basalt) are on average 81±15% steeper than those in siliciclastic rocks (ratio of geometric means, 95% confidence interval, see Materials and Methods) (p<0.0001), and the steepness distributions are clearly distinct (Figures 1.4A, 1.S1). In the Nevada Basin and Range, we find less of a difference among

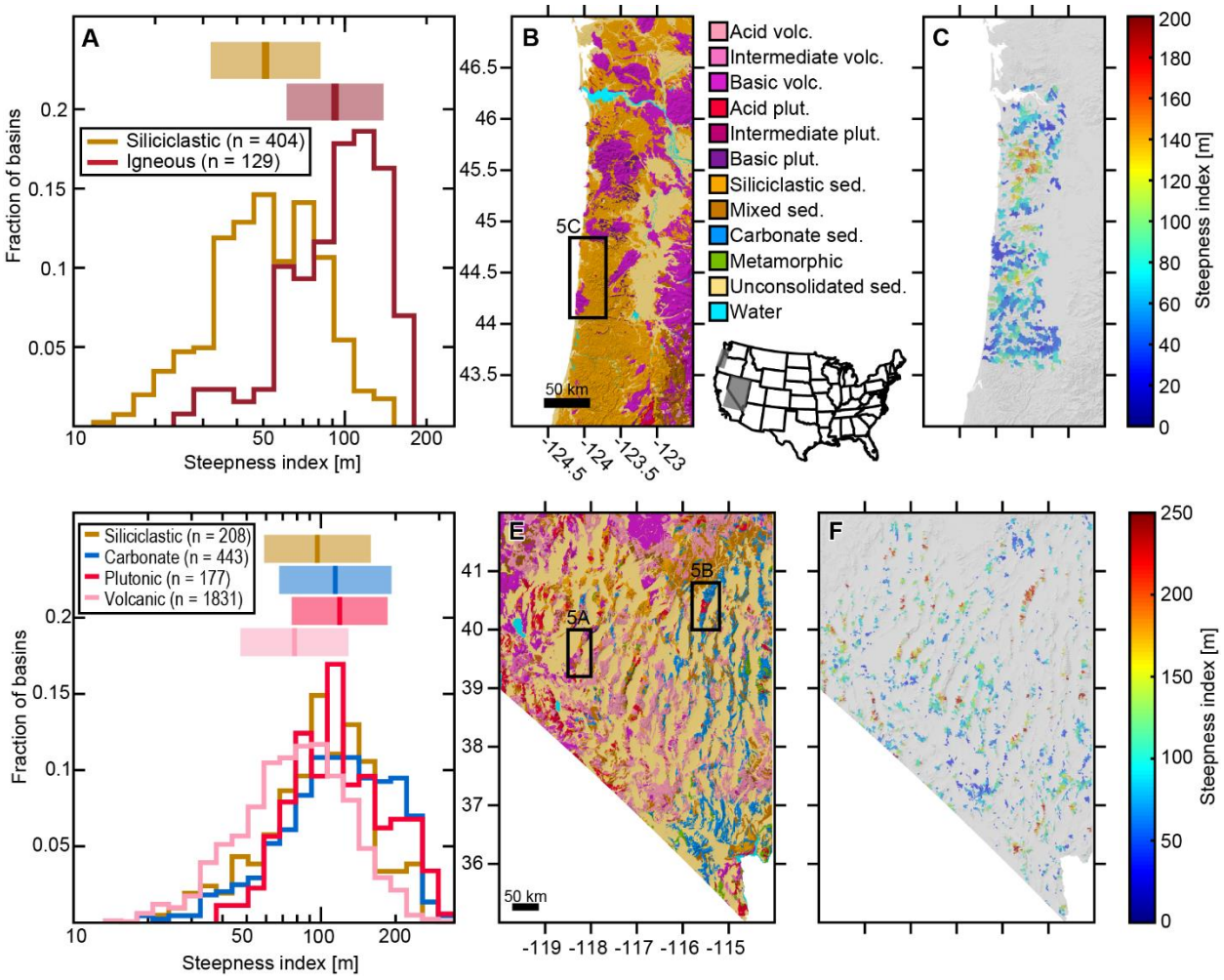

Figure 1.4: River basin steepness and lithology in the Oregon Coast Range (A, B, C) and Nevada Basin and Range (D, E, F). A, D: Binned histograms of basin steepness, separated by lithologic category as shown in the legend. Shaded bars show geometric mean ± 1 standard deviation. B, E: Lithologic maps of each region, from the Lithologic Map of the World (25) (see legend for color scheme). Volc. = volcanic, plut. = plutonic, sed. = sedimentary. Black boxes outline areas shown in Figure 1.5. C, F: Maps showing the basins represented in histograms, colored by steepness index.

lithologies, with smaller differences in means and largely overlapping distributions (Figures 1.4D, 1.S1). Basins in volcanic rocks (largely poorly lithified felsic tuffs) are the least steep and those in plutonic rocks (largely granitic plutons) the steepest on average. Basins in siliciclastic rocks, which may in places be partially metamorphosed, are on average 24±9% steeper than those in volcanic rocks (p<0.0001), but basins in plutonic rocks are 24±12% steeper than siliciclastic (p<0.0001) and 53±11% steeper than volcanic (p<0.0001). We find no statistically significant difference between basins in plutonic and carbonate rocks (p=0.33). The contrasting results from these two regions are consistent with our theoretical prediction that channels in wetter regions like the Oregon Coast Range should be more detachment-limited, and therefore more sensitive to differences in rock type, whereas channels in drier regions should be more transport-limited, and therefore less sensitive to differences in rock type.

To ensure that these results are not solely attributable to other factors, such as geographic gradients in tectonic uplift or climate, we augment this regional analysis with three local case studies of adjacent basins with a common base level but contrasting lithologies (Figure 1.5). Basins in close proximity likely have similar tectonic uplift rates and climate, so differences in channel steepness can more confidently be attributed to differences in rock type. The results of the local comparisons corroborate our regional analyses. In the Stillwater Range in Nevada, which features Tertiary volcanic and granitic rocks juxtaposed against Triassic siliciclastic sedimentary rocks, we find overlapping distributions of basin steepness among the three lithologies, with small and largely insignificant differences in the means (Figure 1.5A). Siliciclastic basins are 11±17% steeper than granitic basins (p=0.22) and 32±30% steeper than volcanic basins (p=0.037); granitic basins are 20±27% steeper than volcanic basins (p=0.15). These differences, although small, likely reflect the mechanical differences among rock units: the

volcanic units are composed of weak tuff, while the siliciclastic units are partially metamorphosed (26). In the Ruby Mountains in Nevada, which features a pegmatitic granite pluton within a Paleozoic carbonate shelf sequence (27), we find that carbonate basins are on average 43±33% steeper (p<0.01) (Figure 1.5B), a slightly larger but still modest contrast. In contrast, in the Oregon Coast Range in the Siuslaw National Forest, which features Eocene basalt and Eocene sandstone and siltstone, we find that igneous basins are on average 243±81% steeper

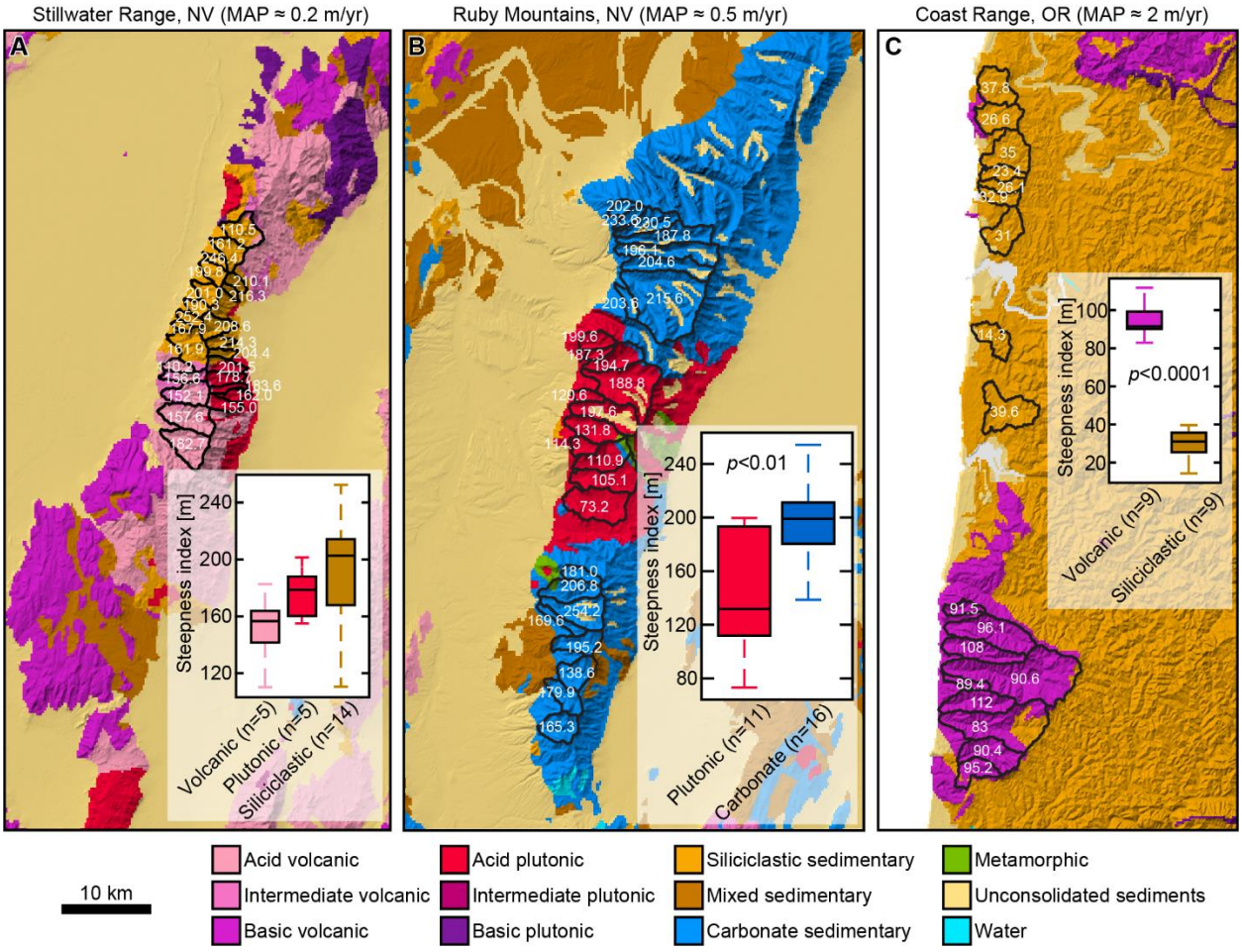

Figure 1.5: Comparisons of channel steepness among drainage basins in adjacent contrasting lithologies. Maps show lithologic categories (see legend) over shaded relief. Locations are indicated in Figure 1.4B, E. Basins analyzed for steepness are outlined in black, with steepness index given in white text. Insets show the steepness distributions of the measured basins: black lines show the median, colored boxes give 25th -75th percentiles, and colored dashed lines show extremes. The p-values given correspond to a two-sample t-test of the means. A: Stillwater Mountains, Nevada. B: Ruby Mountains, Nevada. C: Siuslaw National Forest, Oregon Coast Range.

than sedimentary basins (p<0.0001) (Figure 1.5C). This difference is substantially larger than we observed in our regional analysis of the Oregon Coast Range, suggesting that spatially variable factors other than lithology may decrease the apparent average difference across the region. These local case studies highlight the same trend as our regional analyses: lithology exerts a stronger influence on topography in a humid region than in an arid region.

The interpretation of differences in channel steepness as reflective of differences in effective erodibility hinges on the assumption of a uniform erosion rate. This is a reasonable assumption for the Oregon Coast Range (28, 29) and the Nevada Basin and Range, but there are not enough erosion rate measurements in either region to allow a definitive test. We therefore present an additional analysis of the Appalachian Mountains (Figure 1.6), where a number of studies have yielded a large dataset of cosmogenic nuclide-derived basin-averaged erosion rates (30–36). To add to this dataset, we report 21 new cosmogenic erosion rates from the Upper Tennessee River and Chattooga River basins (Materials and Methods, Supplementary Table 1.1). These erosion rates make it possible to directly calculate K_{eff} from the simplified erosion law

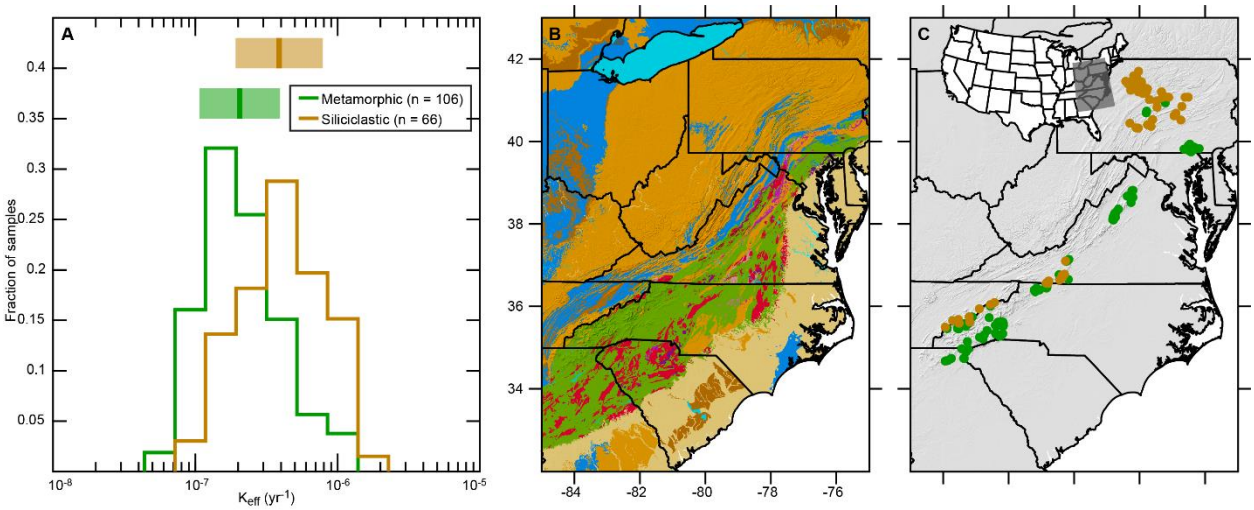

Figure 1.6: Calculated values of effective erodibility K_{eff} in the Appalachian Mountains (see Materials and Methods). A: Histograms of K_{eff} for basins in metamorphic and sedimentary rocks. Note the logarithmic axis. B: Geologic map of study area (see Figure 1.4 for color legend). C: Locations of analyzed drainage basins, colored by lithology as in A.

(Equation 3) by dividing each erosion rate by the steepness index of the basin it averages over, taking the slope exponent to be $n = 1$. Sorting these calculated values of K_{eff} by lithologic category (Figure 1.6B, C), reveals clearly distinct distributions of K_{eff} (Figure 1.6A); the effective erodibility of siliciclastic sedimentary rocks is 94±40% higher on average than metamorphic rocks (p<0.0001), which is consistent with expectations based on mechanical strength (37). This calculation depends on the choice of the slope exponent *n*; the difference in K_{eff} increases with higher values of *n*, indicating that more of the erodibility contrast between the two lithologic categories is accommodated by differences in steepness than by erosion rate. However, the difference is statistically significant for a wide range of positive values of *n* both less than and greater than one. Measurements from carbonate rocks are largely absent due to the need for quartz for ^{10}Be measurements, but topography in carbonate rocks is generally less steep than siliciclastic, indicating even higher erodibility (37). Although there is no comparable erosion rate dataset in an arid region to represent the transport-limited regime, this analysis confirms that the effective erodibility shows a clear dependence on lithology in a humid region, without assuming uniform erosion rates.

1.5. Discussion

1.5.1. Climate modulates effective erodibility

These topographic analyses are consistent with the theoretical and numerical predictions that climate, specifically runoff, modulates the influence of lithology on bedrock channel incision through negative feedbacks involving sediment transport. We see a strong dependence of topography and erodibility on lithology in two humid regions (the Oregon Coast Range and Appalachian Mountains) and a weak dependence in an arid region (the Nevada Basin and

Range). We interpret this difference as the result of a stronger negative feedback on bedrock erosion in arid regions through increased sediment cover. Simply put, stronger rocks do not always generate steeper rivers and higher topographic relief than weaker rocks, especially in arid regions.

Transport-limited river channels mute the effect of lithologic differences as long as sediment transport does not itself depend strongly on lithology. However, a channel's transport capacity may depend on lithology to some extent, due to lithologic effects on grain size or shape, particle density, or partitioning between bed load, suspended load, and dissolved load. Grain size has a particularly strong influence on sediment flux (38), although this effect can be counteracted by corresponding changes in channel width (39), and we do not expect that the differences will be large among basins of similar discharge and drainage area, most of which will feature gravel-bedded channels at the scales we examine.

1.5.2. Lithologic categories and boundaries

The broad lithologic categories used here are a crude proxy for the mechanical properties relevant to bedrock erosion, a necessary approximation due to the scarcity of direct rock strength measurements and the difficulty of relating instantaneous measurements to long-term erodibility. This is evidenced by the Valley and Ridge province, where both "hard" and "soft" units are sedimentary (siliciclastic and carbonate, respectively), but clearly have physical differences meaningful to erosional processes (Figure 1.1). Such variability likely also explains some of the observed variations in steepness and effective erodibility within lithologic categories in our analyses. Nonetheless, these categories probably do correlate with meaningful differences in rock properties (9, 19), and analyzing many basins across regions likely averages out much of the local variability within lithologic categories.

Our analysis focuses on drainage basins in uniform lithology, such that topography can reach a near-steady state for uniform erosion rate and erodibility. Other researchers have shown the potentially complex transient response of rivers eroding through layered rocks due to the lateral migration of lithologic contacts across the lowering land surface (40, 41). Our results imply that this transient response should also be a function of climate and the relative importance of detachment-limited and transport-limited channel incision. Under transport-limited conditions, where channel slope is set primarily by upstream-integrated erosion and sediment flux, rather than local erosion rate, we expect that the effect of layered rocks and lithologic boundaries on topography is inhibited (15).

1.5.3. Orographic feedbacks

In all three regions analyzed in this study, the steepness index and the modern precipitation rate for each basin are positively correlated. This relationship, which is contrary to the usual expectation of increased erodibility from increased runoff (8), occurs because steeper basins generally contain higher elevations where precipitation is orographically enhanced. This orographic feedback partially offsets the effect of lithology on channel steepness and erodibility, meaning that the true effect of lithologic variation, especially in a humid region, may be larger than we observe with our analysis.

We investigate this effect with an additional calculation that accounts for precipitation differences. Since the steepness index is a rough proxy for unit stream power, in which drainage area is a proxy for discharge, we attempt to account for variations in runoff by multiplying the drainage area by the basin-averaged MAP in the steepness index calculation, yielding a precipitation-adjusted steepness index, and repeating our regional analyses (Figures 1.S2-1.S4) (see Materials and Methods). The results are similar to those obtained without correcting for

precipitation rates (Figures 1.3 and 1.5), but the differences between rock types are amplified due to the positive correlation between precipitation and steepness. For example, in the Oregon Coast Range we find that igneous basins are 111±22% steeper than sedimentary basins using the precipitation-adjusted steepness (Figure 1.S2), compared with 81±15% for the unadjusted steepness index (Figure 1.4A). In Nevada, we find that siliciclastic basins are 33±11% steeper than volcanic basins, compared with 23±8% for the unadjusted steepness. This method of accounting for differences in runoff among basins is imperfect because modern precipitation rates may not be representative of the formative conditions shaping these landscapes over time, and because runoff may not scale linearly with precipitation due to differences in watershed hydrology. Nevertheless, this analysis suggests that orographic effects may partially counteract differences in steepness that result from lithologic contrasts, and that the immediate effect of lithologic differences may be larger than what is apparent from a large-scale topographic analysis. Moreover, this amplification of differences is much larger for the Oregon Coast Range than in Nevada, suggesting that the contrast between sediment cover effects on channel incision between humid and arid landscapes may be even starker than our initial analysis suggested.

1.5.4. Global implications

The regions we analyze span much of the globally observed distribution of precipitation, with a range encompassing three-quarters of Earth's land surface (42). We therefore expect that rivers worldwide have widely varying responses to lithologic heterogeneity, governed by their place on the spectrum from detachment- to transport-limited. 43% of Earth's land surface (excluding Antarctica) is classified as "humid" by the aridity index (43); we expect that many erosional rivers in these regions are dominantly detachment-limited due to efficient sediment transport. These river basins should show a clear dependence of erodibility and topography on

lithology, similarly to the Oregon Coast Range or the Appalachian Mountains. Conversely, 39% of Earth's land surface is classified as either "semi-arid" or "arid;" we expect erosional rivers in these regions to be more transport-limited, and thus less sensitive to differences in bedrock properties.

The climate-modulated sensitivity of rivers to rock strength has likely influenced the evolution of continental topography and the degree to which topography reflects lithology in different regions. This complicated and varied relationship among climate, lithology, and erosion may explain the difficulty of identifying trends in global datasets. The sediment cover feedback likely acts in combination with other climatic influences on the relationship between lithology and erodibility, such as chemical weathering or dissolution (44, 45). These effects may be particularly important in post-orogenic landscapes (e.g., Figure 1.1) where erosion rates can approach spatial uniformity over long timescales and topography is not governed by active tectonic uplift.

1.6. Conclusions

We show that the widely proposed sediment cover feedback on bedrock channel incision, in which sediment produced by erosion armors the riverbed and slows channel incision, implies that the influence of rock strength on erosion rates and topography is weaker in landscapes with more transport-limited rivers. If rivers are more transport-limited in more arid landscapes with less runoff, this in turn implies that climate modulates the influence of rock type on erosion and landscape evolution. We corroborate this prediction with numerical modeling and test it with comparative topographic analysis of end-member climatic settings. The results show that river channel steepness depends strongly on rock erodibility in humid regions but only weakly in an

arid region, consistent with a transition from detachment-limited to transport-limited conditions with declining runoff. This non-linear interaction between climate and rock type, two of the major factors that govern landscape evolution, implies that rivers globally may exhibit a wide range of sensitivity to bedrock geology, obscuring trends in global data.

1.7. Materials and Methods

1.7.1. Theoretical model

We use three proposed models (2, 17, 18) for the area fraction of sediment cover on a riverbed, expressed in terms of other physical quantities relating to sediment transport.

$$C_a = \frac{Q_s}{Q_{sc}} \tag{4a}$$

$$C_a = 1 - \exp\left(-\phi \frac{Q_s}{Q_{sc}}\right) \tag{4b}$$

$$C_a = 1 - \exp\left(-\frac{h_s}{h^*}\right) \tag{4c}$$

In these expressions, Q_s is the volumetric sediment flux [L^3/T], Q_{sc} is the maximum volumetric sediment transport capacity [L^3/T], h_s is the thickness of sediment on the bed [L], and h^* is a characteristic bed roughness scale [L] (see below). The coefficient ϕ in Eq. 4b describes the nature of sediment deposition and the resulting dependence of sediment cover on sediment flux (17). In the following section, we substitute each of these three expressions into the modified stream power erosion law (Eq. 1) and analyze the resulting behavior at uniform, steady erosion. We derive corresponding expressions for the effective erodibility (Eq. 2) and show detachment- and transport-limited limits of this quantity for each model. We derive a dimensionless number for each that characterizes the relative strength of detachment and transport processes for a river channel.

1.7.2. Scenario I: Linear decline model

Here we follow ref. (2) and model the sediment cover as a linear function of the volumetric sediment flux Q_s relative to the transport capacity of the flow Q_{sc}, such that the bed is entirely exposed at zero transport and entirely covered when transport exactly matches capacity (Eq. 4a). We model the transport capacity of the river channel as another power-law function of discharge and slope (7, 15, 46, 47), with exponents α and β typically larger than m and n (15, 47–49):

$$Q_{sc} = K_c Q_w^{\alpha} S^{\beta} . \tag{5}$$

We assume steady-state erosion, such that the sediment flux is equal to the product of the erosion rate times drainage area:

$$Q_s = EA. \tag{6}$$

We assume that water discharge scales linearly with drainage area, with the runoff coefficient r [L/T] describing the balance of precipitation, evaporation, and infiltration:

$$Q_w = rA. \tag{7}$$

Substituting equations 5-7 into the erosion law (Eq. 1), and solving for the erosion rate E gives

$$E = \frac{K_r (rA)^m S^n}{1 + \frac{K_r}{K_c} A (rA)^{m-\alpha} S^{n-\beta}}. \tag{8}$$

The dimensionless number $\frac{K_r}{K_c} A (rA)^{m-\alpha} S^{n-\beta}$ in the denominator describes the relative importance of detachment and transport processes, and can be expressed as the ratio τ_T / τ_D, where τ_T is a characteristic timescale of transport processes and τ_D is a characteristic timescale of detachment processes, each for a given amount of erosion δz:

$$\tau_T = \frac{\delta z A}{Q_{sc}} = \frac{\delta z A}{K_c (rA)^{\alpha} S^{\beta}} , \tag{9}$$

$$\tau_D = \frac{\delta z}{E} = \frac{\delta z}{K_r (rA)^m S^n}. \quad (10)$$

In these expressions, τ_T is the time necessary to transport the sediment created by eroding a vertical distance of δz over the upstream drainage area A at transport capacity given by Eq. 5. τ_D is the time necessary to erode that vertical distance in the absence of any sediment cover limitations (Eq. 1).

In the low-sediment flux limit, where $Q_s \ll Q_{sc}$, this dimensionless number is small and the denominator is close to one, giving the limit

$$K_{\text{eff}} \approx K_r r^m, \quad (11)$$

for the effective erodibility in the generalized erosion law (Eq. 2). This corresponds to $\tau_D \gg \tau_T$, indicating that detachment is the rate-limiting process. In the high-sediment flux limit, where $Q_s \approx Q_{sc}$, the dimensionless number is large and the denominator is much larger than one, giving the limit

$$K_{\text{eff}} \approx K_c r^{\alpha-m} A^{\alpha-m-1} S^{\beta-n}. \quad (12)$$

This limit corresponds to transport-limited conditions, where $\tau_T \gg \tau_D$. In the fully transport-limited case, the erosion rate is simply the transport capacity divided by the drainage area.

1.7.3. Scenario II: Exponential decline model

Here we follow the exponential decline model of ref. (17) for sediment cover as a function of the sediment flux relative to the transport capacity (Eq. 4b). As in Scenario I, we assume steady-state erosion, a power-law sediment transport capacity law, and linear discharge-drainage area scaling (Eqs. 5-7). Combining these equations gives

$$E = K_r (rA)^m S^n \exp\left(-\phi \frac{EA}{K_c (rA)^\alpha S^\beta}\right), \quad (13)$$

where ϕ characterizes processes of sediment deposition and bed cover (17). This equation does not have a simple solution for the erosion rate E. We instead evaluate two limits where $\frac{Q_s}{Q_{sc}} \approx 0$ and $\frac{Q_s}{Q_{sc}} \approx 1$, and linearly expand around these two points. In the first limit, we find

$$E \approx K_r (rA)^m S^n \left(1 - \phi \frac{EA}{K_c (rA)^\alpha S^\beta}\right). \tag{14}$$

Since $\frac{Q_s}{Q_c} \approx 0$, the last term is close to one, giving $E \approx K_r (rA)^m S^n$ and $K_{\text{eff}} \approx K_r r^m$. In the second limit, we find

$$E \approx K_r (rA)^m S^n \exp(-\phi) \left(1 + \phi \left(1 - \frac{EA}{K_c (rA)^\alpha S^\beta}\right)\right). \tag{15}$$

Solving for the erosion rate E gives

$$E \approx \frac{K_r (rA)^m S^n \exp(-\phi)\,(1+\phi)}{\left(1 + \phi \exp(-\phi)\, A \frac{K_r}{K_c} (rA)^{m-\alpha} S^{n-\beta}\right)}. \tag{16}$$

Since $Q_s \approx Q_{sc}$, the denominator is much larger than one. We can therefore simplify this expression to

$$E \approx \frac{(1+\phi)}{\phi} \frac{K_c (rA)^\alpha S^\beta}{A}, \tag{17}$$

which yields the following expression for effective erodibility:

$$K_{\text{eff}} \approx \frac{(1+\phi)}{\phi} K_c r^{\alpha-m} A^{\alpha-m-1} S^{\beta-n}. \tag{18}$$

Equation 15 states that the erosion rate is equal to the sediment transport capacity divided by the drainage area, multiplied by the factor $(1+\phi)/\phi$ to account for the fact that the bed can be partially exposed even when $Q_s = Q_{sc}$. This factor is always larger than one, and approaches one for large ϕ. The dimensionless number $\phi \exp(-\phi)\, A \frac{K_r}{K_c} (rA)^{m-\alpha} S^{n-\beta}$ is analogous to that

described for Scenario I with an additional prefactor to account for the exponential decline model.

1.7.4. Scenario III: SPACE model

Here, we use a version of the SPACE model (18), a disequilibrium erosion and transport model similar to that of ref. (50), but with a two-phase substrate of distinct bedrock and sediment components. The erosion rates of these two phases are both described as functions of stream power, partitioned by the sediment cover fraction, which is modeled as an exponential function of the bed sediment thickness h_s [L] relative to a characteristic bed roughness scale h^* (Eq. 4c):

$$E_r = K_r Q_w^m S^n (1 - C_a), \tag{19}$$

$$E_s = K_s Q_w^m S^n C_a. \tag{20}$$

E_r and E_s [L/T] are the erosion rates of bedrock and sediment, respectively, with K_r and K_s [L^{1-3m}/T^{1-m}] the rate coefficients for each process. The different coefficients reflect the different erodibilities of the two materials, generally with $K_s > K_r$. The material eroded from the bed (both bedrock and sediment) is added to the sediment flux of the river. The deposition of sediment onto the bed is modeled as a linear function of the volumetric sediment concentration,

$$D_s = D^* \frac{Q_s}{Q_w}, \tag{21}$$

where D^* is a characteristic deposition rate [L/T]. These expressions are combined to give the time evolution equations for the bedrock height and sediment thickness,

$$\frac{\partial z_r}{\partial t} = U - E_r, \tag{22a}$$

$$\frac{\partial h_s}{\partial t} = D_s - E_s, \tag{22b}$$

where z_r [L] is the height of the bedrock surface above a vertical datum and U is the tectonic uplift rate [L/T]. As in the first two scenarios, we parameterize the water discharge as a linear

function of the upstream drainage area (Eq. 7). Given a uniform erosion rate E, the sediment thickness will reach an equilibrium value h_s^{eq} satisfying the following conditions:

$$Q_s = EA\,, \tag{23a}$$

$$E_r = E\,, \tag{23b}$$

$$E_s = D_s\,. \tag{23c}$$

This equilibrium value is:

$$h_s^{eq} = h^* \ln\left(1 + \frac{K_r}{K_s}\frac{D^*}{r}\right), \tag{24}$$

which gives the effective erodibility

$$K_{\text{eff}} = \frac{K_r r^m}{\left(1 + \frac{K_r}{K_s}\frac{D^*}{r}\right)}. \tag{25}$$

If $h_s^{eq} \ll h^*$, the denominator is close to one, giving $K_{\text{eff}} \approx K_r r^m$, corresponding to detachment-limited conditions. If $h_s^{eq} \gg h^*$, the denominator is much larger than one, giving $K_{\text{eff}} \approx K_s r^{1+m}/D^*$, corresponding to transport-limited conditions. The dimensionless number $\frac{K_r}{K_s}\frac{D^*}{r}$ governs a system's place between these two limits, with small values indicating detachment-limited conditions and large values indicating transport-limited conditions. Similarly to Scenarios I and II, this dimensionless number can be expressed as a ratio of transport and detachment timescales. The detachment timescale takes the same form as above (Eq. 10). Since the equilibrium transport capacity (i.e. $E_s = D_s$) for $h_s \gg h^*$ and $C_a \approx 1$ is given by $Q_{sc} = K_s(rA)^{m+1}S^n/D^*$, the transport timescale for this model can be expressed as

$$\tau_T = \frac{D^*\delta z A}{K_s(rA)^{m+1}S^n}. \tag{26}$$

1.7.5. Numerical methods

We computed numerical solutions of the governing equations for the SPACE model (Eqs. 19-22b) following the semi-analytical forward-time algorithm of (18). We discretized our model domain as a 500×500 rectangular grid. We used steepest-descent flow routing applied to the solid surface (bedrock plus sediment), using the Priority-Flood algorithm of (51) implemented in the RichDEM package (52). The left boundary was set to a constant base level, the upper and lower boundaries were periodic, and the right boundary was impermeable to water and sediment. The right half of the model domain had an uplift rate of 10^{-4} m/yr; the left half had no uplift. The model domain also featured two different lithologies: the upper half had a bedrock erosion coefficient (K_r) of 4×10^{-6} $m^{-0.5}$ $yr^{-0.5}$; the lower half had a coefficient of 8×10^{-6} $m^{-0.5}$ $yr^{-0.5}$, twice as large. All other parameters were spatially uniform. We performed six runs with varying values of the runoff coefficient (r), with all other parameters held constant for all six runs. Values for all parameters are given in Table 1.1. The initial topography we used for each run consisted of a repeated 500×250 pixel grid of uniformly distributed random noise, such that the top and bottom halves of the model domain had the same initial condition.

Table 1.1: Parameters for numerical simulations

Parameter	**Value(s)**
Bedrock erosion coefficient (K_r)	4×10^{-6}, 8×10^{-6} $m^{-0.5}$ $yr^{-0.5}$
Sediment erosion coefficient (K_s)	2×10^{-5} $m^{-0.5}$ $yr^{-0.5}$
Characteristic deposition rate (D^*)	5 m/yr
Discharge exponent (m)	0.5
Slope exponent (n)	1
Runoff rate (r)	0.25-8 m/yr
Characteristic bed roughness scale (h^*)	1 m
Grid spacing (Δx, Δy)	300 m
Timestep duration (Δt)	10 yr
Uplift rate (U)	0, 10^{-4} m/yr

1.7.6. Topographic analysis

We computed channel metrics using MERIT DEM and MERIT Hydro elevation and hydrographic datasets at 3 arc-second (~90 m) resolution (53, 54). For regional analyses, we divided the landscape into drainage basins of minimum 5 km^2 and maximum 30 km^2 upstream drainage area. For each basin, we then computed the channel steepness index k_{sn} by applying a linear regression to the χ-transformed elevation profiles (55) for all points in the basin with a drainage area greater than 10 pixels (including main-stem and tributary profiles). We used a uniform concavity exponent of 0.5 for all analyses to facilitate comparison among basins and regions. For each basin, we also computed the areal fraction corresponding to each lithologic category from the Lithologic Map of the World (25) and the basin-averaged MAP using the PRISM dataset (56). To create the histograms for Oregon and Nevada shown in Figure 1.4, we considered only basins with an areal fraction of the specified lithology greater than 0.8. To ensure locally steady-state topography and linear χ-elevation profiles, we excluded basins with an R^2 value smaller than 0.5 for the k_{sn} regression; this criterion excludes only a small fraction of basins. For each Appalachian cosmogenic erosion rate sample, we computed k_{sn} and the basin lithologic composition as above, considering the basin with its outlet at the sample location. We excluded samples with drainage areas greater than 100 km^2 and applied the same criteria for basin lithologic composition and R^2 value. Sample distributions for steepness and effective erodibility are roughly log-normal, so we compare the ratio of the geometric means with a paired *t*-test of the logarithm of the values. This analysis gives a 95% confidence interval for the difference in the arithmetic means of the logarithms, which we transform into the ratio of the geometric means of the raw values.

We used the basin-averaged MAP to estimate a runoff-corrected steepness, by substituting the product of the MAP and drainage area for the drainage area in the steepness index, yielding the following expression for adjusted steepness: $S(MAP \times A)^{\theta}$. The steepness index is commonly assumed to scale with unit stream power, where the drainage area is a proxy for water discharge. If the runoff ratio (discharge per unit drainage area) scales linearly with MAP, then this runoff-corrected steepness will provide a more accurate proxy for unit stream power. We similarly estimated the runoff-corrected effective erodibility for the Appalachian cosmogenic samples by dividing the erosion rate by the runoff-corrected steepness index. The results of this analysis are presented in Supplementary Figures 1.S2-1.S4.

1.7.7. Cosmogenic erosion rates

We compiled 256 basin-averaged ^{10}Be-derived erosion rates measured in the central and southern Appalachian Mountains from previous studies (30–36). For the studies published prior to 2011 we used the erosion rates as re-calculated by (13). For all other studies we used the erosion rates reported by the original authors. We supplemented this compilation with 21 additional erosion rates measured in the Upper Chattooga and Tennessee River basins. We sampled sediment from active bars, pools, and the beds of channels. We isolated quartz and extracted ^{10}Be at the University of Massachusetts Cosmogenic Nuclide Laboratory. The samples were analyzed using the accelerator mass spectrometer (AMS) at the Purdue Rare Isotope Measurement Laboratory (PRIME Lab) and normalized to the 07KNSTD standard (57). We ran two process blanks and subtracted the average ^{10}Be/^{9}Be ratio of the process blanks from the sample measurements. We propagated the sample and mean blank uncertainty to represent 1σ analytical uncertainty on each of the measurements. We then used the CRONUS v3.0 calculator (58) to derive erosion rates from our measured ratios. We followed the methods of (13) to

calculate an effective latitude, longitude, and elevation for each basin. We assumed that there is no topographic shielding (59) and that the density of the material is 2.65 g cm^{-3}. We used the Lal/Stone cosmogenic isotope production scaling (60, 61) and report the external uncertainty in erosion rate. Sample locations, concentrations, and erosion rates are listed in Table 1.S1.

Acknowledgments

This paper is based upon work supported by the National Aeronautics and Space Administration Earth and Space Science Fellowship under Grant No. 80NSSC18K1324 (SLG), the USAF-MIT AI Accelerator Project (JTP and SLG), the mTerra Catalyst Fund (MFS and JTP), the National Science Foundation Graduate Research Fellowship under Grant No. 1122374 (MFS), and the National Science Foundation EarthScope AGeS Program under Grant Nos. EAR-1358514, 1358554, 1358401, 1358443, and 1101100 (MFS and JTP). We thank Richard Barnes for assistance implementing his flow routing code, Isaac Larsen for his assistance with ^{10}Be sample preparation, and Sean Gallen for his assistance with sample collection.

References

1. Whipple KX (2004) Bedrock Rivers and the Geomorphology of Active Orogens. *Annu Rev Earth Planet Sci* 32(1):151–185.
2. Sklar LS, Dietrich WE (2004) A mechanistic model for river incision into bedrock by saltating bed load. *Water Resour Res* 40:1–21.
3. Finnegan NJ, Roe GH, Montgomery DR, Hallet B (2005) Controls on the channel width of rivers: Implications for modeling fluvial incision of bedrock. *Geology* 331(3):229–232.
4. Snyder NP, Whipple KX, Tucker GE, Merritts DJ (2000) Landscape response to tectonic

forcing: Digital elevation model analysis of stream profiles in the Mendocino triple junction region, northern California. *Geol Soc Am Bull* 112(8):1250–1263.

5. Lague D (2014) The stream power river incision model: Evidence, theory and beyond. *Earth Surf Process Landforms* 39(1):38–61.
6. Howard AD, Kerby G (1983) Channel changes in badlands. *Geol Soc Am Bull* 94:739–752.
7. Howard AD (1994) A detachment limited model of drainage basin evolution. *Water Resour Res* 30(7):2261–2285.
8. Ferrier KL, Huppert KL, Perron JT (2013) Climatic control of bedrock river incision. *Nature* 496:206–209.
9. Stock JD, Montgomery DR (1999) Geologic constraints on bedrock river incision using the stream power law. *J Geophys Res Solid Earth* 104(B3):4983–4993.
10. Perron JT (2017) Climate and the Pace of Erosional Landscape Evolution. *Annu Rev Earth Planet Sci* 45(1):561–591.
11. Hack JT (1960) Interpretation of erosional topography in humid temperate regions. *Am J Sci* 258-A:80–97.
12. Cook KL, Whipple KX, Heimsath AM, Hanks TC (2009) Rapid incision of the Colorado River in Glen Canyon – insights from channel profiles, local incision rates, and modeling of lithologic controls. *Earth Surf Process Landforms* 34:994–1010.
13. Portenga EW, Bierman PR (2011) Understanding Earth's eroding surface with 10 Be. *GSA Today* 21(8):4–10.
14. Harel MA, Mudd SM, Attal M (2016) Global analysis of the stream power law parameters based on worldwide 10Be denudation rates. *Geomorphology* 268:184–196.

15. Whipple KX, Tucker GE (2002) Implications of sediment-flux-dependent river incision models for landscape evolution. *J Geophys Res* 107(B2):1–20.

16. Nittrouer JA, Mohrig D, Allison MA, Peyret AB (2011) The lowermost Mississippi River: a mixed bedrock-alluvial channel. *Sedimentology* 58(7):1914–1934.

17. Turowski JM, Lague D, Hovius N (2007) Cover effect in bedrock abrasion: A new derivation and its implications for the modeling of bedrock channel morphology. *J Geophys Res Earth Surf* 112(4):1–16.

18. Shobe CM, Tucker GE, Barnhart KR (2017) The SPACE 1.0 model: a Landlab component for 2-D calculation of sediment transport, bedrock erosion, and landscape evolution. *Geosci Model Dev* 19:4577–4604.

19. Sklar LS, Dietrich WE (2001) Sediment and rock strength controls on river incision into bedrock. *Geology* 29(12):1087–1090.

20. Lague D (2010) Reduction of long-term bedrock incision efficiency by short-term alluvial cover intermittency. *J Geophys Res Earth Surf* 115(F2):1–23.

21. Deal E, Braun J, Botter G (2018) Understanding the Role of Rainfall and Hydrology in Determining Fluvial Erosion Efficiency. *J Geophys Res Earth Surf* 123:744–778.

22. Yuan XP, Braun J, Guerit L, Rouby D, Cordonnier G (2019) A New Efficient Method to Solve the Stream Power Law Model Taking Into Account Sediment Deposition. *J Geophys Res Earth Surf* 124(6):1346–1365.

23. Hack JT (1973) Stream-profile analysis and the stream-gradient index. *J Res US Geol Surv* 1(4):421–429.

24. Perras MA, Diederichs MS (2014) A Review of the Tensile Strength of Rock : Concepts and Testing. *Geotech Geol Eng* 32:525–546.

25. Hartmann J, Moosdorf N (2012) The new global lithological map database GLiM: A representation of rock properties at the Earth surface. *Geochemistry, Geophys Geosystems* 13(12):1–37.

26. Nelson SW (1975) The Petrology of a Zoned Granitic Stock, Stillwater Range, Churchill County, Nevada. Dissertation (University of Nevada, Reno).

27. Willden R, Kistler RW (1969) *Geologic map of the Jiggs quadrangle, Elko County, Nevada (Geologic Quadrangle Map GQ-859)* (Washington, D.C.).

28. Reneau SL, Dietrich WE (1991) Erosion rates in the southern Oregon Coast Range: Evidence for an equilibrium between hillslope erosion and sediment yield. *Earth Surf Process Landforms* 16(4):307–322.

29. Heimsath AM, Dietrich WE, Nishiizumi K, Finkel RC (2001) Stochastic processes of soil production and transport: Erosion rates, topographic variation and cosmogenic nuclides in the Oregon Coast Range. *Earth Surf Process Landforms J Br Geomorphol Res Gr* 26(5):531–552.

30. Matmon A, et al. (2003) Erosion of an ancient mountain range, the Great Smoky Mountains, North Carolina and Tennessee. *Am J Sci* 303(9):817–855.

31. Duxbury J (2009) Erosion Rates in and Around Shenandoah National Park, VA Determined Using Analysis of Cosmogenic 10Be. Dissertation (University of Vermont). doi:10.2475/01.2015.02.

32. Linari CL, et al. (2017) Rates of erosion and landscape change along the Blue Ridge escarpment, southern Appalachian Mountains, estimated from in situ cosmogenic 10Be. *Earth Surf Process Landforms* 42(6):928–940.

33. Marstellar TL (2012) Investigating sediment source to sink processes in a post-orogenic

landscape. Dissertation (Georgia Institute of Technology).

34. Reuter JM (2005) Erosion rates and patterns inferred from cosmogenic 10Be in the Susquehanna River Basin. Dissertation (University of Vermont).

35. Reusser L, Bierman PR, Rood D (2015) Quantifying human impacts on rates of erosion and sediment transport at a landscape scale. *Geology* 43(2):171–174.

36. Stokes MF, Larsen IJ, Goldberg SL, McCoy SW, Perron JT The erosional signature of divide motion along the Blue Ridge escarpment. *Geol (in prep).*

37. Mills HH (2003) Inferring erosional resistance of bedrock units in the east Tennessee mountains from digital elevation data. *Geomorphology* 55(1–4):263–281.

38. Engelund F, Hansen E (1967) A monograph on sediment transport in alluvial streams. *Monografia*:65.

39. Wickert AD, Schildgen TF (2019) Long-profile evolution of transport-limited gravel-bed rivers. *Earth Surf Dyn* 7(1):17–43.

40. Forte AM, Yanites BJ, Whipple KX (2016) Complexities of landscape evolution during incision through layered stratigraphy with contrasts in rock strength. *Earth Surf Process Landforms* 41(12):1736–1757.

41. Mitchell NA, Yanites BJ (2021) Bedrock River Erosion through Dipping Layered Rocks: Quantifying Erodibility through Kinematic Wave Speed. *Earth Surf Dyn* 9:723–753.

42. Fick SE, Hijmans RJ (2017) WorldClim 2: new 1-km spatial resolution climate surfaces for global land areas. *Int J Climatol* 37(12):4302–4315.

43. Trabucco A, Zomer RJ (2018) Global Aridity Index and Potential Evapo-Transpiration (ET0) Climate Database v2. *CGIAR Consort Spat Inf.*

44. Murphy BP, Johnson JPL, Gasparini NM, Sklar LS (2016) Chemical weathering as a

mechanism for the climatic control of bedrock river incision. *Nature* 532:223–227.

45. Peifer D, Persano C, Hurst MD, Bishop P, Fabel D (2021) Growing topography due to contrasting rock types in a tectonically dead landscape. *Earth Surf Dyn* 9:167–181.

46. Paola C, Heller PL, Angevine CL (1992) The large-scale dynamics of grain-size variation in alluvial basins, 1: Theory. *Basin Res* 4(2):73–90.

47. Begin ZB, Meyer DF, Schumm SA (1981) Development of longitudinal profiles of alluvial channels in response to base-level lowering. *Earth Surf Process Landforms* 6(1):49–68.

48. Howard AD, Dietrich WE, Seidl MA (1994) Modeling fluvial erosion on regional to continental scales. *J Geophys Res* 99(B7):13971–13986.

49. Willgoose G, Bras RL, Rodríguez-Iturbe I (1991) A coupled channel network growth and hillslope evolution model: 1. Theory. *Water Resour Res* 27(7):1671–1684.

50. Davy P, Lague D (2009) Fluvial erosion/transport equation of landscape evolution models revisited. *J Geophys Res Earth Surf* 114(3):1–16.

51. Barnes R, Lehman C, Mulla D (2014) Priority-flood: An optimal depression-filling and watershed-labeling algorithm for digital elevation models. *Comput Geosci* 62:117–127.

52. Barnes R (2016) RichDEM: Terrain Analysis Software.

53. Yamazaki D, et al. (2017) A high-accuracy map of global terrain elevations. *Geophys Res Lett* 44(11):5844–5853.

54. Yamazaki D, et al. (2019) MERIT Hydro: A High-Resolution Global Hydrography Map Based on Latest Topography Dataset. *Water Resour Res* 55(6):5053–5073.

55. Perron JT, Royden LH (2013) An integral approach to bedrock river profile analysis. *Earth Surf Process Landforms* 576(August 2012):570–576.

56. Group PC (2012) PRISM 30-year Normals.

57. Nishiizumi K, et al. (2007) Absolute calibration of 10Be AMS standards. *Nucl Instruments Methods Phys Res B* 258:403–413.

58. Balco G, Stone JO, Lifton NA, Dunai TJ (2008) A complete and easily accessible means of calculating surface exposure ages or erosion rates from 10 Be and 26 Al measurements. *Quat Geochronol* 3:174–195.

59. DiBiase RA (2018) Short communication : Increasing vertical attenuation length of cosmogenic nuclide production on steep slopes negates topographic shielding corrections for catchment erosion rates. *Earth Surf Dyn* 6:923–931.

60. Lal D (1991) Cosmic ray labeling of erosion surfaces: in situ nuclide production rates and erosion models. *Earth Planet Sci Lett* 104:424–439.

61. Stone JO (2000) Air pressure and cosmogenic isotope production. *J Geophys Res* 105(B10):23753–23759.

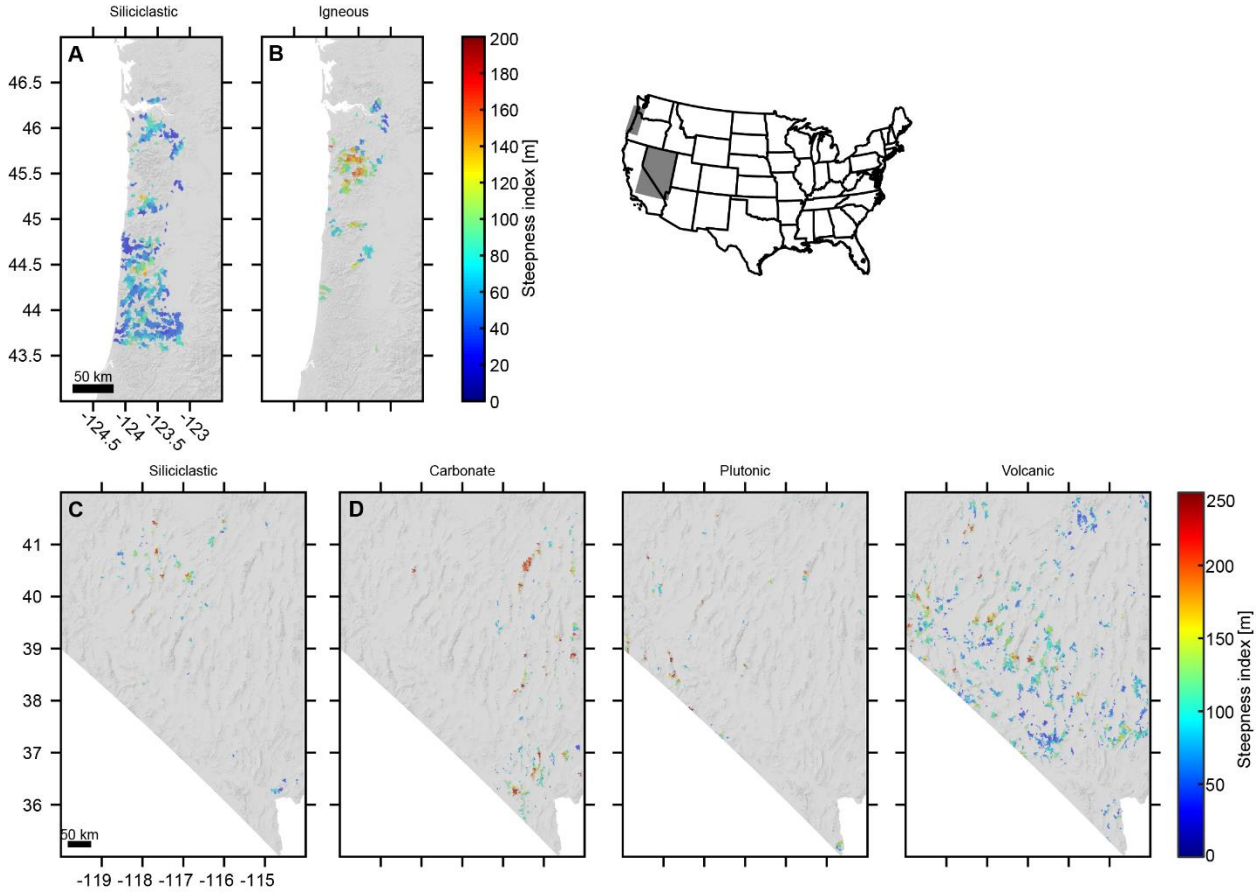

Figure 1.S1: Maps of basins in the Oregon Coast Range (A, B) and the Nevada Basin and Range (C, D, E) separated by lithology and colored by steepness index. Basins shown here are the basins that met our screening criteria and were included in histograms in Figure 1.3 (see Materials and Methods).

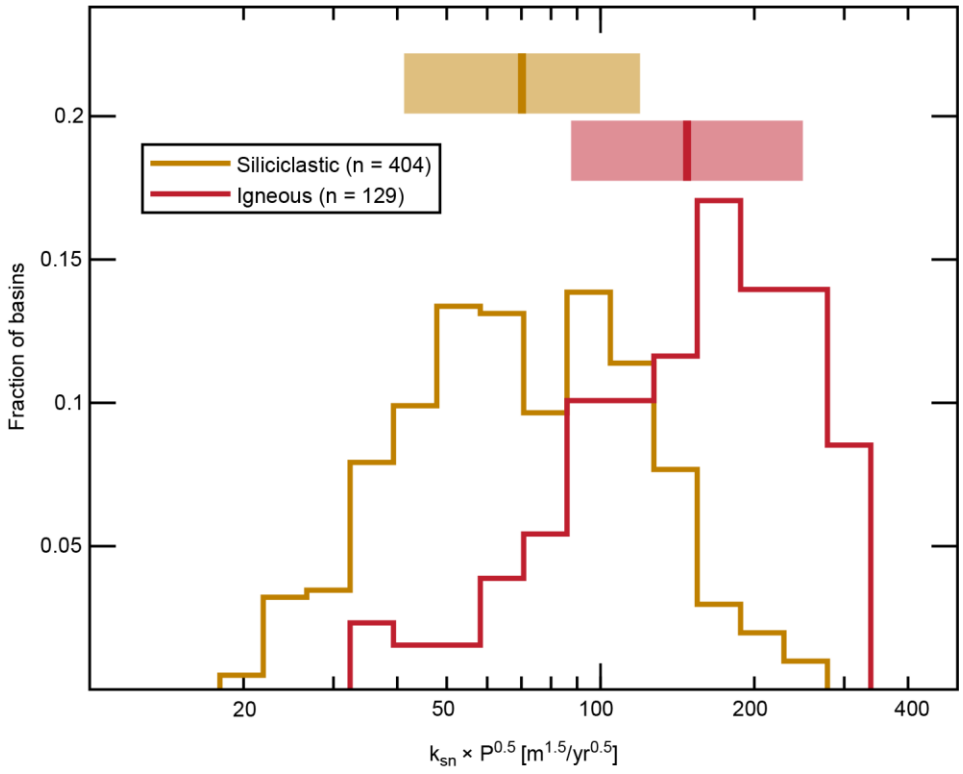

Figure 1.S2: Histograms of precipitation-adjusted steepness for the Oregon Coast Range, separated by lithology. Igneous basins are on average 112±22% higher with respect to this quantity than siliciclastic basins (p<0.0001).

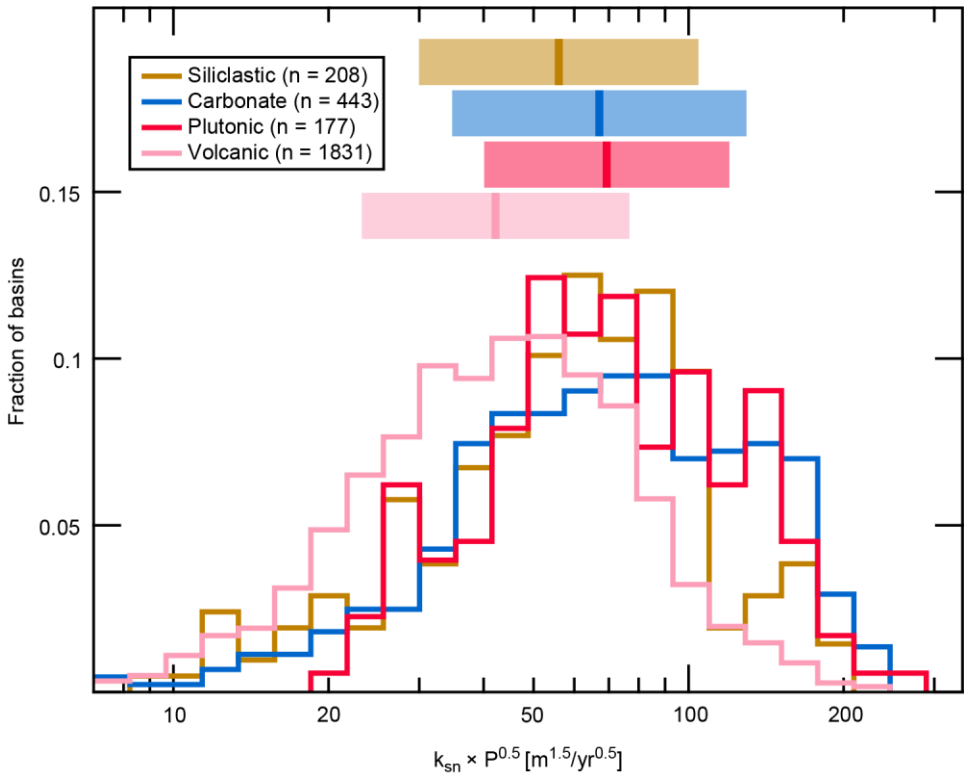

Figure 1.S3: Histograms of precipitation-adjusted steepness for the Nevada Basin and Range, separated by lithology. With respect to this quantity, plutonic basins are on average 65±14% steeper than volcanic (p<0.0001), 25±15% steeper than siliciclastic (p<0.001), and 4±11% steeper than carbonate (p=0.52). Carbonate basins are on average 59±11% steeper than volcanic (p<0.0001) and 21±13% steeper than siliciclastic (p<0.001). Siliciclastic basins are 33±12% steeper than volcanic (p<0.0001).

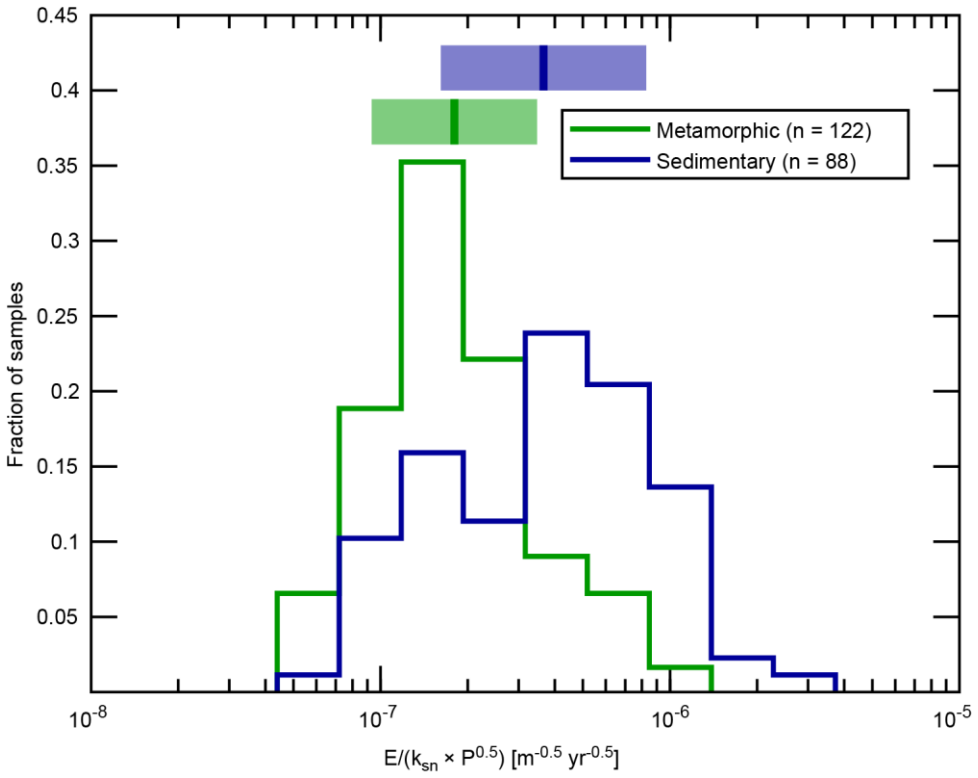

Figure 1.S4: Histograms of precipitation-adjusted K_{eff} for the Appalachian Mountains, separated by lithology. Sedimentary basins are on average 103±45% higher with respect to this quantity than metamorphic basins (p<0.0001).

Table 1.S1: Cosmogenic erosion rates and sample data for the Tennessee River and Chattooga River basins.

Sample ID	River	Longitude	Latitude	Drainage area (km^2)	^{10}Be concentration (atoms/g)	^{10}Be uncertainty (1σ, atoms/g)	Erosion rate (m/Myr)	Erosion rate uncertainty (m/Myr)
TEN18-01	Betty Creek	34.97668	-83.43471	32.3	459400	9900	10	0.84
TEN18-02	Ledford Branch	35.15237	-83.25957	2.8	327800	9300	14.7	1.26
TEN18-03	Walnut Creek	35.13922	-83.27246	15.6	302700	6500	15.9	1.32
TEN18-04	Cullasaja River	35.12205	-83.28171	121.7	368900	10500	13	1.12
TEN18-05	Big Creek	35.08174	-83.20662	11.1	427300	8500	11	0.92
TEN18-06	Catheys Creek	35.21316	-82.78721	21.5	385500	7800	12.4	1.04
TEN18-07	Kuykendall Creek	35.21390	-82.78528	7.5	451800	10800	10.7	0.91
TEN18-08	Rice Creek	36.01004	-82.56195	15.5	291300	9000	17.2	1.48
TEN18-09	Rocky Fork	36.04808	-82.56071	22.2	415200	10700	11.4	0.97
TEN18-10	Jones Branch	36.09970	-82.43103	5.9	271800	8000	18.3	1.57
TEN18-11	Nolichucky River	36.10135	-82.44807	1644.1	242100	8300	19.4	1.70
TEN18-12	Hollow Poplar Creek	36.08955	-82.33287	12.6	486900	10700	9.94	0.84
TEN18-13	North Toe River	36.04043	-82.30597	1134.0	273700	7400	18.2	1.55
TEN18-14	Hurricane Creek	35.72093	-83.02543	22.1	296400	8200	16.7	1.43
TEN18-15	Pigeon River	35.52446	-82.84420	335.7	325900	16400	15.3	1.46
TEN18-16	Spring Creek	35.87727	-82.83523	182.2	276500	6100	18.4	1.53
TEN18-17	Paint Creek	35.94735	-82.89468	63.8	457000	10800	10.9	0.93
TEN18-18	Flat Creek	35.73142	-82.59518	41.6	510600	12500	9.44	0.81
TEN18-19	Worse Creek	34.74100	-83.35861	1.4	381500	7900	13.2	1.10
TEN18-20	Unnamed	34.74333	-83.35871	0.1	91400	3000	58.4	5.02
TEN18-21	Unnamed	34.74742	-83.37509	0.6	415800	9600	11.9	1.00

2. Ongoing river capture in the Amazon

A version of this chapter was published in *Geophysical Research Letters*, with the indication that the first two authors contributed equally to this work. The formatted version can be found online; please use the citation below when referring to this work. Reprinted with permission from American Geophysical Union.

Stokes, M. F., Goldberg, S. L., & Perron, J. T. (2018). Ongoing river capture in the Amazon. Geophysical Research Letters, 45(11), 5545-5552. https://doi.org/10.1029/2018GL078129

Abstract

River capture is thought to trigger abrupt changes in evolving continental drainage systems, but it is almost always inferred rather than observed, and the mechanisms that lead to capture are unclear. We shed light on these mechanisms by documenting an ongoing capture involving major South American rivers. The Rio Casiquiare is a distributary of the Rio Orinoco and a tributary of the Rio Negro; it forms a perennial water connection between the drainage basins of the Amazon and Orinoco, the largest and fourth-largest rivers on Earth by discharge. This unusual configuration is the result of an incomplete and ongoing river capture, in which the Rio Negro is capturing the upper Rio Orinoco. We describe a positive feedback between diversion of water into the capturing channel and sedimentation within the channel being captured, a mechanism that could drive river capture in the Amazon and elsewhere.

2.1. Introduction

River networks have long been recognized as dynamic features of Earth's surface (Davis, 1899; Gilbert, 1877; Thompson, 1939). As surface processes respond to climate and tectonics, continental landscapes are reshaped by shifting drainage divides and topological reorganization of river networks (Willett et al., 2014). Such changes are driven by a combination of two end-member mechanisms, divide migration and river capture. Divide migration occurs when a difference in erosion rates across a drainage divide continuously pushes the divide, changing basin geometry. River capture occurs when a river breaches a drainage divide to reroute the upstream portion of a neighboring river basin, preserving the drainage geometry while changing the topology of the river network. River captures facilitate geologically rapid changes to continental landscapes (Prince et al., 2011; Shugar et al., 2017) and have been shown to play a

role in the distribution of freshwater organisms (Bossu et al., 2013; Craw et al., 2007; Kozak et al., 2006). Despite the importance of river captures, the processes that drive them are not well understood.

Past river captures are commonly recognized by circumstantial evidence such as barbed tributaries, wind gaps, or knickzones in river elevation profiles (Bishop, 1995; Clark et al., 2004; Davis 1889; Johnson, 1907; Willett et al., 2014; Yanites et al., 2013). In some cases, there is more direct evidence of capture, such as sediment provenance (Prince et al., 2011) or preserved fluvial terraces that can be used to deduce intermediate stages of capture (Brocard et al., 2011). Shugar et al. (2017) documented a rare example of an active capture, which occurred when a retreating glacier caused a drainage divide to change unusually rapidly. Direct evidence or observations of capture in purely fluvial settings are even less common.

In this paper, we present evidence that the Rio Casiquiare in South America is driving an ongoing river capture. In Section 2.2, we synthesize geological, biological and hydrological evidence from the region to reveal the ongoing, tectonically driven river network reorganization controlling the Casiquiare capture. We then use observations and simple hydraulic calculations in Section 2.3 to assess the local causes and dynamics of this lowland river capture.

2.2. Geologic setting

2.2.1. The Rio Casiquiare

The Rio Casiquiare is a 355-km-long river in southern Venezuela within the Amazon rainforest (Figure 2.1a). It originates at a bifurcation of the Rio Orinoco as a distributary, and at its confluence with the Rio Guainía forms the Rio Negro, a major tributary of the Amazon River. A perennial connection between two large drainage basins is highly unusual – indeed, the French

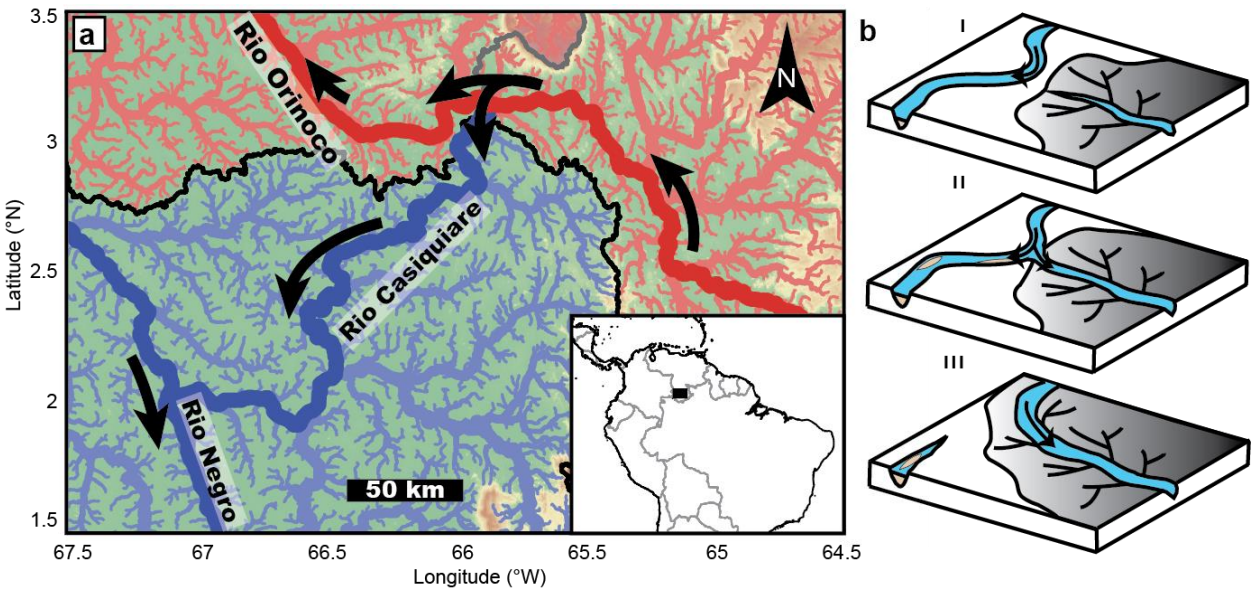

Figure 2.1. (a) Map of the Rio Casiquiare with rivers and flow directions indicated. The black line is the present boundary of the Amazon basin; the gray line is the future boundary once the capture is complete. **(b)** Schematic representation of the hypothesized capture process. I) pre-capture; II) present bifurcation; III) future complete capture. Shading denotes the Amazon basin.

geographer Philippe Buache ridiculed an initial report of the channel as a "monstrous error of geography" (von Humboldt, 1877). As a result, it has long attracted the interest of explorers and scientists (López, 1956; Rice, 1921; Stern, 1970; Sternberg, 1975; von Humboldt & Bompland, 1829; Winemiller et al., 2008), several of whom have interpreted the perennial connection as a river capture in progress (Figure 2.1b). Despite these past suggestions of active capture, there has not been a study of the mechanisms that could be driving such a process.

2.2.2. South American drainage reorganization

The Orinoco and Amazon drainage basins have experienced extensive changes since the onset of Andean orogeny. During the early Miocene period the present upper Amazon basin may have flowed northward to the Caribbean Sea through a paleo-Orinoco River (Hoorn et al., 1995; Hoorn et al., 2010) or alternatively drained into a subsiding continental basin east of the Andes (Latrubesse et al., 2010). In the late Miocene period (Figueiredo et al., 2009; Hoorn et al., 2017) or early Pliocene (Latrubesse et al., 2010) the upper Amazon breached its eastern divide to

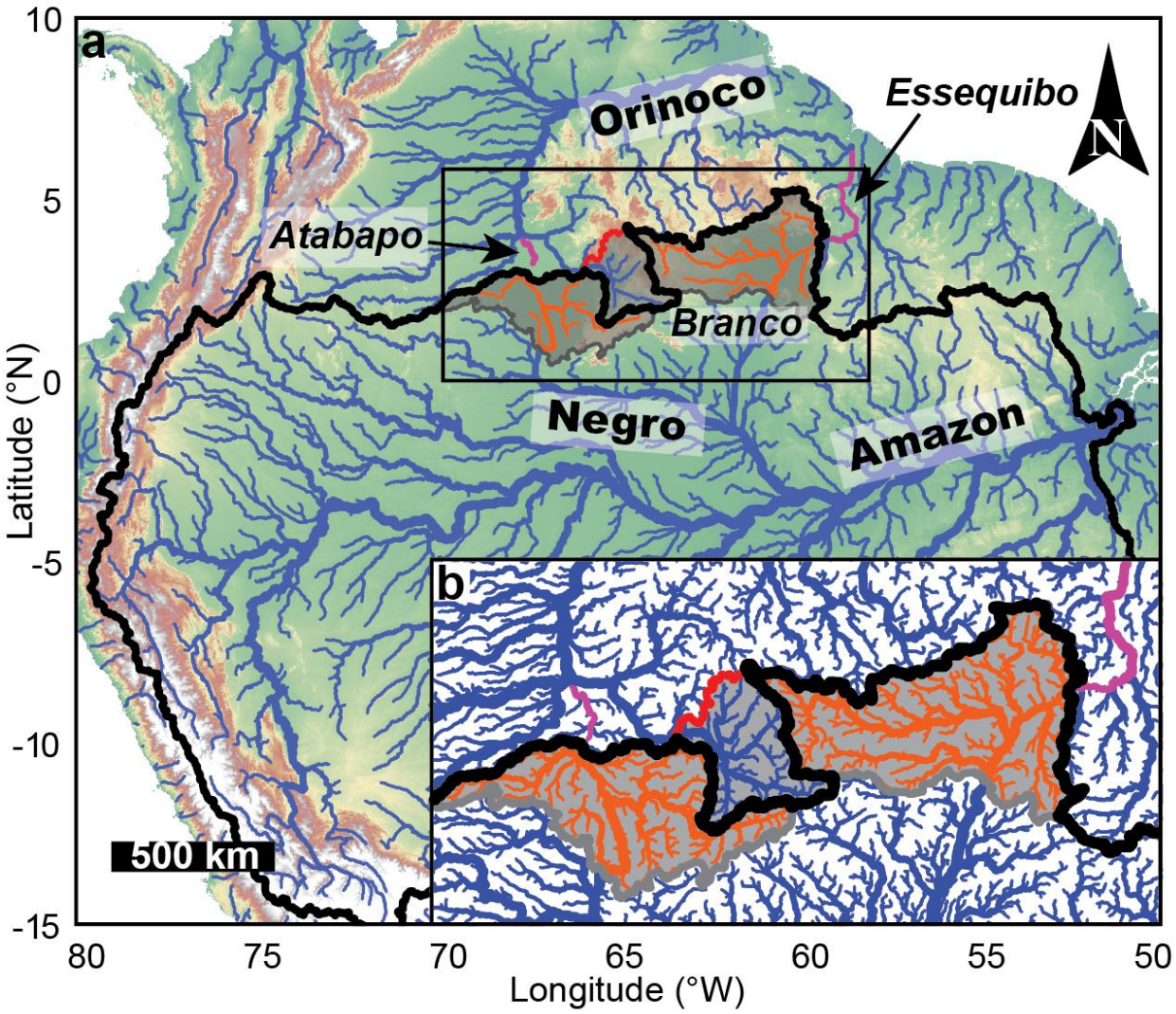

Figure 2.2: (a) Map of the Amazon basin showing past and ongoing expansion of the basin through river capture. Bold black line traces the present boundary of the Amazon basin. Red line shows the future position of the boundary upon completion of the capture of the upper Rio Orinoco by the Rio Casiquiare; gray lines show past positions of divides inferred from captures. Shading denotes area gained by the Amazon through the three captures discussed in the text. The rivers plotted in orange are captured reaches; the rivers plotted in magenta are those that lost drainage area. **(b)** Enlarged map of the northern divide.

establish its present course. The integration of the upper Amazon basin with the Atlantic drainage increased the discharge, and thus the erosive power, of the mainstem Amazon. The subsequent entrenchment of the mainstem Amazon steepened its tributaries, causing them to erode faster than neighboring basins. At the same time, ongoing sedimentation from the Andes filled in low-lying areas and reduced relief along the northern Amazon drainage divide. We

suggest that this combination of accelerated erosion and decreased divide relief facilitated the lateral expansion of the Amazon basin. Biologic and geologic evidence of captures from the neighboring Rio Essequibo and Rio Atabapo (Lovejoy & de Araújo, 2000; Lujan & Armbruster, 2011; Sivasundar et al., 2001; Turner et al., 2004) supports a regional trend of northward motion of the divide (Figure 2.2).

2.3. The Rio Casiquiare capture

Currently, the bifurcation of flow in the Rio Orinoco routes approximately 25% of the discharge from the upper Rio Orinoco into the Rio Casiquiare (USACE, 1943). If the capture proceeds until completion, the present-day upper Orinoco will be completely diverted to the Rio Negro (Figure 2.1b), resulting in an exchange of roughly 40,000 km^2 of drainage area (Figure 2.2). We suggest two driving mechanisms behind such a capture. First, headward incision of the proto-Rio Casiquiare established an active connection between the two river systems (Section 2.3.1). Second, now that interbasin flow occurs, the dynamics of flow and sediment transport through the bifurcation will divert progressively more discharge from the Orinoco into the Casiquiare. In Section 2.3.2, we use hydraulic calculations to assess the hypothesis that the Rio Casiquiare will eventually become the dominant channel.

2.3.1. Headward advance of the proto-Rio Casiquiare

The establishment of the perennial connection between the Rio Casiquiare and the Orinoco required headward incision by the proto-Rio Casiquiare that progressed at a faster rate than Rio Orinoco tributaries. The Rio Casiquiare is more than twice as steep as the Rio Orinoco downstream of the bifurcation (Figure 2.3), which may have hastened the headward incision of the proto-Casiquiare. The eventual establishment of the bifurcation was likely aided by the

combination of low-relief topography and high discharge, particularly at the annual flood stage. The annual variation in river stage at the bifurcation is ~4 m (USACE, 1943) and during a period of satellite observation from 2003 – 2013 the stage varied by up to 6.5 m in the Rio Casiquiare downstream of the bifurcation (ORE-HYBAM Station ENV951 located at 2.4°N 66.5°W; Cochonneau et al., 2006). The modern topographic divide lies only 3-10 m above the Rio Orinoco at low flow as measured by SRTM in February 2000 (Farr et al., 2007; Lehner et al., 2008) (Figure 2.3), and is thus readily breached at flood stage. We hypothesize that as seasonal overflow breached and eroded the divide, the Rio Casiquiare branch was favored due to its steeper slope. At some point seasonal flooding of the divide became a perennial connection.

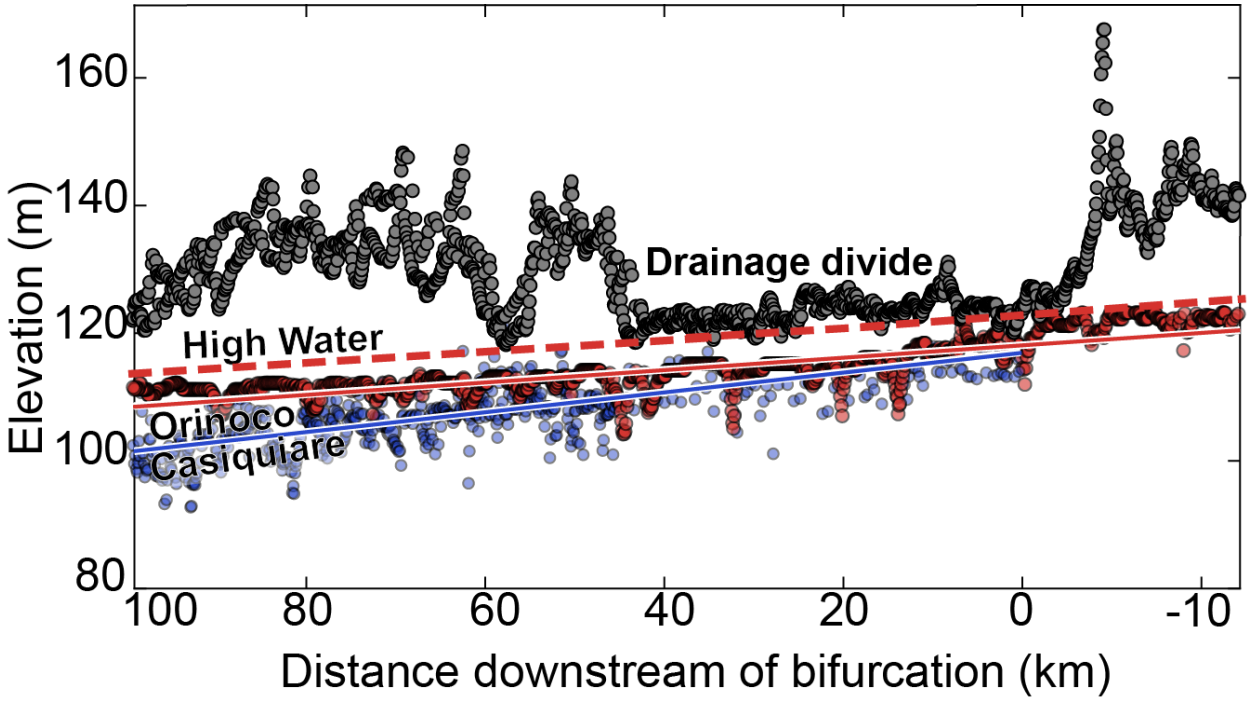

Figure 2.3. Elevation profiles of the Rio Casiquiare (blue), Rio Orinoco (red), and the drainage divide (gray) in the area of the bifurcation. The scatter in the river profiles is due to noise in the SRTM topography; least-squares regression lines are shown to emphasize the average channel slopes. High water (dashed red line) is shown for a stage increase of 4 m.

2.3.2. Bifurcation dynamics

Now that the bifurcation is established, the completion of the capture will depend on the dynamics of the bifurcation in addition to the downstream evolution of the Orinoco and Rio Negro. Although there are no other mid-continent river connections of comparable scale worldwide (Winemiller & Willis, 2011), bifurcations in other lowland river settings offer physical analogs. Bifurcations are dynamic and can change on timescales of days to millennia as the interactions between discharge, erosion, and sedimentation cause one of the channels to become the dominant or only channel. The stability of the bifurcation is a function of the capacity of each channel to convey the water and sediment supplied to it (Edmonds & Slingerland, 2008; Fisk, 1952; Kleinhans et al., 2012; van Denderen et al., 2017).

We use existing measurements of channel geometry and flow characteristics to study the partitioning of discharge through the bifurcation and to assess whether or not the system is progressing towards a complete capture. Data collected by the United States Army Corps of Engineers in a 1943 report on navigability of the Rio Orinoco and Rio Casiquiare (USACE, 1943) include longitudinal bed and water surface profiles, discharge, surface velocity, and channel cross sections below the bifurcation on each branch (Figure 2.4). These data allow us to estimate downstream gradients of bed shear stress through each branch of the bifurcation, which we use as a proxy for erosion or aggradation.

Assuming steady, uniform flow, we approximate basal shear stress (τ_b) at each cross-section during low and bankfull flow as

$$\tau_b = \rho g R_h S, \quad (1)$$

where ρ is water density (1000 kg/m^3), g is gravitational acceleration, S is the water surface slope, and R_h is the hydraulic radius. Downstream of the bifurcation, we measured R_h from

channel cross sections surveyed by the USACE. Upstream of the bifurcation there is no cross-sectional survey from which to measure R_h, so we use the following simple hydraulic calculations to estimate its value from other measurements. The Orinoco channel downstream of the bifurcation has a nearly rectangular cross-section with a width-to-depth ratio of approximately 80 (Figure 2.4b). We assume that the Orinoco channel upstream of the bifurcation is also nearly rectangular and much wider than it is deep, such that R_h is approximately equal to cross-sectionally averaged flow depth (H), which is in turn related to discharge (Q), channel width (W) and cross-sectionally averaged velocity ($\bar{u}$) by

$$R_h \approx H = \frac{Q}{\bar{u}W}. \tag{2}$$

Channel width upstream of the bifurcation is measured from Google Earth imagery (a-a′ in Figure 2.4). We use two different estimates of discharge upstream of the bifurcation: the first is a USACE low-water discharge measurement upstream of the bifurcation at Tama-Tama; the second is estimated by adding together USACE discharge measurements at the time of the 1943 survey downstream of the bifurcation in each channel (b-b′ and c-c′ in Figure 2.4).

We next estimate cross-sectionally averaged flow velocity ($\bar{u}$ in equation 2). To assess the robustness of the results, we employ two empirical approaches that differ in how they relate velocity to flow depth, channel slope and resistance. First, we use Manning's equation,

$$\bar{u} = \frac{1}{n} H^{\frac{2}{3}} S^{\frac{1}{2}} \tag{3}$$

where n is a dimensional flow resistance parameter. Substituting equation (3) into equation (2) and solving for H yields

$$H = \left(\frac{nQ}{WS^{\frac{1}{2}}} \right)^{\frac{3}{5}}. \tag{4}$$

The value of Manning's *n* is estimated by applying equation (3) to the Orinoco downstream of the bifurcation (b-b′ in Figure 2.4) with $\bar{u}$ taken to be the cross-sectionally averaged velocity calculated from the discharge and cross-sectional area measured by the USACE in the 1943 survey. Second, we use the Darcy-Weisbach equation,

$$\bar{u} = \sqrt{\frac{8gHS}{f}}, \tag{5}$$

where *f* is a dimensionless friction factor. Substituting equation (5) into equation (2) and solving for *H* yields

$$H = \left(\frac{Q}{W}\right)^{\frac{2}{3}} \left(\frac{f}{8gS}\right)^{\frac{1}{3}}. \tag{6}$$

We estimate *f* from the empirical relationship of Leopold et al. (1964),

$$\frac{1}{\sqrt{f}} = 2.0 \log\left(\frac{H}{D_{84}}\right) + 1.0 \tag{7}$$

where D_{84} is the 84th percentile diameter of the bed sediment. We use the value of D_{84} that gives the correct flow depth for the downstream Rio Orinoco at survey water level; this value falls within the sand size class. The implicit dependence on *H* introduced by equation (7) requires an iterative solution.

The two estimates of *Q* (low-water and 1943 survey level) and the two methods of estimating *H* (Manning and Darcy-Weisbach) give four flow depth estimates for the upstream Rio Orinoco (a-a′). Using the measured water surface slopes, measured flow depths below the bifurcation, and estimated flow depths above the bifurcation, we then calculate the bed shear stress using equation (1) at each location for three different flow conditions: 1943 low water, the survey water level, and high water. The high-water flow stage is estimated to be 4 m above the survey water level based on a marker observed by the USACE upstream of the bifurcation at

Table 2.1. Values used in hydraulic calculations.

	Orinoco, upstream (a-a′)	Orinoco, downstream (b-b′)	Casiquiare (c-c′)
S (slope) (m/m)	4.31×10^{-5}	4.31×10^{-5}	8.72×10^{-5}
Channel width (m)	399[a]	254	87
Q (discharge) (m^3/s)			
Low Water	580	-	-
Survey level	*1052*[b]	816	236
D_{84} (grain size) (mm)	0.75[c]	0.75[c]	-
Friction factor			
Manning's *n* / Darcy-Weisbach *f*	*0.0167 / 0.0147*	*0.0167 / 0.0147*	-
R_h(hydraulic radius) (m)			
Low water	*2.19 / 2.15*	2.93	3.51
Survey level	*3.13 / 3.11*	3.53	4.43
τ_b (bed shear stress) (Pa)			
Low water	*0.926 / 0.909*	*1.24*	*3.00*
Survey level	*1.32 / 1.31*	*1.49*	*3.79*
High water	*3.01 / 3.00*	*3.18*	*7.21*
Downstream shear stress gradient (Pa/km)			
Low water		*0.240 / 0.253*	*1.67 / 1.68*
Survey level		*0.130 / 0.138*	*1.99 / 1.99*
High water		*0.130/ 0.138*	*3.38 / 3.38*

Note. Italicized values are our calculations; other values are measured parameters (USACE measurements unless specified otherwise). Where there are two values reported they represent the Manning and Darcy-Weisbach methods for estimating flow depth (*Manning / Darcy-Weisbach*). Letters in column headings refer to cross-sections in Figure 2.4.

[a]Estimated from Google Earth. [b]Summation of the two measured downstream discharges; no upstream measurement. [c]Used to calculate Darcy-Weisbach friction factor.

Tama-Tama. We apply this observed stage increase uniformly to all three locations. The water surface slope is kept constant for all calculations as it was only surveyed once. Values used in the calculations and the resulting shear stress estimates are listed in Table 2.1.

Using these shear stress estimates, we then calculate a longitudinal shear stress gradient along each channel by dividing the difference in shear stress (downstream minus upstream) between the measured locations by the distance along the channel centerline. The shear stress increases from the upstream Rio Orinoco (a-a′ in Figure 2.4) through the bifurcation into the downstream Rio Casiquiare (c-c′ in Figure 2.4), with calculated gradients ranging from 1.67 to 3.38 Pa/km. The shear stress also increases through the downstream Rio Orinoco (b-b′ in Figure

2.4), but the estimated gradients range from 0.130 to 0.253 Pa/km, roughly an order of magnitude smaller than for the Rio Casiquiare. The magnitudes of the shear stress gradients depend on which estimates of *H* are used in the calculation, with a larger difference in gradients between the two branches at higher water levels (Table 2.1).

Sediment transport capacity per unit channel width is positively related to the bed shear stress (e.g. Engelund & Hansen, 1967). In a transport-limited regime, vertical changes in bed height therefore depend on the downstream gradient in shear stress. The downstream-increasing shear stress in the Rio Casiquiare through the bifurcation at the survey level and high flow suggests that the bed of the Rio Casiquiare is eroding. The comparatively minor downstream increase in shear stress through the Rio Orinoco even at high flow suggests relatively little potential for bed erosion. There may even be aggradation within the Rio Orinoco, as evidenced by the presence of a large deposit of sediment immediately downstream of the bifurcation, which is visible in satellite imagery (inset, Figure 2.4) and was observed by Stern (1970). This hydraulic analysis suggests that the steeper slope, deeper channel, and larger shear stress within the Rio Casiquiare will eventually cause it to become the dominant channel in the bifurcation, leading to complete capture of the upper Rio Orinoco.

2.4. Discussion: Implications for drainage capture

The Rio Casiquiare, a rare example of an incomplete drainage capture, can inform our understanding of the mechanisms by which captures occur, in the Amazon basin and beyond. Models of capture in bedrock landscapes typically invoke headward incision by a more rapidly eroding channel (Bishop, 1995). However, the observation that channels fed by surface runoff require a minimum drainage area to form and incise (Montgomery & Dietrich, 1992) has led

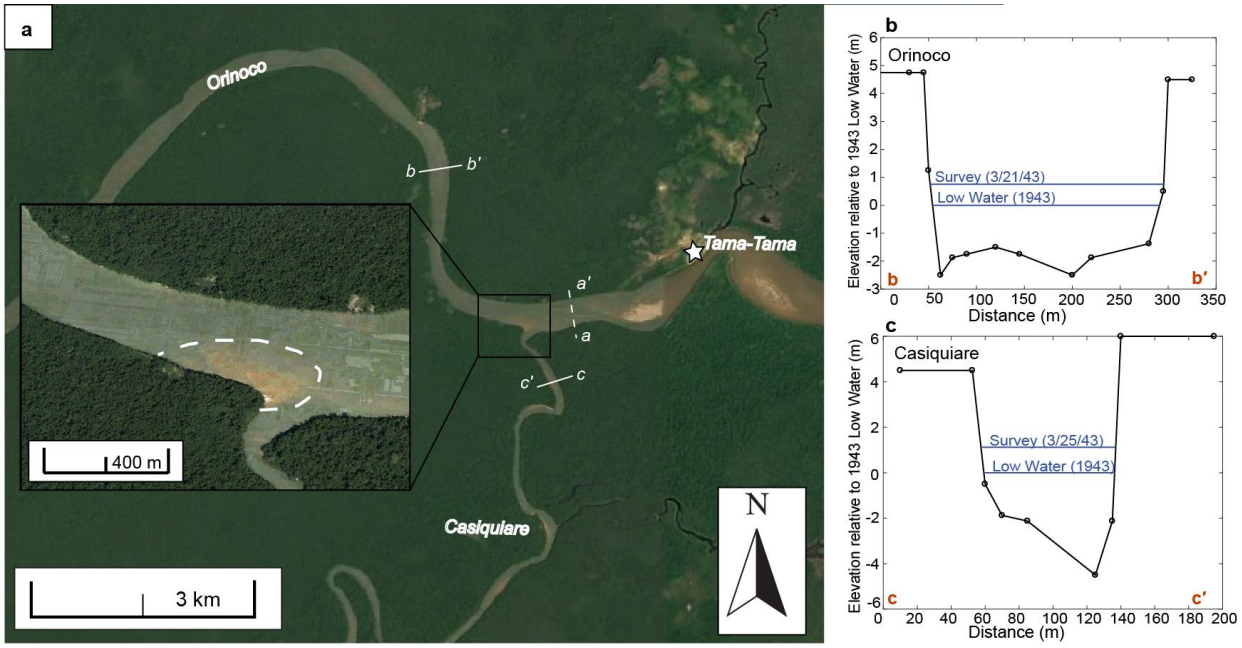

Figure 2.4. (a) Satellite image of the bifurcation of the Rio Casiquiare from the Rio Orinoco (3.139° N, 65.880° W). Locations of the USACE cross-sections and velocity measurements (b-b′ and c-c′) are marked with solid white lines. The cross-section where we perform calculations upstream of the bifurcation (a-a′) is marked with a white dashed line. The inset highlights the bifurcation with an area of in-channel sedimentation (white dashed line) in response to loss of discharge to the downstream Rio Orinoco. Images from Google and DigitalGlobe. Surveyed cross-sections b-b′ and c-c′ are plotted in **(b)** and **(c)**.

some authors to question how a channel can erode through a divide by headward incision alone (Bishop, 1995). In some bedrock landscapes, groundwater piracy may accelerate mass wasting and erosion of the divide (Brocard et al., 2011; Yanites et al., 2013). Another possibility is that damming or sedimentation in the captured channel plays an active role in capture by diverting water to a neighboring basin.

In the case of the Rio Casiquiare, we propose that capture is ultimately driven by headward erosion of a steeper Rio Negro tributary, and that the difference in slope between the two channels will be responsible for complete diversion of the Rio Orinoco into the Rio Casiquiare. However, in-channel sedimentation in the Orinoco and flooding at high discharge also play critical roles in governing the mechanism and duration of river capture. Sedimentation

in the Rio Orinoco downstream of the bifurcation has enhanced the local difference in slopes between the two channels and promoted re-routing of water during seasonal flooding. The longevity of the Casiquiare bifurcation (at least centuries) suggests that capture in alluviated lowlands is not instantaneous, but rather a multi-stage process in which water, sediment and biota are transported over major watershed boundaries on timescales that are relevant for the evolutionary history of aquatic organisms (Winemiller & Willis, 2011).

River captures are often discussed in the context of bedrock channels (e.g. Prince et al., 2011; Yanites et al., 2013). However, the sizes of lowland alluvial captures may far exceed those of bedrock headwater channels. For example, the 40,000 km^2 of drainage area being exchanged in the Casiquiare-Orinoco capture is roughly 100 times larger than a prominent capture in the southeast Appalachians in a dominantly bedrock system (Prince et al., 2011). If the Rio Casiquiare capture is completed, the three captures shaded in Figure 2.2 will represent a combined increase in the Amazon basin's drainage area of roughly 250,000 km^2 and a shift in the drainage divide of about 200 km. Since past captures become more difficult to identify with age, there were likely other earlier captures that contributed to the northward expansion of the Amazon basin that are no longer clearly recognizable. This history of inter-basin flow has allowed biological dispersal and gene flow between the Amazon and Orinoco basins (Willis et al., 2010; Winemiller et al., 2008), suggesting that river capture may have played a role in enhancing the biodiversity of the region, one of the most diverse freshwater environments in the world (Albert & Carvalho, 2011).

2.5. Conclusions

River capture is a phenomenon widely inferred from unexpected patterns in topography, sedimentary provenance and biogeography, but it is rarely observed directly. We show that the Rio Casiquiare is actively capturing the upper Rio Orinoco, driven by a combination of in-channel sedimentation in the Rio Orinoco and seasonal inundation of the drainage divide that favors the steeper Rio Casiquiare. Although the bifurcation has existed for centuries, our analysis suggests that the steeper slope of the Rio Casiquiare will eventually cause it to become the dominant channel. The Rio Casiquiare appears to be the most recent in a series of similar captures by the Amazon River that have substantially influenced the landscape of South America.

Acknowledgements

We thank Jaap Nienhuis for sparking our interest in the Rio Casiquiare and an anonymous reviewer for helpful suggestions. We acknowledge support from the National Science Foundation Graduate Research Fellowship Program under Grant No. 1122374 (MFS); the MIT Ida Green Fellowship (MFS); MIT Praecis Presidential Fellowship (SLG); and the Patrick Hurley Fellowship (SLG). Figures 2.1 and 2.2 were generated using TOPOToolbox (Schwanghart & Scherler, 2014) using river network and elevation data from SRTM/HydroSHEDS (Lehner et al. 2008).

References

Albert J.S., & Carvalho T.P. (2011). Neogene Assembly of Modern Faunas. In J.S. Albert & R.E. Reis (Eds.), *Historical Biogeography of Neotropical Freshwater Fishes* (pp. 119-136). Berkeley, CA: University of California Press.

Bishop P. (1995). Drainage rearrangement by river capture, beheading and diversion. *Progress in Physical Geography, 19*(4), 449-473. https://doi.org/10.1177/030913339501900402

Bossu, C.M., Beaulieu, J.M., Ceas, P.A., & Near, T.J. (2013). Explicit tests of paleodrainage connections of southeastern North America and the historical biogeography of Orangethroat Darters (Percidae: *Etheostoma: Ceasia*). *Molecular Ecology*, *22*(21), 5397-5417. https://doi.org/10.1111/mec.12485

Brocard, G., Teyssier, C., Dunlap, W.J., Authemayou, C. Simon-Labric, T., Cacao-Chiquín, E.N., et al., (2011). Reorganization of a deeply incised drainage: role of deformation, sedimentation and groundwater flow. *Basin Research*, *23*(6), 631 – 651. https://doi.org/10.1111/j.1365-2117.2011.00510.x

Clark, M.K., Schoenbohm, L.M., Royden, L.H., Whipple, K.X., Burchfiel, B.C., Zhang, X., et al. (2004). Surface uplift, tectonics and erosion of eastern Tibet from large-scale drainage patterns. *Tectonics*, *23*(1), TC1006. https://doi.org/10.1029/2002TC001402

Cochonneau, G., Sondag, F., Guyot, G., Geraldo, B., Filizola, N., Fraizy, P., et al. (2006). The environmental observation and research project, ORE HYBAM, and the rivers of the Amazon basin: *Climate Variability and Change – Hydrological Impacts (IAHS Publication)*, *308*, 44-50.

Craw, D., Burridge, C., Anderson, L., & Waters, J.M. (2007). Late Quaternary river drainage and fish evolution, Southland, New Zealand. *Geomorphology*, *84*(1-2), 98-110. https://doi.org/10.1016/j.geomorph.2006.07.008

Davis W.M. (1889). A river-pirate. *Science*, *13*(314) , 108-109. https://doi.org/10.1126/science.ns-13.314.108

Davis, W.M. (1899). The geographical cycle. *The Geographical Journal*, *14*(5), 481 – 504. https://doi.org/10.2307/1774538

Edmonds, D.A., & Slingerland, R.L. (2008). Stability of delta distributary networks and their bifurcations. *Water Resources Research*, *44*(9), W09426. https://doi.org/10.1029/2008WR006992

Engelund, F., & Hansen, E. (1967). *A monograph on sediment transport in alluvial streams.* Copenhagen, Denmark: Teknisk Forlag.

Farr, T., Rosen, P.A., Caro, E., Crippen, R., Duren, R., Hensley, S., et al. (2007). The shuttle radar topography mission. *Reviews of Geophysics*, *45*(2), RG2004, https://doi.org/10.1029/2005RG00018

Figueiredo, J., Hoorn, C., van der Ven, P., & Soares, E. (2009). Late Miocene onset of the Amazon River and the Amazon deep-sea fan: Evidence from the Foz do Amazonas Basin. *Geology*, *37*(7), 619-622. https://doi.org/ 10.1130/G25567A.1

Fisk, H.N. (1952). *Geological Investigation of the Atchafalaya Basin and the Problem of Mississippi Diversion*. Vicksburg, MS: Mississippi River Commission, Waterways Experiment Station.

Gilbert, G.K. (1877). *Report on the Geology of the Henry Mountains*. Washington, DC: US Government Printing Office.

Hoorn, C., Botogá-A, G.R., Romero-Baez, M., Lammerstma, E.I., Flantua, S.G.A., Dantas, E.L., et al. (2017). The Amazon at sea: Onset and stages of the Amazon River from a marine record, with special reference to Neogene plant turnover in the drainage basin, *Global and Planetary Change*, *153*, 51-65. https://doi.org/10.1016/j.gloplacha.2017.02.005

Hoorn, C., Guerrero, J., Sarmiento, G.A., and Lorente, M.A. (1995). Andean tectonics as a cause for changing drainage patterns in Miocene northern South America. *Geology*, *23*(3), 237-240. https://doi.org/10.1130/0091-7613(1995)023<0237:ATAACF>2.3.CO;2

Hoorn, C., Wesselingh, F.P., ter Steege, H., Bermudez, M.A., Mora, A., Sevink, J., et al. (2010). Amazonia through time: Andean uplift, climate change, landscape evolution, and biodiversity. *Science*, *330*(6006), 927-931. https://doi.org/10.1126/science.1194585

Johnson, D.W. (1907). River capture in the Tallulah district, Georgia. *Science*, *25*(637), 428 – 432. https://doi.org/ 10.1126/science.25.637.428-a

Kleinhans, M.G., Ferguson, R.I., Lane, S.N., & Hardy, R.J. (2012). Splitting rivers at their seams: bifurcations and avulsion. *Earth Surface Processes and Landforms*, *38*(1), 47-61. https://doi.org/10.1002/esp.3268

Kozak, K.H., Blaine, R.A., & Larson, A. (2006). Gene lineages and eastern North American paleodrainage basins: phylogeography and speciation in salamanders of the *Eurycea bislineata* species complex. *Molecular Ecology*, *15*(1), 191-207. https://doi.org10.1111/j.1365-294X.2005.02757.x

Latrubesse, E.M., Cozzuol, M., da Silva-Caminha, S.A.F., Rigsby, C.A., Absy, M.L., Jaramillo, C. (2010). The Late Miocene paleogeography of the Amazon Basin and the evolution of the Amazon River system. *Earth Science Reviews, 99(3-4)*, 99-124. https://doi.org/10.1016/j.earscirev.2010.02.005

Lehner, B., Verdin, K., & Jarvis, A. (2008). New global hydrography derived from spaceborne elevation data. *Eos (Transactions, American Geophysical Union), 89*(10), 93-94. https://doi.org/10.1029/2008EO100001

Leopold, L.B., Wolman, M.G., & Miller, J.P. (1964). *Fluvial processes in geomorphology*. San Francisco, CA: W.H. Freeman and Company.

López V.M. (1956). Venezuela. In F.W. Jenks (Ed.), *Handbook of South American Geology: An Explanation of the Geologic Map of South America, Memoirs of the Geological Society of Americas* (Vol 65, pp. 331-340). Boulder, CO: Geological Society of the Americas. https://doi.org/10.1130/MEM65

Lovejoy, N.R., & de Araújo M.L.G. (2000). Molecular systematics, biogeography and population structure of Neotropical freshwater needlefishes of the genus *Potamorrhaphis*. *Molecular Ecology*, *9*(3), 259–268. https://doi.org/10.1046/j.1365-294x.2000.00845.x

Lujan, N.K., & Armbruster, J.W. (2011). The Guiana Shield. In J.E. Albert & R.E. Reis (Eds.), *Historical Biogeography of Neotropical Freshwater Fishes* (pp. 211 – 224). Berkeley, CA: University of California Press.

Montgomery, D.R. & Dietrich, W.E. (1992). Channel initiation and the problem of landscape scale. *Science, 255*(5046), 826 – 830. https://doi.org/ 10.1126/science.255.5046.826

Prince, P.S., Spotila, J.A., & Henika, W.S. (2011). Stream capture as driver of transient landscape evolution in a tectonically quiescent setting. *Geology*, *39*(9), 823 – 826. https://doi.org/10.1130/G32008.1

Rice, A.H. (1921). The Rio Negro, the Rio Casiquiare, and the upper Orinoco, September 1919-April 1920. *The Geographical Journal*, *58*(5), 321-343. https://doi.org/ 10.2307/1780880

Schwanghart, W., & Scherler, D. (2014). TopoToolbox 2 – MATLAB-based software for topographic analysis and modeling in Earth surface sciences. *Earth Surface Dynamics, 2*(1), 1 – 7. https://doi.org/10.5194/esurf-2-1-2014

Shugar, D.H., Clague, J.J., Best, J.L., Schoof, C., Willis, M.J., Copland, L., & Roe, G.H. (2017). River piracy and drainage basin reorganization led by climate-driven glacier retreat. *Nature Geoscience*, *10*(5), 370 – 375. https://doi.org/ 10.1038/ngeo2932

Sivasundar, A., Bermingham, E., & Orti, G. (2001). Population structure and biogeography of migratory freshwater fishes (*Prochilodus: Characiformes)*. *Molecular Ecology*, *10*(2), 407–417. https://doi.org/10.1046/j.1365-294X.2001.01194.x

Stern, K.M. (1970). Der Casiquiare-Kanal, einst und jetzt. *Amazoniana*, *2*(4), 401 – 416.

Sternberg, H.O. (1975). The Amazon River of Brazil. *Geographische Zeitschrift*, 40, 1–74.

Thompson, H. D. (1939). Drainage evolution in the southern Appalachians. *Geological Society of America Bulletin*, *50*(8), 1323-1356. https://doi.org/10.1130/GSAB-50-1323

Turner, T.F., McPhee, M.V., Campbell, P., & Winemiller, K.O. (2004). Phylogeography and intraspecific genetic variation of prochilodontid fishes endemic to rivers of northern South America. *Journal of Fish Biology*, *64*(1), 186-201. https://doi.org/10.1111/j.1095-8649.2004.00299.x

US Army Corps of Engineers. (1943). *Report on Orinoco-Casiquiare-Negro Waterway* (3 vols.). Washington, DC: US Army.

van Denderen, R.P., Schielen, R.M.J., Blom, A., Hulscher, S.J.M.H., & Kleinhans, M.G. (2017). Morphodynamic assessment of side channel systems using a simple one-dimensional bifurcation model and a comparison with aerial images. *Earth Surface Processes and Landforms*. https://doi.org/10.1002/esp.4267

von Humboldt, A. (1877) *Cosmos: A sketch of the physical description of the universe* (E.C. Otté, Trans.). London: Harper & Brothers. (Original work published 1845)

von Humboldt, A., & Bompland, A. (1829). *Personal narrative of travels to the equinoctial regions of the new continent during the years 1799-1804*. (H.M. Williams, Trans.). London: Longman. (Original work published 1814)

Willett, S.D., McCoy, S.W., Perron, J.T., Goren, L., & Chen, C.Y. (2014). Dynamic reorganization of river networks. *Science*, *343*(6175), 1248765. https://doi.org/10.1126/science.1248765

Willis, S.C., Nunes, M., Montana, C.G., Farias, I.P. Orti, G., & Lovejoy, N.R. (2010). Casiquiare river acts as a corridor between the Amazonas and Orinoco river basins: biogeographic analysis of the genus Cichla. *Molecular Ecology*, *19*(5), 1014-1030. https://doi.org/10.1111/j.1365-294X.2010.04540.x

Winemiller, K.O., López- Fernández, H., Taphorn, D.C., Nico, L.G., & Duque, A.B. (2008). Fish assemblages of the Casiquiare River, a corridor and zoogeographical filter for dispersal between the Orinoco and Amazon basins. *Journal of Biogeography*, *35*(9), 1551–1563. https://doi.org/10.1111/j.1365-2699.2008.01917.x

Winemiller, K.O., & Willis, S.C. (2011). The Vaupes Arch and Casiquiare Canal: Barriers and Passages. In J.S. Albert and R.E. Reis (Eds.), *Historical Biogeography of Neotropical Freshwater Fishes* (pp. 225-242). Berkeley, CA: University of California Press.

Yanites, B.J., Ehlers, T.A., Becker, J.K., Schnellmann, M., & Heuberger, S. (2013). High magnitude and rapid incision from river capture: Rhine River, Switzerland. *Journal of Geophysical Research: Earth Surface*, *118*(2), 1060-1084. https://doi.org/10.1002/jgrf.20056

3. Fast response of Amazon rivers to Quaternary climate cycles

Abstract

Large alluvial rivers transport water and sediment across continents and shape lowland landscapes. Repeated glacial cycles have dominated Earth's recent climate, but it is unclear whether these rivers are sensitive to such rapid changes. The Amazon River system, the largest and highest-discharge in the world, features extensive recent terraces that demonstrate geologically rapid change temporally correlated with changes in runoff from Quaternary climate cycles. To test the plausibility of a causal relationship, we use a simple model to estimate from empirical measurements how quickly a river profile responds to changes in discharge or sediment supply. Applying this model to data from 30 gauging stations along alluvial rivers throughout the Brazilian Amazon, we find that many rivers of the Amazon basin can respond faster than changes in runoff or sediment flux on glacial timescales. The Amazon basin is unusually responsive compared to other large river systems due to its high discharge and sediment flux, narrow floodplains, and low slopes. As a result, we predict that the Amazon basin has been highly dynamic during Quaternary glacial cycles, with cyclical aggradation and incision of lowland rivers driving repeated habitat and environmental change throughout the region. This dynamic landscape may contribute to the exceptional biodiversity of the region and patterns of human settlement.

3.1. Introduction

3.1.1. Large alluvial rivers and climate

Large alluvial rivers are the arteries of Earth's major river systems, carrying water and sediment across continents (Ashworth & Lewin, 2012; Potter, 1978). Rivers are the primary agents of landscape change acting on much of Earth's terrestrial surface, and they are themselves

shaped by their climatic and tectonic settings through the effects of hydrology, weathering, rock deformation and vertical motion, and other factors. Although the importance of these factors is widely acknowledged, it is difficult to reconstruct how individual rivers responded to specific climatic or tectonic events in the geologic past due to both insufficient data and incomplete theories. This is one reason why models of landscape evolution commonly assume constant climatic conditions through time.

Although tectonic deformation is typically steady over million-year timescales, Earth has recently experienced large oscillations in climate driven by Milankovitch orbital forcing and amplified by feedbacks in the climate system (Lisiecki & Raymo, 2005; Zachos, Pagani, Sloan, Thomas, & Billups, 2001). Since the Mid-Pleistocene Transition (~1 Ma), these cycles have occurred with a 100 kyr period (Figure 3.1A). In addition to driving glacial advance and retreat at high latitudes and elevations, these climate cycles have caused global changes in temperature and precipitation (Pinot et al., 1999), which have likely altered water discharge and sediment flux in rivers worldwide. The sensitivity of large rivers to these changes is debated. There is some evidence for observable river responses to glacial cycles (Bridgland & Westaway, 2008; Tofelde et al., 2017), but other studies have argued for buffered behavior on these timescales (Allen, 2008; Castelltort & Van Den Driessche, 2003; Métivier, 1999; Métivier & Gaudemer, 1999), in which rivers adjust to the long-term mean climate over multiple glacial cycles and are insensitive to shorter-term fluctuations. The responsivity is likely scale-dependent, with smaller rivers able to respond faster than continent-scale river systems, which typically cannot respond on glacial timescales (Castelltort & Van Den Driessche, 2003). The response of rivers to glacial climate changes – or the lack of a response – governs the nature of sediment delivery to ocean basins, the formation or absence of river terraces on land, and potential feedbacks between

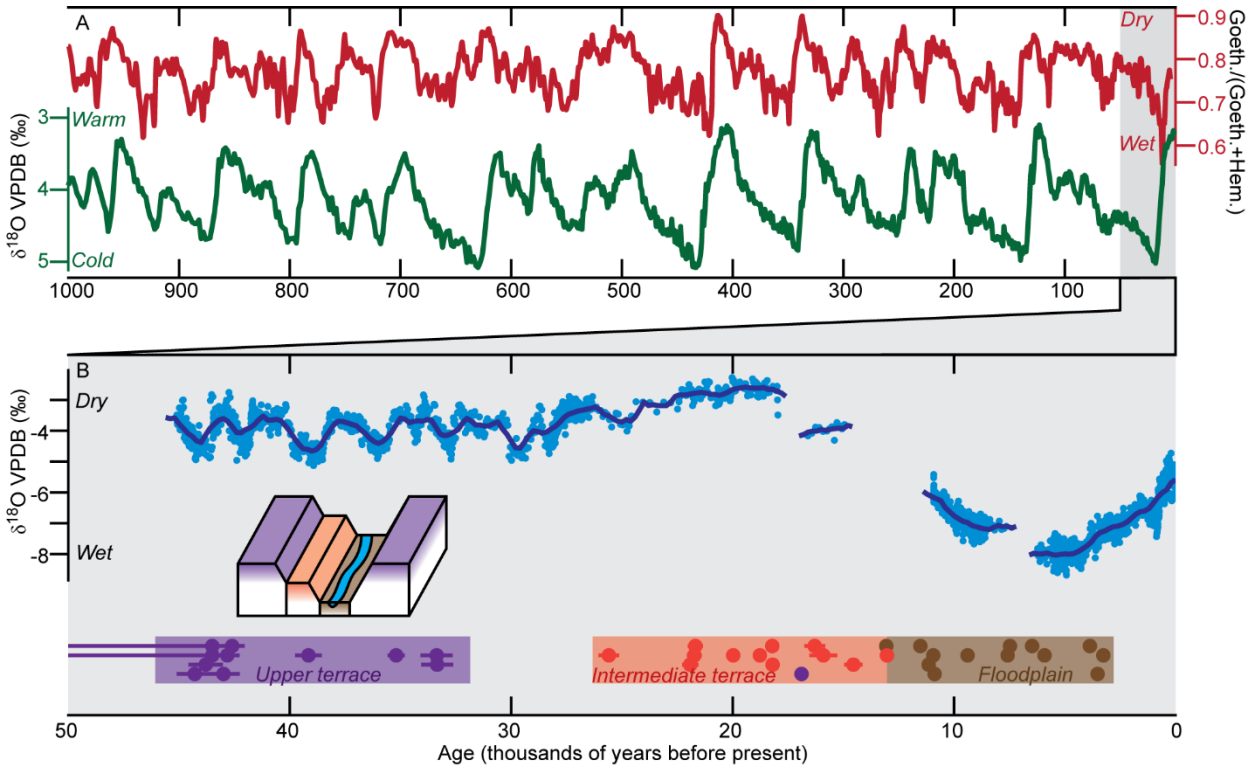

Figure 3.1. **Chronology of Quaternary climate and fluvial deposits in the Amazon**. A: One million year records of global benthic foraminifera oxygen isotopes (green curve, left axis) (Lisiecki & Raymo, 2005), a proxy for ocean temperature and ice volume, and iron oxide mineralogy from the Amazon fan (goethite/[goethite+hematite], red curve, right axis) (Harris & Mix, 1999). The iron oxide ratio reflects varying contributions of cratonic and Andean eroded material, which is thought to be determined by climatic factors. B: Blue points and curve show 50 kyr record of hydrologic change in the eastern Amazon from a speleothem oxygen isotope record (Wang et al., 2017); higher values correspond to drier conditions. Purple, orange, and brown points show ^{14}C ages from different fluvial terrace levels as shown on block diagram; ages and terrace designations from (Rossetti et al., 2014). Terraces ages and schematic diagram are shown for the Madeira river, which is typical of the Andean rivers in the basin.

climate cycles and Earth's surface processes.

A river's sensitivity to climate cycles, and its corresponding ability to reshape itself and the surrounding landscape, depends on whether it can adjust to changes in climatic conditions on relevant timescales. To assess the role of cyclical climate change in shaping alluvial rivers, we use a simple theoretical model to quantify the response time of an alluvial system from physically measurable quantities. We compare this response time to the periodicity of glacial

cycles to explore the predictions and implications of this model for the Amazon basin and elsewhere during Quaternary glacial cycles. This relationship predicts the relative stability or dynamism of terrestrial landscapes subject to cyclical climate forcing.

3.1.2 The Amazon River Basin

The Amazon River is by far the largest in the world by discharge, five times larger than the next, and carries nearly one-fifth of global river discharge (Milliman & Farnsworth, 2011). The Amazon basin includes the tectonically active Andes mountains, the Brazilian and Guyana cratons, and lowland basins (Figure 3.2). Although far from polar ice sheets, it has experienced substantial changes in precipitation during glacial cycles, with more precipitation during interglacial episodes and dry conditions during glacial episodes. This precipitation pattern is attested for during the most recent glacial cycle by speleothem oxygen isotopes (Wang et al., 2017) (Figure 3.1B) and the preservation of relict aeolian dunes (Carneiro Filho, Schwartz, Tatumi, & Rosique, 2002); offshore terrigenous sediments are interpreted to indicate a similar correlation of precipitation and glacial cycles for at least the past million years (Figure 3.1A) (Harris & Mix, 1999). The same precipitation trend is observed across the Amazon basin from west to east (Cheng et al., 2013; Wang et al., 2017). We use this climate history and the diverse array of rivers in the Amazon basin as a natural experiment to explore how a large, continent-scale river system responds to cyclical environmental forcing.

Unusually for a large lowland river system, most of the rivers of the lowland Amazon basin are entrenched by several tens of meters into alluvial deposits composing the surrounding landscape (Figure 3.2), and the high bluffs created by this entrenchment are often the most substantial topographic relief in this generally flat region. This landscape morphology exerts a strong influence on the environmental structure of the region by clearly separating the seasonally

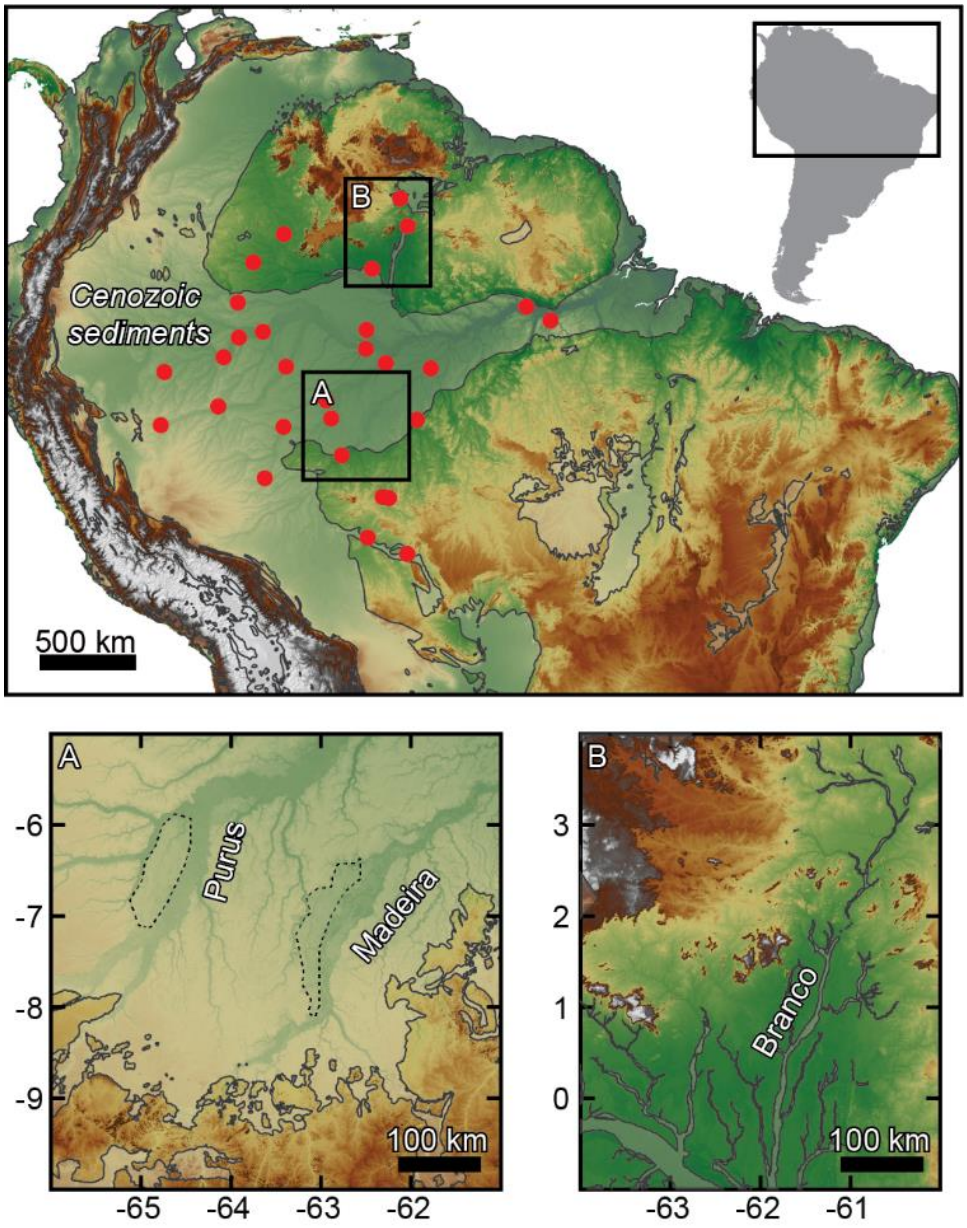

Figure 3.2. **Geologic and topographic context of study region.** Shaded relief topographic map of northern South America from 30″ HydroSHEDS DEM (Lehner, Verdin, & Jarvis, 2008) showing widespread entrenchment of Amazonian rivers into the surrounding landscape. Red circles show locations of sediment flux measurements. Insets A and B show examples of an Andean river (Madeira), a foreland river (Purus), and a cratonic river (Branco), using MERIT DEM elevation data (Yamazaki et al., 2017). Outlined and shaded regions show extent of Cenozoic sediments (Bizzi et al., 2003; Schenk et al., 1999). Dashed lines in A denote intermediate alluvial terraces (Figure 3.1B).

flooded *várzea* and *igapó* forests on the floodplain from the upland *terra firme* habitat despite typical annual river stage variation of 5-10 m (Meade, Rayol, Da Conceicão, & Natividade, 1991). This environmental diversity likely plays a role in the exceptional biodiversity of the region, given the ecological differences between the two habitats (Campbell, Daly, Prance, & Maciel, 1986; Gama, de Souza, Martins, & de Souza, 2005). This structure may also have fostered ancient agriculture; the largest archaeological settlements with highly fertile anthropogenic soils are often located near the edges of bluffs at the interface of these two environments (Denevan, 1996; Kern et al., 2003; McMichael et al., 2014; WinklerPrins & Aldrich, 2010).

Much of the Amazonian lowlands is composed of recent (Neogene and Quaternary) fluvial sediments (Bizzi, Schobbenhaus, Vidotti, & Gonçalves, 2003; Schenk, Viger, & Anderson, 1999) (Figure 3.2). The entrenchment of modern rivers and floodplains into these sediments indicates past aggradation by fluvial systems, creating the terraces and surfaces preserved today above the modern floodplains, followed by incision of rivers into their former deposits. This switch from aggradation to incision profoundly reshaped the environment. When the present upper terrace adjacent to most Andean and foreland rivers (upper surface in Figure 3.2A) was an active depositional surface, the landscape was dominated by an extensive, seasonally flooded wetland. The subsequent incision of rivers and their floodplains caused a restriction of the *várzea* forest to the active floodplain and the emergence of the upland *terra firme* environment on the relict depositional surface as the areally dominant environment (Pupim et al., 2019). Hypothesized causes of this switch from aggradation to incision include neotectonic crustal deformation (Rossetti, 2014), climatic and hydrologic change (Harris & Mix, 1999; Rigsby, Hemric, & Baker, 2009), dynamic topography (Shephard, Müller, Liu, & Gurnis, 2010),

and downstream base level change (Irion et al., 2010). The available sediment burial ages, although sparse, suggest that the upper terrace may in many locations be late Pleistocene in age (Pupim et al., 2019; Rossetti et al., 2014), implying average incision rates since terrace abandonment of up to ~1 mm/yr. Such rates are geologically rapid, particularly for a lowland region. Unraveling the influence of the many factors shaping the rivers of the Amazon region has the potential to reveal the origins and history of this unique landscape.

To assess the role of periodic climate change in shaping alluvial rivers, and evaluate whether Quaternary glacial cycles could have created the high bluffs and deeply entrenched rivers of the Amazon basin, we use a combination of theoretical analysis, empirical measurements, and topographic analysis to characterize the response of the Amazon river system to cyclical climate change on Milankovitch timescales. We examine how different rivers within the basin responded to Pleistocene climate cycles and associated changes in precipitation, river discharge, and sediment flux, and we compare our model to observed river terraces and burial ages. Our examples span multiple tectonic and geologic contexts, including active orogeny, foreland basin, and cratonic basin.

3.2. Materials and Methods

3.2.1. Model of alluvial profile evolution

We model the evolution of an alluvial river's elevation profile with a non-linear advection-diffusion equation, which we derive from a power-law sediment transport expression using an approach similar to that of previous studies (Begin, Meyer, & Schumm, 1981; Métivier & Gaudemer, 1999; Paola, 2000; Paola, Heller, & Angevine, 1992; Whipple & Tucker, 2002). We begin with an equation relating total sediment flux to river slope and water discharge,

$$Q_s = K Q_w^m S^n \quad (1)$$

where Q_s is the volumetric sediment flux averaged over the channel cross-section [L^3/T], K is a transport coefficient [$L^{3(1-m)}T^{1-m}$], Q_w is the water discharge [L^3/T], and S is the channel slope [-]. m and n are exponents, and are both expected to fall between 1 and 2 (Howard, 1994; Whipple & Tucker, 2002). Similarly to the stream-power law for bedrock river incision (Lague, 2014), a transport law of this form is motivated by a shear-stress based formulation for sediment transport such as that of Engelund & Hansen (1967). The transport coefficient K includes information about sediment transport by flowing water, physical sediment properties, river channel geometry, and hydraulic flow resistance. We parameterize the river discharge as a linear function of drainage area (A [L^2]), related by the runoff coefficient r [L/T]:

$$Q_w = rA. \quad (2)$$

We next invoke an Exner-type volume conservation equation in one dimension (downstream channel distance),

$$\frac{\partial z}{\partial t} = -\frac{1}{\varepsilon}\frac{\Omega}{W}\frac{\partial Q_s}{\partial x}, \quad (3)$$

where the vertical coordinate z refers to the elevation of the channel [L] and the horizontal coordinate x is the downstream channel distance [L]. ε is the volumetric solids fraction of the bed material [-], Ω is the sinuosity of the river channel relative to the floodplain valley [-], and W is the floodplain width [L]. This model assumes that the channel and floodplain are tightly coupled on the timescales of interest, such that aggradation and degradation of the channel and floodplain are equal. This assumption is justified in the case of Amazonian rivers by the high rate of sediment exchange between the channel and floodplain (Aalto et al., 2003; Dunne, Mertes, Meade, Richey, & Forsberg, 1998). We are therefore modeling the evolution of the combined

channel-floodplain system. Combining equations 1-3 and replacing the channel slope with the negative downstream derivative of channel elevation gives

$$\frac{\partial z}{\partial t} = -\frac{1}{\varepsilon}\frac{\Omega}{W}\frac{\partial}{\partial x}\left(K(rA)^m\left(-\frac{\partial z}{\partial x}\right)^n\right). \tag{4}$$

For simplicity, we assume that the runoff and transport coefficients *r* and *K* are spatially uniform. Expanding the derivatives in equation 4 then gives

$$\frac{\partial z}{\partial t} = -\frac{1}{\varepsilon}\frac{\Omega}{W}\left(Kmr^m A^{m-1}\frac{\partial A}{\partial x}\left(-\frac{\partial z}{\partial x}\right)^n - Kn(rA)^m\left(-\frac{\partial z}{\partial x}\right)^{n-1}\frac{\partial^2 z}{\partial x^2}\right). \tag{5}$$

Equation 5 is a non-linear advection-diffusion equation. The first term in parentheses is a non-linear advection term representing changes in sediment transport capacity due to downstream changes in drainage area. The second term in parentheses is a non-linear diffusion term representing changes in sediment transport capacity due to downstream changes in slope. In natural systems, these two effects are of comparable magnitude, and for an equilibrium (graded) profile are necessarily equal and opposite. The effective advection celerity *u* and diffusivity *D* are given by

$$u = \frac{1}{\varepsilon}\frac{\Omega}{W}Kmr^m A^{m-1}\frac{\partial A}{\partial x}\left(-\frac{\partial z}{\partial x}\right)^{n-1}, \tag{6}$$

$$D = \frac{1}{\varepsilon}\frac{\Omega}{W}Kn(rA)^m\left(-\frac{\partial z}{\partial x}\right)^{n-1}. \tag{7}$$

We substitute our sediment transport law (equation 1) to yield simplified forms:

$$u = \frac{\Omega m}{\varepsilon}\frac{Q_s}{WS}A^{-1}\frac{\partial A}{\partial x}, \tag{8}$$

$$D = \frac{\Omega n}{\varepsilon}\frac{Q_s}{WS}. \tag{9}$$

The diffusivity given by equation 9 is like that of past studies (Castelltort & Van Den Driessche, 2003; Métivier & Gaudemer, 1999), but with additional terms of sinuosity (to fully account for

the relationship between river length and floodplain area), packing density, and the slope exponent (to account for non-linearity of diffusion).

The parameters *u* and *D* can be used to estimate characteristic response times for the profile evolution of an alluvial river. We assess the relative importance of the diffusive and advective terms by examining the dimensionless Péclet number over an alluvial length scale *L*:

$$\mathrm{Pe} = L\frac{u}{D} = L\frac{m}{n}\,A^{-1}\frac{\partial A}{\partial x}. \tag{10}$$

If we substitute a Hack's Law power-law relationship (Hack, 1957) for drainage area as a function of downstream distance, $A \propto x^h$, the Péclet number becomes

$$\mathrm{Pe} = \frac{L}{x}\frac{mh}{n}, \tag{11}$$

where *h* is the exponent relating drainage area to channel length. We take as our length scale *L* the length of the alluvial portion of the river. Typical values of *m* and *n* range from one to two (Tucker & Bras, 1998; Whipple & Tucker, 2002), with estimated values for the ratio *m*/*n* between two-thirds (Howard, 1994) and one (Tucker & Bras, 1998). The Hack exponent *h* is typically ~1.7-2. At the river mouth, the ratio *L*/*x* will always be less than or equal to one, since the alluvial length can be at most the total length of the river from the drainage divide. Thus, the Péclet number will be close to or less than one. Rivers with $Pe \sim 1$, which occurs when $L \approx x$ and most of the river length is alluvial, have similar advective and diffusive timescales. Rivers with $L < x$ and $Pe < 1$ have a diffusion timescale that is shorter than the advection timescale, and the system is diffusion-dominated. In either case, the diffusion timescale provides an estimate of the system response time. This is useful because the advection celerity (equation 8) is less straightforward to quantify for natural systems due to the spatial derivative of drainage area, which is difficult to approximate for rivers with discrete tributaries. We therefore focus on the

diffusivity and diffusion timescale as quantitative metrics to characterize and compare the response of alluvial rivers, which we evaluate for natural systems.

With the exception of the slope exponent *n*, the diffusivity (equation 9) depends only on physical and empirically measurable quantities: the bed porosity, channel sinuosity, floodplain width, channel slope, and sediment flux. We describe the data and methods used to measure these quantities in Section 2.2. Due to uncertainties in estimating long-term sediment flux from short-term measurements, we do not use the individually measured sediment fluxes to compute the diffusivity. Rather, we regress observed sediment flux against channel slope and water discharge for a number of gauging stations to obtain a transport relationship, which we use to estimate the transport coefficient *K* in equation 7. To calculate the diffusion timescale L^2/D, we use the same length scale as above, the alluvial length of the river. This gives a similar expression to the reaction time of (Métivier & Gaudemer, 1999), with additional terms of sinuosity (to fully account for the relationship between river length and floodplain area), packing density, and the slope exponent (to account for non-linearity of diffusion). We also use the diffusivities to compute a propagation length δ (analogous to the skin depth in thermal diffusion) indicating the distance an environmental signal will propagate along a river channel for a fixed periodicity of forcing, using the relation $\delta = \sqrt{DP/\pi}$, where *P* is the period, which we take to be 10^5 years to simulate recent glacial cycles.

3.2.2. Data sources

We calculated diffusivities for 30 gauging stations along alluvial rivers in the Amazon using Equation 7. From these diffusivities we calculated diffusion timescales and propagation lengths. We estimated the transport coefficient *K* from sediment flux measurements at a network of gauging stations (Filizola & Guyot, 2009) measuring total suspended load (Figure 3.2),

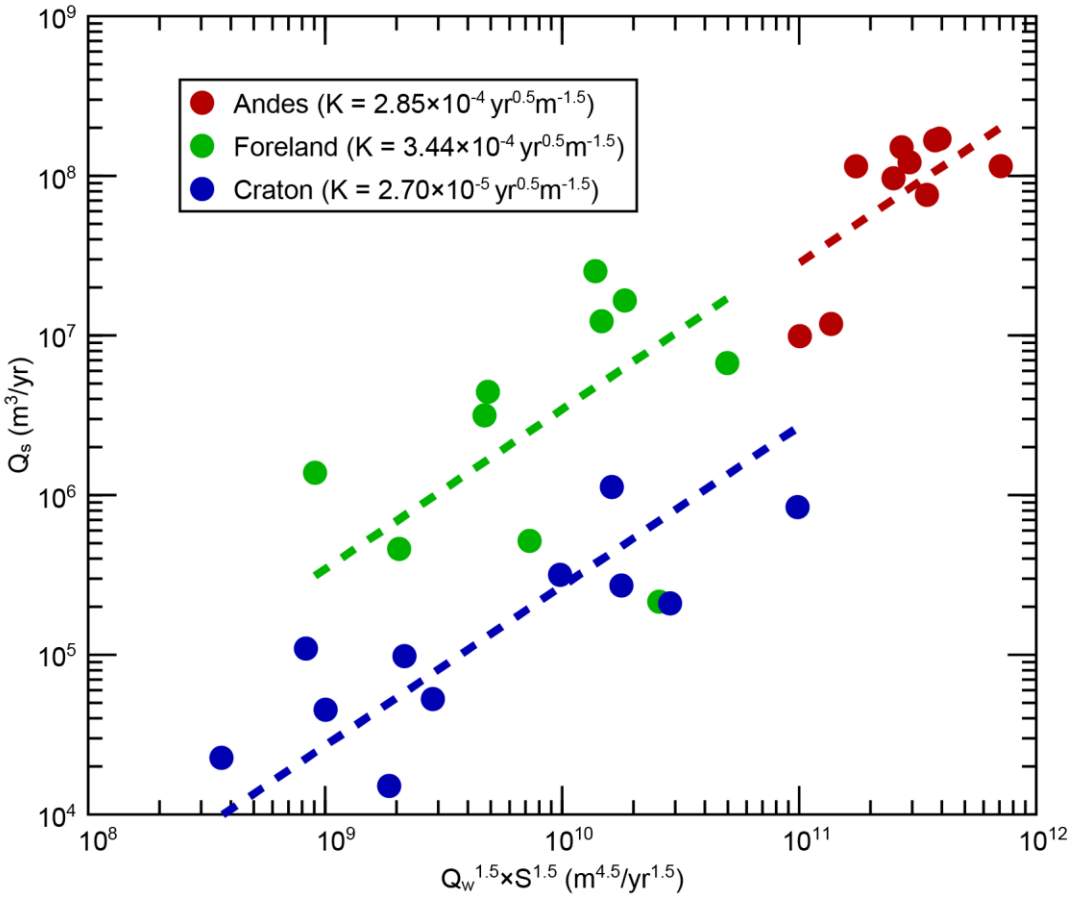

Figure 3.3. Estimating the sediment transport coefficient. Power-law regression of sediment flux against the discharge-slope product raised to the 3/2 power. The intercept gives the transport coefficient *K*. We perform a separate regression for each of the three tectonic settings.

converting mass fluxes to volumetric fluxes assuming a sediment density of 2.65 g/cm^3. While aggradation or incision depend on the total bed material load, including both bedload and suspended load, we expect that most of the sediment in these large, low-gradient rivers is transported as suspended load. We divide these rivers into three tectonic categories: Andes, foreland, and craton. Andes rivers receive sediment directly from the Andes; foreland rivers are those located within the foreland basin but without a direct Andean connection; craton rivers are those draining the Brazilian Shield or Guiana Highlands. We estimated values of *K* independently for each of the three tectonic settings by regressing the sediment flux measurements against the product of the discharge and slope raised to a power of 1.5, in the

middle of the published range (Tucker & Bras, 1998; Whipple & Tucker, 2002) (Figure 3.3), with the exponent fixed to facilitate direct comparison of transport coefficients among tectonic settings. We find that the transport coefficients for Andean and foreland rivers are similar, while that of cratonic rivers is about ten times lower (Figure 3.3). This may reflect differences in sediment grain size, bed-load proportion, or channel and flow properties among these different settings, or it may indicate that cratonic rivers are not fully transport-limited and thus not well represented by our model.

We calculated channel slopes using MERIT Hydro flow routing data and MERIT DEM elevation data, at 3-second (~90 m) resolution (Yamazaki et al., 2019, 2017), by performing a linear regression on the channel profiles in the vicinity of the gauging stations. We manually measured floodplain width and channel sinuosity from the same datasets. While sinuosity may have varied through time due to changes in discharge and sediment flux, most of the rivers we measured have sinuosities between 1.1 and 1.5, which suggests that potential past variations were small relative to other uncertainties. We assume that the width of the modern floodplain is representative of the width of the floodplain as the river was lowering/incising because this width sets the volume of sediment evacuated by the river to create the steep bluffs bounding the modern floodplain. We used 0.65 for the sediment packing fraction (Dunne et al., 1998). For the length scale L, we used the length of the alluvial portion of each river, as determined from topographic and geologic map data. We use the confluence of the tributary with the mainstem as the downstream boundary.

3.2.3. Numerical simulations

Although estimated diffusion timescales provide a useful order-of-magnitude assessment of rivers' responsiveness to climate cycles, they only address one of the terms in our advection-

diffusion model and do not account for temporal variation in D or u from changing environmental conditions. We tested the validity of this scaling analysis and explored the transient response of rivers with numerical solutions. We solved Equation 5 using a centered-space, forward-time finite difference method and a Hack's law approximation for drainage area (Hack, 1957). We calibrated the model parameters to two example Amazon tributaries, the Madeira and Guapore Rivers, representing the Andean and cratonic settings respectively (Table 3.S1). Both of these rivers feature clear alluvial features such as meanders and oxbows within floodplains. We use $m = n = 1.5$ and a Hack exponent $h = 1.8$. We used the transport coefficients for Andean and cratonic rivers (Figure 3.3), respectively, and discharge from the Porto Velho and Pimenteiras gauging stations. For the initial condition, the upstream boundary was assigned discharge, drainage area, and slope from the gauging station, with sediment flux given by the transport coefficient and transport law. For the initial profile we used a graded (equilibrium) profile for the modern value of the runoff, at which the transport capacity in equation 1 is equal to the upstream supply at all points in the model domain. We imposed the upstream sediment supply as a slope boundary condition, and constant base level at the downstream boundary. Although these rivers were likely subject to base-level change from ice age sea-level effects, our theoretical model is generally agnostic to the particular mechanism of perturbation.

We present two sets of simulations of oscillatory climate forcing. In the first, we varied the runoff coefficient with a 100 kyr period, similar to precipitation changes in the Amazon basin during recent glacial cycles (Figure 3.1), while keeping sediment supply constant. We vary the runoff by a factor of two. In the second, we varied the sediment supply under a constant runoff (Figure 3.5D), also by a factor of two. These simulations are not meant to be quantitative reconstructions of the history of the Madeira and Guapore systems, but rather attempts to

understand how rivers with similar characteristics might evolve under a cyclical climate such as Earth has recently experienced. We seek to understand a river's ability to respond on relevant timescales to any environmental change that causes profile disequilibrium.

3.3. Results

3.3.1. River response times and propagation lengths

The estimated diffusivities span four orders of magnitude, from 1.6×10^5 m^2/yr to 8.5×10^8 m^2/yr (Figure 3.4A). The diffusivities show a strong dependence on tectonic setting, with the Andean rivers at the high end of the range (geometric mean 3.8×10^8 m^2/yr), the cratonic rivers at the low end (1.2×10^6 m^2/yr), and the foreland rivers between (1.2×10^7 m^2/yr). This is mainly due to the large variations in discharge and sediment flux, although this effect is partially counteracted by the floodplain width in the denominator of Equation 2, which scales with

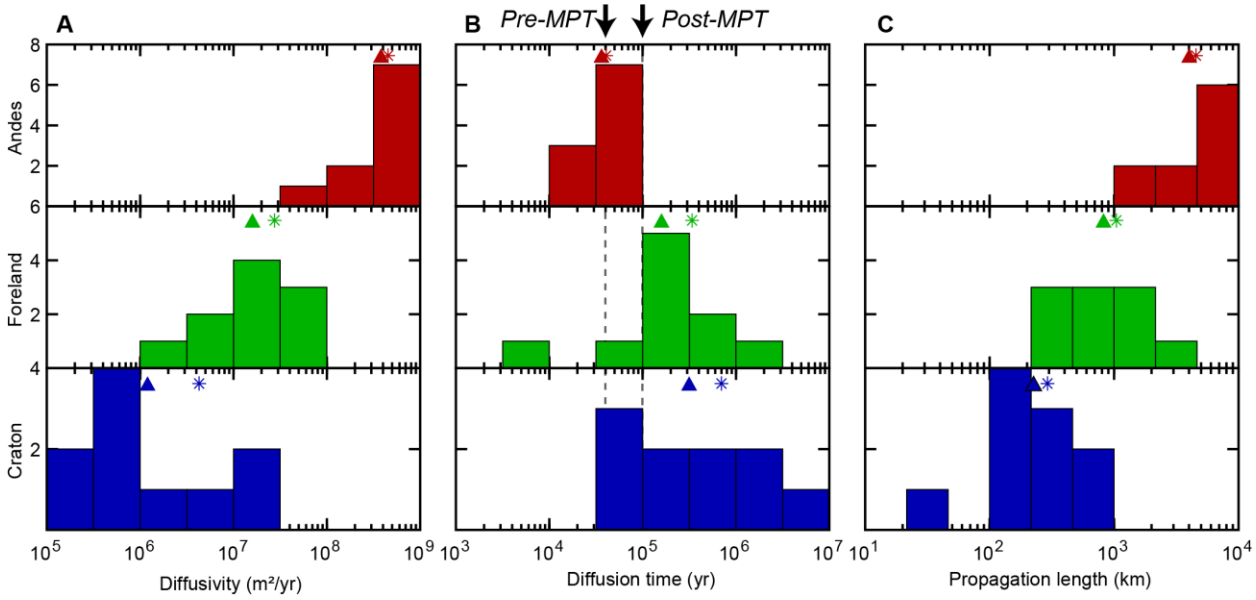

Figure 3.4: **Diffusivities, diffusion timescales and propagation lengths.** Estimated diffusivities (A), diffusion timescales (B), and propagation lengths for a 100 kyr period (C) for rivers in the Amazon, categorized by tectonic setting. Vertical axis shows the number of stations in each bin. Triangles and stars show the geometric and arithmetic means, respectively, of each quantity and tectonic setting. The dashed lines and arrows denote the approximate periods glacial cycles before (40 kyr) and after (100 kyr) the Mid-Pleistocene Transition (MPT).

sediment flux and drainage area. The diffusivity should generally increase downstream with increasing drainage area, discharge, and sediment flux, although the rivers we sample are generally sufficiently large and the gauging stations sufficiently far downstream that our estimates are broadly representative of the lower reaches of the rivers; we do not expect that the diffusivity increases substantially downstream of the gauging stations in our study reaches.

When we convert the diffusivities to diffusive response times (Figure 3.4B), the range is reduced to three orders of magnitude, with the shortest response times belonging to the Andean rivers, with a minimum of 13 kyr and a geometric mean of 36 kyr, and the longest response timescales belonging to the cratonic rivers, with a geometric mean of 340 kyr and a maximum of 9 Myr. Foreland rivers have intermediate response times with a geometric mean of 160 kyr. The reduction in range relative to diffusivities is due to the compensating effect of river length – the Andean rivers with the largest discharge, sediment flux, and diffusivity are also substantially longer than most of the foreland and cratonic rivers. Nevertheless, the short response times of the Andean rivers show that the high discharge and sediment flux outweigh their great length, even in the case of the mainstem Amazon, which has nearly 5000 km of alluvial length. The propagation lengths for a 100 kyr period (Figure 3.4C) have geometric means of 4000, 820, and 230 km for Andean, foreland, and cratonic rivers respectively.

While these are likely order-of-magnitude estimates due to uncertainties in the parameters, the response times for Andean rivers (Figure 3.4B) are all shorter than the 100 kyr period of recent glacial cycles, and most are substantially shorter, by a factor of 2 to 6. Similarly, the propagation lengths for Andean rivers (Figure 3.4C) all exceed 1000 km, indicating that environmental perturbations with a 100,000 year period can elicit a response over continental scales. Comparing the propagation length with the actual alluvial river length is analogous to

comparing the response timescale with the periodicity of forcing: rivers with propagation lengths longer than their alluvial lengths have response timescales shorter than the forcing period, and vice versa.

The response times for cratonic and foreland rivers are more varied and span a wide range on both sides of this glacial timescale. Foreland rivers have response times with geometric and arithmetic means of 160 and 340 kyr and propagation lengths with geometric and arithmetic means of 820 and 1050 km. Cratonic rivers have response times with geometric and arithmetic means of 310 and 700 kyr and propagation lengths with geometric and arithmetic means of 230 and 290 km. As we discuss in more detail in the Section 4, these estimated response times and propagation lengths suggest that the Andean rivers and many foreland rivers have repeatedly aggraded and incised in response to Quaternary glacial cycles.

3.3.2. Numerical results

The simulation results are consistent with our analysis of diffusive response times. The two river systems we used to calibrate the numerical simulations have estimated response times of 14 kyr (Madeira) and 1.3 Myr (Guapore), a difference that reflects their vastly different sediment loads and discharges (Table 3.S1). Correspondingly, in the Madeira simulation, the modeled river profile rapidly adjusts to the changes in runoff or sediment flux and is always near its equilibrium profile throughout the simulation (Figure 3.5B). This is consistent with the Madeira River's estimated response time, which is substantially shorter than the periodicity of the modeled forcing. Analogously, our estimated propagation length of 5000 km is longer than the 3000 km alluvial length of the Madeira River.

The Guapore simulation behaves very differently (Figure 3.5C). Since the response time is much longer than the 100 kyr period of forcing, the river profile is unable to adjust to each

cycle (green curves in Figure 3.5C). The distance of profile adjustment from one cycle is comparable to the ~200 km propagation length we estimate. Instead, over many cycles the river approaches a profile governed by the long-term mean runoff (purple curves in Figure 3.5C), with the individual cycles damped by the long response time. The diverging behavior of these two simulations is a direct consequence of their different response times relative to the periodicity of the imposed climate forcing; the diffusive response time accurately captures the behavior of the advection-diffusion system we model. This dichotomous behavior occurs similarly for a periodic

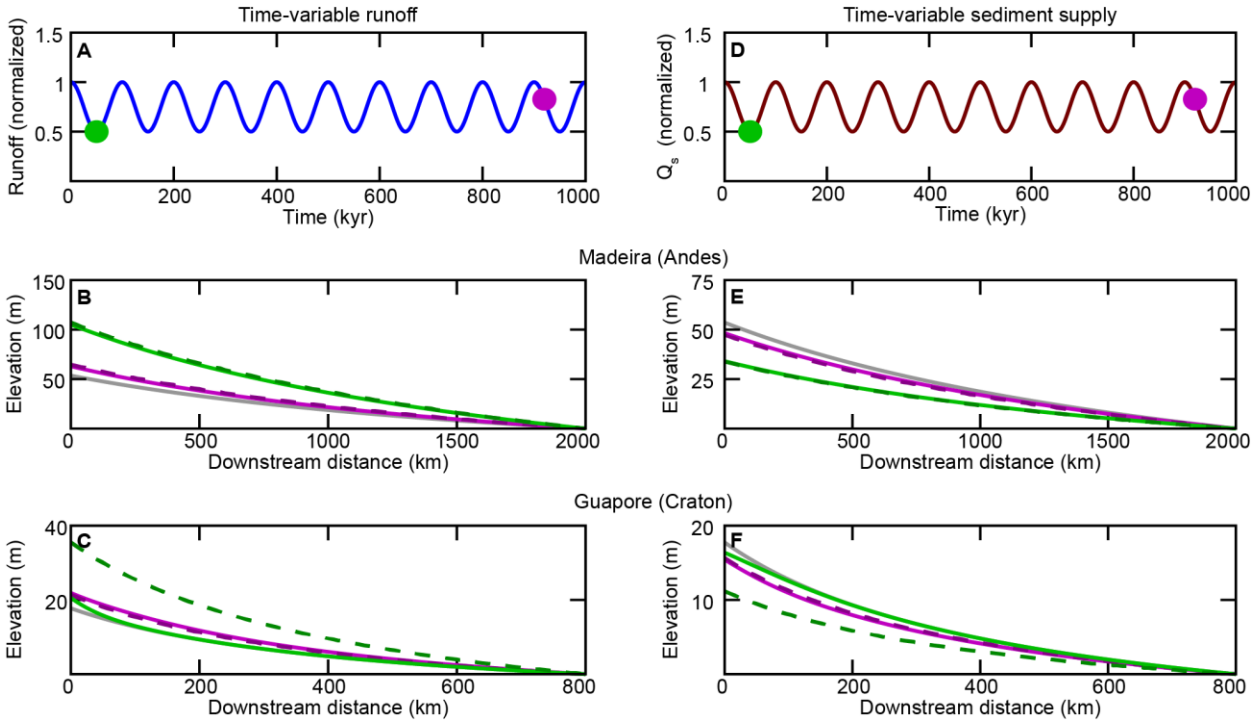

Figure 3.5. **Numerical simulations of river profile evolution**. Numerical simulations of river profile evolution under time-varying runoff with constant sediment supply (A, B, C) and time-varying sediment supply with constant runoff (D, E, F). A: Time history of runoff coefficient *r* for simulations shown in B and C. B, E: Simulations using Madeira River parameters. C, F: Simulations using Guapore River parameters. D: Time history of sediment supply for simulations shown in E and F. For each simulation, three profiles are shown. The gray profile shows the initial condition, and the two colored lines correspond to the times marked by the two colored circles in A. For each colored profile, the solid line shows the actual computed river profile, and the darker dashed line shows the equilibrium graded profile for the instantaneous values of the runoff and sediment flux. Line colors correspond to the markers shown in A and D.

sediment supply with the same period (Figure 3.S1). A similar relationship between channel adjustment and periodicity of climatic forcing has been shown for bedrock rivers within a numerical landscape evolution model, where the response time depends instead on the erodibility (Godard, Tucker, Fisher, & Burbank, 2013).

3.4. Discussion

3.4.1. Response of Amazonian rivers to cyclical climate change

The high diffusivities, short response times, and long propagation lengths for the Andean rivers of the Amazon basin are the result of their high discharge and sediment flux. These characteristics enhance Andean rivers' ability to respond to environmental change by aggradation and incision, which depend on a river's capacity to deposit or erode alluvial sediment. Planform changes in alluvial rivers also depend on the entrainment and deposition of sediment; the river response times estimated here may also be useful for understanding changes in meandering in response to climate change, and the meander migration rate of Amazonian rivers similarly has been found to vary as a positive function of sediment flux (Constantine, Dunne, Ahmed, Legleiter, & Lazarus, 2014). Our estimated response times of Andean-draining rivers are consistent with a floodplain recycling time of a few thousand years estimated from sediment measurements along the Amazon mainstem (Mertes, Dunne, & Martinelli, 1996), which further supports the applicability of our advection-diffusion model for these rivers, and likely for the similar foreland rivers as well.

While we model the effect of changes in precipitation and runoff separately, they likely are both changing simultaneously in response to climate cycles and associated changes in vegetation, and may not be in phase (Perron, 2017). The response of river systems to climate

cycles depends on the net effect of changes in discharge and sediment supply on the imbalance between sediment supply and transport capacity. However, as long as these changes are governed by the same global climate cycles and exhibit a similar periodicity, a river profile's ability to adjust to any combination of external changes in discharge and sediment supply depends on the timescale of those changes relative to the river's own response timescale. In the Amazon region, the correlation between dry conditions and terrace deposition ages (Pupim et al., 2019; Wang et al., 2017) (Figure 3.1) demonstrates that the net effect of climate-induced changes in runoff and sediment supply in this region was a reduction in transport capacity relative to supply during dry periods, causing aggradation, and excess transport capacity during wet periods, causing incision and terrace abandonment. This suggests that changes in runoff were the dominant control on fluvial terrace evolution in the region. We also note that, although the diffusivity and thus response timescale will vary with changes in runoff and sediment supply due to non-linearities in equation 5 and in the underlying physical processes, these changes are likely modest. A two-fold change in runoff, all other parameters constant, will change the diffusivity and diffusion time by a factor of $2^{m/n}$; the exponent ratio is close to one. A two-fold change in sediment supply, all other parameters constant, will change the diffusivity and diffusion time by a factor of $2^{1-1/n}$; the exponent is less than one. As a result, the relationship between a river's response time and Quaternary climate periodicity is unlikely to be substantially altered.

While a river with a fast response time will adjust its profile in response to changes in runoff or sediment supply, changes to these two forcings have opposite effects on sediment output for a river system that evolves according to the advection-diffusion model. In the case of runoff variations with constant sediment input, a river with a slow response time will have a variable sediment output whereas river with fast response time will maintain a constant output

equal to the input. Conversely, in the case of sediment input variations with constant runoff, a river with a slow response time will maintain a constant output whereas an river with a fast response time will have variable output corresponding to the variable input. This is because a river's ability or inability to adjust its longitudinal profile and slope governs sediment transport capacity under constant discharge. Comparison of the onshore terrace record with high-resolution offshore sediment accumulation data could thus discriminate between changes in runoff and sediment supply as drivers of geomorphic change.

3.4.2. Quaternary landscape evolution of the Amazon basin

We extend our analysis of river response times (Figure 3.4) to infer the recent landscape history of the Amazon region, since speleothem records indicate broadly consistent trends of wetting and drying across the basin (Cheng et al., 2013; Wang et al., 2017). The sediment-rich Andean-sourced rivers of the western and central Amazon have the capacity to quickly respond to changes in climate, and as a result have probably repeatedly aggraded during dry glacial periods and incised into these deposits during wet interglacials. This inference is supported by the short response time (~30-60 kyr) of the mainstem Amazon, despite its extraordinary alluvial length (4900 km), and by similarly short response times for other Andean tributaries. The deposits that today make up the *terra firme* regions are likely a palimpsest of past glacial episodes, formed and reworked during many successive aggradational phases. This may explain some of the anomalously old ages measured from OSL dating of upper terrace deposits in close proximity to terraces with young MIS 2-3 ages (Cremon et al., 2015): the older terraces could have formed during previous aggradational episodes without subsequent disturbance.

The similar pattern of terraces in many foreland rivers that do not directly receive Andean sediment (Figure 3.2) suggests that many of these rivers behave similarly to a degree. Although

their diffusivities are lower due to smaller discharges and drainage area, this is partially compensated by their shorter lengths than Andean rivers. As a result, they mostly have response times between 100 and 200 kyr. We note that a response time comparable to or even slightly longer than the periodicity of forcing will still permit a detectable response to cyclical change, even if the system does not have sufficient time to fully reach a new equilibrium with each wetting or drying. This is demonstrated by the propagation lengths of many hundreds of kilometers for foreland rivers for a 100 kyr periodic forcing, indicating that an observable response will be felt through much of the river system. In numerical experiments not shown in Figure 3.5, we observed that a river adjusts approximately halfway to a new equilibrium profile at a time of one-half the response time following a step change in discharge, gradually decaying exponentially towards its new equilibrium as time goes on. These widespread terraces thus set the stage for human settlement of the Amazon. Precolonial settlements, as well as many modern settlements, are typically located along the bluff edges created by these terraces – on upland *terra firme*, but adjacent to rivers and floodplains (Denevan, 1996).

The cyclical aggradation and incision of Andes-draining and foreland rivers has created a highly dynamic physical environment, with seasonally flooded wetlands counterintuitively dominating the region during dry glacial phases due to aggradation, and the present condition of extensive *terra firme* uplands following incision and localization of the floodplain during wetter interglacials. The low-sediment flux cratonic rivers of the eastern Amazon may have evolved more slowly, buffered from climate changes on glacial timescales. This may explain why many cratonic rivers in the region do not feature major terraces, indicating that they have likely not experienced significant aggradation and incision during Quaternary climatic oscillations. However, the distribution of diffusion times for cratonic and foreland rivers overlap, yet most

foreland rivers feature major terraces while many cratonic rivers do not. The systematically lower sediment transport of cratonic rivers (Figure 3.3) may indicate that these rivers are not fully transport-limited, even though we selected gauging stations that appeared qualitatively alluvial from topographic data and satellite imagery. If this is the case, then the transport-limited model we use in the study may not be a good description of their behavior, which likely implies a slower fluvial response to environmental change than predicted by this model.

3.4.3. Amazon in a global context

Contrary to our findings, a past study (Métivier & Gaudemer, 1999) found evidence for buffered behavior on glacial timescales for the large Himalayan rivers of the Indo-Gangetic Plain, using a similar model, and a global analysis (Castelltort & Van Den Driessche, 2003) argued that large river systems are typically buffered on these timescales. Several important differences explain the high reactivity of Amazonian rivers relative to the Himalayan rivers and many other large rivers worldwide. Rivers of the Amazon carry comparable sediment loads to those of the Himalaya, yet have floodplains an order of magnitude narrower and slopes an order of magnitude shallower than the braided Himalayan rivers. Both of these factors increase the effective diffusivity and decrease the response time of the Amazon rivers, making them unusually responsive for a river system of their magnitude. The single-threaded rivers of the Amazon thus have a set of characteristics – low gradient, narrow floodplains, high discharge and sediment loads – that predisposes them to adjust rapidly to environmental changes and fosters the dynamic landscape of the western and central Amazon. These differences are at least partly due to the exceptional discharge of the Amazon, owing to its location in the humid tropics and its high rainfall and runoff throughout the basin. The large discharge in turn allows the river to carry its sediment load at very low slopes ($\sim 10^{-5}$). We note that although Castelltort & Van Den

Driessche (2003) used a similar mathematical framework to estimate response times for a set of global rivers, their analysis differed substantially from ours by using the channel width instead of the floodplain width to estimate the diffusivity. This implicitly assumes that the buffering ability comes only from the channel itself, without aggradation or degradation of the adjacent floodplain, and thus tends to substantially underestimate the response times of rivers with active floodplains.

3.4.4. Implications for Amazonian biodiversity

The Amazon region is one of the largest and most species-rich biodiversity hotspots on Earth (Hoorn et al., 2010), and a conspicuous global exception to the correlation of high biodiversity with high-relief mountain ranges (Antonelli et al., 2018). One proposed explanation for the exceptional terrestrial biodiversity of the Amazon is the repeated expansion and contraction of the rainforest habitat due to ecological response to climate changes, with isolation in forest-fragment refugia during glacial episodes driving speciation and diversification (Haffer, 1969). We speculate that the physical changes to the landscape caused by fluvial aggradation and incision and the shifting distribution of *várzea* and *terra firme* habitats may have played a similar role. During dry aggradational episodes, seasonally flooded wetlands were dominant and upland regions restricted. Conversely, during wet incisional episodes, upland regions became extensive. The onset of Pleistocene glaciation and the intensification of glacial cycles at the Mid-Pleistocene Transition may have thus been drivers of speciation in the region through repeated habitat gain and loss. Our analysis suggests that the shift from 40 to 100 kyr periodicity would have caused a larger portion of the Amazon basin to begin to respond to these climatic changes. Moreover, the amplitude of glaciations increased with this transition, which likely increased the variability of tropical rainfall as well. Indeed, phylogenetic evidence indicates that these climate

transitions correspond to elevated origination rates for both vertebrate and invertebrate lineages in the Amazon basin (Garzón-Orduña, Benetti-Longhini, & Brower, 2014; Ribas, Aleixo, Nogueira, Miyaki, & Cracraft, 2012).

3.5. Conclusions

To investigate whether the large alluvial rivers of the Amazon basin have responded to Quaternary glacial cycles, we estimated diffusive response timescales for a range of Amazon tributaries using a simple theoretical model and empirical measurements. The timescales we calculate, which we support with numerical simulations, imply that Andean and foreland rivers have repeatedly aggraded and incised in response to Quaternary glacial cycles, which agrees with the observed wide range of terrace ages in the Amazon lowlands, including many recent dates (25-50 ka). The dynamic behavior of such a large river system, which differs from many other large rivers worldwide, stems from the tectonic and climatic setting of the basin, which give it abundant sediment and water discharge and very low slopes, as well as the narrow floodplains of Amazon rivers, which give it the power to respond rapidly to environmental change on glacial timescales and create a highly dynamic landscape under a cyclical climate.

Acknowledgments

We thank David McGee for helpful discussions of South American paleoclimate and Sara Harris for providing the data for Figure 3.1A. We thank Jean Braun and Eric Kirby for helpful suggestions on an earlier version of the manuscript. This paper is based upon work supported by the National Aeronautics and Space Administration Earth and Space Science Fellowship under Grant No. 80NSSC18K1324. We also acknowledge support from the Abdul Latif Jameel Water

and Food Systems Lab at the Massachusetts Institute of Technology. The authors declare no conflict of interest.

References

Aalto, R., Maurice-Bourgoin, L., Dunne, T., Montgomery, D. R., Nittrouer, C. A., & Guyot, J. L. (2003). Episodic sediment accumulation on Amazonian flood plains influenced by El Niño/Southern Oscillation. *Nature*, *425*(6957), 493–497. https://doi.org/10.1038/nature02002

Allen, P. A. (2008). Time scales of tectonic landscapes and their sediment routing systems. In K. Gallagher, S. J. Jones, & J. Wainwright (Eds.), *Landscape Evolution: Denudation, Climate and Tectonics Over Different Time and Space Scales.* (Vol. 296, pp. 7–28). London: Geological Society. https://doi.org/10.1144/SP296.2

Antonelli, A., Kissling, W. D., Flantua, S. G. A., Bermúdez, M. A., Mulch, A., Muellner-Riehl, A. N., … Hoorn, C. (2018). Geological and climatic influences on mountain biodiversity. *Nature Geoscience*, *11*(10), 718–725. https://doi.org/10.1038/s41561-018-0236-z

Ashworth, P. J., & Lewin, J. (2012). How do big rivers come to be different? *Earth-Science Reviews*, *114*, 84–107. https://doi.org/doi:10.1016/j.earscirev.2012.05.003

Begin, Z. B., Meyer, D. F., & Schumm, S. A. (1981). Development of longitudinal profiles of alluvial channels in response to base-level lowering. *Earth Surface Processes and Landforms*, *6*(1), 49–68. https://doi.org/10.1002/esp.3290060106

Bizzi, L. A., Schobbenhaus, C., Vidotti, R. M., & Gonçalves, J. H. (2003). *Geologia, Tectônica e Recursos Minerais do Brasil: texto, mapas e SIG*. Brasilia: CPRM-Serviço Geológico do Brasil.

Bridgland, D., & Westaway, R. (2008). Climatically controlled river terrace staircases: A worldwide Quaternary phenomenon. *Geomorphology*, *98*(3–4), 285–315. https://doi.org/10.1016/j.geomorph.2006.12.032

Campbell, D. G., Daly, D. C., Prance, G. T., & Maciel, U. N. (1986). Quantitative ecological inventory of terra firme and várzea tropical forest on the Rio Xingu, Brazilian Amazon. *Brittonia*, *38*(4), 369–393.

Carneiro Filho, A., Schwartz, D., Tatumi, S. H., & Rosique, T. (2002). Amazonian paleodunes provide evidence for drier climate phases during the Late Pleistocence-Holocene. *Quaternary Research*, *58*(2), 205–209. https://doi.org/10.1006/qres.2002.2345

Castelltort, S., & Van Den Driessche, J. (2003). How plausible are high-frequency sediment supply-driven cycles in the stratigraphic record? *Sedimentary Geology*, *157*, 3–13. https://doi.org/10.1016/S0037-0738(03)00066-6

Cheng, H., Sinha, A., Cruz, F. W., Wang, X., Edwards, R. L., d'Horta, F. M., … Auler, A. S. (2013). Climate change patterns in Amazonia and biodiversity. *Nature Communications*, *4*, 1411.

Constantine, J. A., Dunne, T., Ahmed, J., Legleiter, C., & Lazarus, E. D. (2014). Sediment supply as a driver of river meandering and floodplain evolution in the Amazon Basin. *Nature Geoscience*, *7*(November), 899–904. https://doi.org/10.1038/NGEO2282

Cremon, É. H., Rossetti, D. D. F., Yee, M., Tatumi, S. H., Bertani, T. C., Cohen, M. C. L., … Munita, C. J. A. S. (2015). Mid-Late Pleistocene OSL chronology in western Amazonia and implications for the transcontinental Amazon pathway. *Sedimentary Geology*, *330*, 1–15. https://doi.org/10.1016/j.sedgeo.2015.10.001

Denevan, W. M. (1996). A bluff model of riverine settlement in prehistoric Amazonia. *Annals of*

the Association of American Geographers, *86*(4), 654–681. https://doi.org/j.1467-8306.1996.tb01771.x

Dunne, T., Mertes, L. A. K., Meade, R. H., Richey, J. E., & Forsberg, B. R. (1998). Exchanges of sediment between the flood plain and channel of the Amazon River in Brazil. *Geological Society of America Bulletin*, *110*(4), 450–467. https://doi.org/10.1130/0016-7606(1998)110<0450:EOSBTF>2.3.CO;2

Engelund, F., & Hansen, E. (1967). A monograph on sediment transport in alluvial streams. *Monografia*, 65. https://doi.org/10.1007/s13398-014-0173-7.2

Filizola, N., & Guyot, J. L. (2009). Suspended sediment yields in the Amazon basin: an assessment using the Brazilian national data set. *Hydrological Processes*, *23*, 3207–3215. https://doi.org/10.1002/hyp.7394

Gama, J. R. V., de Souza, A. L., Martins, S. V., & de Souza, D. R. (2005). Comparação entre florestas de várzea e de terra firme do Estado do Pará. *Revista Árvore*, *29*(4), 607–616.

Garzón-Orduña, I. J., Benetti-Longhini, J. E., & Brower, A. V. Z. (2014). Timing the diversification of the Amazonian biota: butterfly divergences are consistent with Pleistocene refugia. *Journal of Biogeography*, *41*(9), 1631–1638.

Godard, V., Tucker, G. E., Fisher, G. B., & Burbank, D. W. (2013). Frequency-dependent landscape response to climatic forcing. *Geophysical Research Letters*, *40*, 859–863. https://doi.org/10.1002/grl.50253

Hack, J. T. (1957). Studies of longitudinal stream profiles in Virginia and Maryland. *USGS Professional Paper*, *249*(B), 97.

Haffer, J. (1969). Speciation in Amazonian forest birds. *Science*, *165*(3889), 131–137.

Harris, S. E., & Mix, A. C. (1999). Pleistocene precipitation balance in the Amazon Basin

recorded in deep sea sediments. *Quaternary Research*, *51*(1), 14–26. https://doi.org/10.1006/qres.1998.2008

Hoorn, C., Wesselingh, F. P., ter Steege, H., Bermúdez, M. A., Mora, A., Sevink, J., … Antonelli, A. (2010). Amazonia through time: Andean uplift, climate change, landscape evolution, and biodiversity. *Science*, *330*(6006), 927–931. https://doi.org/10.1126/science.1194585

Howard, A. D. (1994). A detachment limited model of drainage basin evolution. *Water Resources Research*, *30*(7), 2261–2285. https://doi.org/10.1029/94WR00757

Irion, G., de Mello, J. A. S. N., Morais, J., Piedade, M. T. F., Junk, W. J., & Garming, L. (2010). Development of the Amazon Valley During the Middle to Late Quaternary: Sedimentological and Climatological Observations. In W. J. Junk, M. T. F. Piedade, F. Wittmann, J. Schongart, & P. Parolin (Eds.), *Amazonian Floodplain Forests: Ecophysiology, Biodiversity and Sustainable Management* (pp. 27–42). Dordrecht: Springer. https://doi.org/10.1007/978-90-481-8725-6

Kern, D. C., D'Aquino, G., Rodrigues, T. E., Lima Frazao, F. J., Sombroek, W., Meyers, T. P., … Neves, E. G. (2003). Distribution of Amazonian Dark Earths in the Brazilian Amazon. In J. Lehmann, D. C. Kern, B. Glaser, & W. I. Woods (Eds.), *Amazonian Dark Earths: Origin, Properties, Management* (pp. 51–75). Dordrecht: Kluwer Academic Publishers. https://doi.org/DOI: 10.1007/1-4020-2597-1_4

Lague, D. (2014). The stream power river incision model: Evidence, theory and beyond. *Earth Surface Processes and Landforms*, *39*(1), 38–61. https://doi.org/10.1002/esp.3462

Lehner, B., Verdin, K., & Jarvis, K. (2008). New global hydrography derived from spaceborne elevation data. *Eos, Transactions, AGU*, *89*(10), 93–94.

Lisiecki, L. E., & Raymo, M. E. (2005). A Pliocene-Pleistocene stack of 57 globally distributed benthic δ18O records. *Paleoceanography*, *20*(1), 1–17. https://doi.org/10.1029/2004PA001071

McMichael, C. H., Palace, M. W., Bush, M. B., Braswell, B. H., Hagen, S., Neves, E. G., … Czarnecki, C. (2014). Predicting pre-Columbian anthropogenic soils in Amazonia. *Proceedings of the Royal Society B: Biological Sciences*, *281*(1777), 23–28. https://doi.org/10.1098/rspb.2013.2475

Meade, R. H., Rayol, J. M., Da Conceicão, S. C., & Natividade, J. R. G. (1991). Backwater Effects in the Amazon River Basin of Brazil. *Environmental Geology and Water Sciences*, *18*(2), 105–114.

Mertes, L. A. K., Dunne, T., & Martinelli, L. A. (1996). Channel-floodplain geomorphology along the Solimões-Amazon River, Brazil. *Geological Society of America Bulletin*, *108*(9), 1089–1107. https://doi.org/10.1130/0016-7606(1996)108<1089:CFGATS>2.3.CO;2

Métivier, F. (1999). Diffusivelike buffering and saturation of large rivers. *Physical Review E*, *60*(5), 5827–5832. https://doi.org/10.1103/PhysRevE.60.5827

Métivier, F., & Gaudemer, Y. (1999). Stability of output fluxes of large rivers in south and east Asia during the last 2 million years: Implications on floodplain processes. *Basin Research*, *11*(4), 293–303. https://doi.org/10.1046/j.1365-2117.1999.00101.x

Milliman, J. D., & Farnsworth, K. L. (2011). *River Discharge to the Coastal Ocean: A Global Synthesis*. Cambridge: Cambridge University Press. https://doi.org/10.1017/CBO9780511781247

Paola, C. (2000). Quantitative models of sedimentary basin filling. *Sedimentology*, *47*(SUPPL. 1), 121–178. https://doi.org/10.1046/j.1365-3091.2000.00006.x

Paola, C., Heller, P. L., & Angevine, C. L. (1992). The large-scale dynamics of grain-size variation in alluvial basins, 1: Theory. *Basin Research*, *4*(2), 73–90. https://doi.org/10.1111/j.1365-2117.1992.tb00145.x

Perron, J. T. (2017). Climate and the Pace of Erosional Landscape Evolution. *Annual Review of Earth and Planetary Sciences*, *45*(1), 561–591. https://doi.org/10.1146/annurev-earth-060614-105405

Pinot, S., Ramstein, G., Harrison, S. P., Prentice, I. C., Guiot, J., Stute, M., & Joussaume, S. (1999). Tropical paleoclimates at the Last Glacial Maximum: comparison of Paleoclimate Modeling Intercomparison Project (PMIP) simulations and paleodata. *Climate Dynamics*, *15*(11), 857–874.

Potter, P. E. (1978). Significance and Origin of Big Rivers. *The Journal of Geology*, *86*(15).

Pupim, F. N., Sawakuchi, A. de O., Almeida, R. P., Ribas, C. C., Kern, A. K., Hartmann, G. A., … Cracraft, J. (2019). Chronology of Terra Firme formation in Amazonian lowlands reveals a dynamic Quaternary landscape. *Quaternary Science Reviews*, *210*, 154–163. https://doi.org/10.1016/j.quascirev.2019.03.008

Ribas, C. C., Aleixo, A., Nogueira, A. C. R., Miyaki, C. Y., & Cracraft, J. (2012). A palaeobiogeographic model for biotic diversification within Amazonia over the past three million years. *Proceedings of the Royal Society B: Biological Sciences*, *279*(1729), 681–689.

Rigsby, C. A., Hemric, E. M., & Baker, P. A. (2009). Late Quaternary Paleohydrology of the Madre de Dios River, southwestern Amazon Basin, Peru. *Geomorphology*, *113*(3–4), 158–172. https://doi.org/10.1016/j.geomorph.2008.11.017

Rossetti, D. D. F. (2014). The role of tectonics in the late Quaternary evolution of Brazil's

Amazonian landscape. *Earth-Science Reviews*, *139*, 362–389. https://doi.org/10.1016/j.earscirev.2014.08.009

Rossetti, D. D. F., Cohen, M. C. L., Bertani, T. C., Hayakawa, E. H., Paz, J. D. S., Castro, D. F., & Friaes, Y. (2014). Late Quaternary fluvial terrace evolution in the main southern Amazonian tributary. *Catena*, *116*, 19–37. https://doi.org/10.1016/j.catena.2013.11.021

Schenk, C. J., Viger, R. J., & Anderson, C. P. (1999). *Maps showing geology, oil and gas fields and geologic provinces of the South America region: U.S. Geological Survey Open-File Report 97-470-D*. U.S. Geological Survey, Central Energy Resources Team.

Shephard, G. E., Müller, R. D., Liu, L., & Gurnis, M. (2010). Miocene drainage reversal of the Amazon River driven by plate–mantle interaction. *Nature Geoscience*, *3*(12), 870–875. https://doi.org/10.1038/ngeo1017

Tofelde, S., Schildgen, T. F., Savi, S., Pingel, H., Wickert, A. D., Bookhagen, B., … Strecker, M. R. (2017). 100 kyr fluvial cut-and-fill terrace cycles since the Middle Pleistocene in the southern Central Andes , NW Argentina. *Earth and Planetary Science Letters*, *473*, 141–153. https://doi.org/10.1016/j.epsl.2017.06.001

Tucker, G. E., & Bras, R. L. (1998). Hillslope processes, drainage density, and landscape morphology. *Water Resources Research*, *34*(10), 2751–2764.

Wang, X., Edwards, R. L., Auler, A. S., Cheng, H., Kong, X., Wang, Y., … Chiang, H. W. (2017). Hydroclimate changes across the Amazon lowlands over the past 45,000 years. *Nature*, *541*(7636), 204–207. https://doi.org/10.1038/nature20787

Whipple, K. X., & Tucker, G. E. (2002). Implications of sediment-flux-dependent river incision models for landscape evolution. *Journal of Geophysical Research*, *107*(B2), 1–20. https://doi.org/10.1029/2000jb000044

WinklerPrins, A. M. G. A., & Aldrich, S. P. (2010). Locating Amazonian dark earths: creating an interactive GIS of known locations. *Journal of Latin American Geography*, *9*(3), 33–50. https://doi.org/10.1353/lag.2010.0029

Yamazaki, D., Ikeshima, D., Sosa, J., Bates, P. D., Allen, G. H., & Pavelsky, T. M. (2019). MERIT Hydro: A High-Resolution Global Hydrography Map Based on Latest Topography Dataset. *Water Resources Research*, *55*(6), 5053–5073. https://doi.org/10.1029/2019WR024873

Yamazaki, D., Ikeshima, D., Tawatari, R., Yamaguchi, T., O'Loughlin, F., Neal, J. C., … Bates, P. D. (2017). A high-accuracy map of global terrain elevations. *Geophysical Research Letters*, *44*(11), 5844–5853. https://doi.org/10.1002/2017GL072874

Zachos, J., Pagani, M., Sloan, L., Thomas, E., & Billups, K. (2001). Trends, Global Rhythms, Aberrations in Global Climate 65 Ma to Present. *Science*, *292*(5517), 686–693. https://doi.org/10.1126/science.1059412

Supplementary Table 3.S1: Database of Amazon tributaries

Station	River	Drainage area (10^3 km^2)	Qw (m^3/s)	Qs (10^6 m^3/yr)	Slope (-) (×10^{-5})	Floodplain width (km)	Sinuosity (-)	Alluvial length (km)	Diffusivity (10^6 m^2/yr)	Diffusion time (10^3 yr)	Propagation length (km)	Setting
Palmeiras do Javari	Javari	12	640	0.46	8	5	1.7	1000	6.92	144.4	438	Foreland
Teresina	Solimoes	980	44000	151	3	15	1.2	4900	473.70	50.7	6279	Andes
Sao Paulo de Olivenca	Solimoes	990	47000	122	3	20	1.2	4900	383.86	62.5	4880	Andes
Santo Antonio do Ica	Solimoes	1100	55000	167	3	30	1.2	4900	328.22	73.2	4668	Andes
Cruzeiro do Sul	Jurua	39	910	4.44	10	12	1.5	2600	4.83	1400.7	737	Foreland
Eirunepe—Montante	Jurua	77	1800	3.16	5	15	2.2	2600	10.95	617.1	953	Foreland
Gaviao	Jurua	160	4800	12.3	4	20	2	2600	29.12	232.1	1734	Foreland
Vila Bittencourt	Japura	197	13720	9.91	5	8	1.2	2000	198.30	20.2	1706	Andes
Itapeua	Solimoes	1800	84000	115	3	20	1.1	4900	853.37	28.1	4543	Andes
Rio Branco	Acre	23	330	1.38	9	6	1.3	570	1.73	187.5	571	Foreland
Seringal Fortaleza	Purus	150	3700	25.3	5	20	2.1	3000	23.03	390.9	2281	Foreland
Labrea	Purus	220	5500	16.6	4	20	2.1	3000	38.30	235.0	2064	Foreland
Bacaba	Cuniua	38	1490	0.52	8	9	1.5	700	12.06	40.6	325	Craton
Aruma—Jusante	Purus	360	11000	6.72	4	25	1.7	3000	67.13	134.1	1058	Foreland
Manacapuru	Solimoes	2100	99000	115	1	30	1.1	4900	418.59	57.4	6419	Andes
Cucui	Negro	62	4840	0.32	3	2	1.1	1900	12.72	283.8	754	Craton
Taraqua	Uaupes	45	2760	0.22	10	3	1.2	560	81.57	3.8	290	Foreland
Jalauaca	Demini	23	530	0.1	10	5	1.5	430	0.46	402.8	170	Foreland
Fe e Esperanca	Mucajai	14	280	0.11	10	3	1.3	140	0.25	77.0	216	Craton
Caracarai	Branco	130	2900	1.12	7	10	1.1	575	1.80	183.4	416	Craton
Pontes e Lacerda	Guapore	3	60	0.02	80	1	1.1	760	0.18	3185.1	45	Craton
Pimenteiras	Guapore	54	530	0.05	6	3	1.3	760	0.51	1124.5	179	Craton
Pedras Negras	Guapore	110	910	0.05	7	8	1.4	760	0.50	1145.9	114	Craton
Guajara-Mirim	Mamore	589	8400	11.8	10	12	1.2	1700	89.56	32.3	1076	Andes
Porto Velho	Madeira	950	19000	96.6	7	10	1.2	3250	303.19	34.8	4178	Andes
Jiparana	Jiparana	33	720	0.27	30	1	1.2	680	5.04	91.8	326	Craton
Prainha (Velha)	Aripuana	109	3380	0.84	20	2	1.2	850	20.91	34.6	497	Craton
Fazenda Vista Alegre	Madeira	1300	31000	76.	5	7	1.2	3250	779.04	13.6	5051	Andes
Obidos	Amazonas	4600	170000	171	1	40	1.1	4900	705.87	34.0	6783	Andes
Barragem—Conj. 04	Curua-Una	14	180	0.02	9	1	1.3	460	0.47	453.2	200	Craton

4. Remote sensing reveals widespread extent of Amazonian dark earth

Abstract

Amazonian dark earth (ADE) is anomalously fertile and carbon-rich soil created by past inhabitants of the Amazon basin. Despite its importance to cultural heritage and carbon sequestration, efforts to systematically map the distribution and extent of ADE are hindered by difficulties of access and field excavation. To circumvent these barriers, we use a machine-learning classifier and remote sensing to predict the occurrence of ADE across the 26,000 km^2 Xingu Indigenous Territory (XIT). We use training data derived from field excavation and mapping as well as spectrally distinct vegetation patches. Combining these training data with a two-season Landsat 5 composite image and a random-forest classifier, we produce classification maps for the XIT with predicted locations of ADE. We find a strong correspondence between ADE locations and topography, with sites located along the edges of bluffs adjacent to river floodplains and tributary streams. We further estimate that the XIT may hold 7 Mt of anthropogenic carbon within ADE deposits.

4.1. Introduction

Amazonian dark earth (ADE), or *terra preta*, is a soil found throughout the Amazon basin, characterized by dark color, high organic and charcoal content, and elevated soil fertility compared to the typical extensively weathered and depleted tropical soils found in the region (Figure 4.1) (Glaser & Birk, 2012; Lehmann, Kern, Glaser, & Woods, 2003). The ubiquitous presence of ceramic fragments and other archaeological artifacts and the association of ADE deposits with archaeological sites suggests the formation of these soils by human activities; dated ADE deposits typically range from 500 BCE to 1500 CE (Neves, Petersen, Bartone, & Da Silva, 2003). Researchers have argued that the enhanced fertility of ADE was a key factor enabling the

development of large and complex pre-Columbian civilizations in the region, allowing greater crop productivity and thus population density than natural soils of the region (Denevan, 2004).

In addition to its putative role in supporting past population density, the continued presence of ADE today means that past human activities have sequestered carbon (C) in the soil for centuries. Soils globally are a major carbon reservoir containing ~3500 Pg C, approximately four times more than the atmosphere and six times more than terrestrial vegetation (Sanchez, 2019). Of this global stock, tropical soils represent ~800 Pg, but the long-term stability of tropical soil carbon is threatened both by increasing temperatures (Nottingham, Meir, Velasquez, & Turner, 2020) and by land-use change and deforestation (Damian et al., 2021; Gatti et al., 2021). Natural soils of the Amazon are typically low in C (Cerri, Bernoux, Arrouays, Feigl, & Piccolo, 2000), but ADE is substantially enriched above natural levels in SOC, and additionally features abundant charcoal content (Alho et al., 2019; Glaser, Balashov, Haumaier, Guggenberger, & Zech, 2000). These deposits may therefore represent a substantial carbon reservoir beyond natural soil (Sombroek, Ruivo, Fearnside, Glaser, & Lehmann, 2003). However, the total inventory of this additional anthropogenic carbon stock is unknown due to the lack of constraints on the spatial extent and abundance across the region.

Figure 4.1: Amazonian Dark Earth. A: Soil pit through an ADE deposit at center of Akagahütü archaeological site, showing characteristic dark color, ceramic fragments, and charcoal. B: Soil pit at periphery of Akagahütü, showing extensive chemical weathering typical of Amazon soils. C: Database of reported locations of ADE (WinklerPrins & Aldrich, 2010), showing distribution throughout Amazonia, with concentrations along major rivers and roads. Photographs in A and B by Morgan Schmidt.

Known deposits of ADE are typically found and studied by labor-intensive fieldwork and excavation. While this approach yields valuable information about the detailed composition and spatial structure of ADE, it is not well-suited to systematic surveys of large regions due to the logistical impracticality and difficulties of access. As a result, compilations of reported ADE locations display clear sampling biases, with concentrations in well-studied areas and along major roads and rivers that provide access for researchers (Figure 4.1C). Reported deposits likely omit the large majority of all ADE deposits, in regions that have not been surveyed for their presence (Figure 4.1X) (McMichael et al., 2014; WinklerPrins & Aldrich, 2010). Attempts to analyze the spatial distribution or overall extent of ADE from such databases are inherently hampered by the incompleteness of reported data. One past study used a maximum entropy model to estimate the probability of finding ADE across the region using a database of known locations and a suite of environmental variables, such as topography and climate (McMichael et al., 2014). However this approach does not attempt to identify specific instances of ADE, only locations where it is likely to be found based on circumstantial environmental evidence.

Modern satellite remote sensing datasets feature global coverage at high spatial and temporal resolution and have been used for land-cover classification at large scales (Kim et al., 2014; Pekel, Cottam, Gorelick, & Belward, 2016); analysis of remote sensing imagery may thus offer the opportunity to detect and map ADE deposits without the sampling biases inherent to on-the-ground field study. While typical remote-sensing modalities cannot directly image the soil due to dense vegetation and tree canopy cover, forest growing on ADE has observable differences from that growing on unmodified soil due to differences in soil nutrients or other properties, which manifests as a detectable difference in satellite imagery (Braswell et al., 2012). In this study, we apply a machine-learning classifier to detect and classify forest growing on

ADE deposits from satellite remote-sensing imagery, using labeled training data assembled from ground-truthed field observation in the Xingu Indigenous Territory (XIT). We use the resulting classification map to identify ADE deposits and analyze the spatial distribution and overall areal abundance of ADE within the XIT.

4.2. Materials and Methods

4.2.1. Study region

We focus our analysis on the Xingu Indigenous Territory (XIT) in the upper Xingu River basin in the southeastern Amazon, Mato Grosso State, Brazil (Figure 4.2). The geologic substrate of this region is the Tertiary Ronuro Formation, consisting of poorly consolidated Tertiary terrestrial sand (Bizzi, Schobbenhaus, Vidotti, & Gonçalves, 2003). Fluvial and hillslope processes have shaped the landscape into a mosaic of meandering rivers and adjacent floodplains dissecting the *terra firme* forested uplands, characterized by gently-curving parabolic hillslopes with a relief of 30-50 m above the floodplain (Figure 4.2A). The climate of the region is classified as "tropical savanna," with a mean annual temperature of 25° C and 1800 mm/yr of precipitation, concentrated in the wet season between October and April (Fick & Hijmans, 2017). The XIT is located near the southern boundary of the Amazon rainforest, along the forest-savanna transition. During the 21st century, the forest of the XIT has been extensively affected by wildfires that have burned much of the region (Brando et al., 2014). The unprotected region outside the XIT has been extensively deforested for agriculture in recent decades; the XIT preserves a fragment of mostly intact forest under indigenous management (Coe et al., 2017).

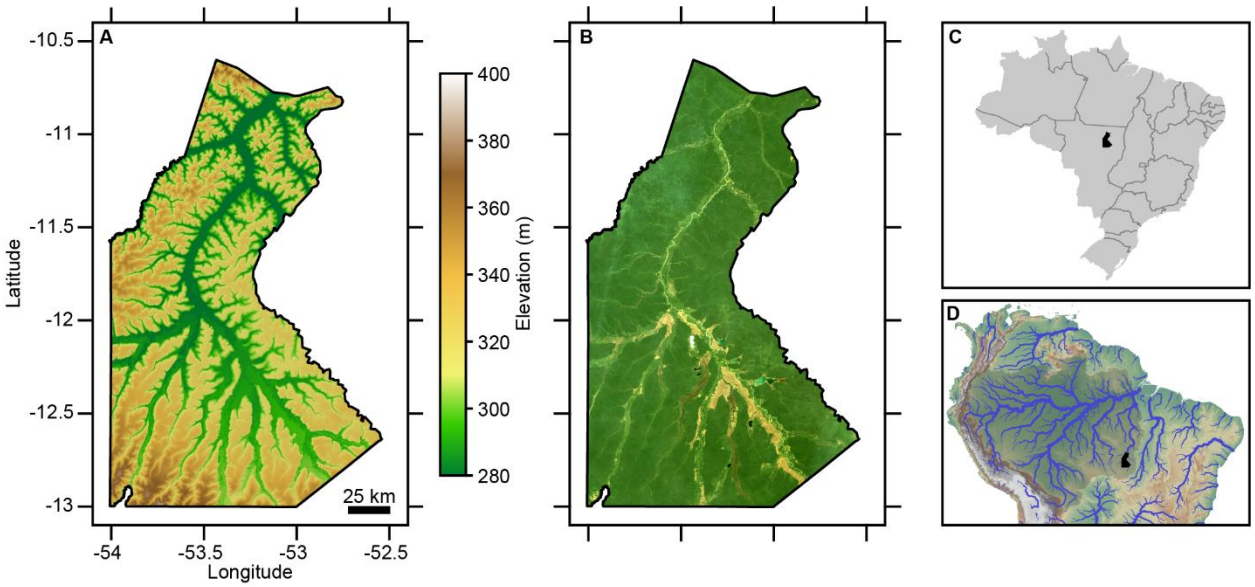

Figure 4.2: Xingu Indigenous Territory. A: Topography of XIT, showing flat floodplains of the upper Xingu River basin dissecting uplands. Elevation data from MERIT DEM (Yamazaki et al., 2017). B: Landsat composite image of XIT (1985-1990). C, D: Political and geographic context. Dark shaded region in (D) shows Amazon River basin. Hydrography data from HYDROSheds (Lehner, Verdin, & Jarvis, 2008).

Culturally, the XIT is inhabited by over 5000 residents from 14 ethnic groups that together comprise the Xinguano Nation. We use ground-truthed training data from the Kuikuro community and their traditional territory, which features well-studied archaeological sites on uplands adjacent to the Culuene (Xingu) and Angahuku Rivers. These sites demonstrate a large, complex, and densely settled society in the past; radiocarbon dates of ancient sites range from 90-160 B.C.E. to modern, primarily between 950 and 1650 C.E (Heckenberger et al., 2003). Archaeological and ethnographic research has documented culturally continuous occupation for centuries up to the present. Studied archaeological sites and ADE deposits are typically under forest cover on uplands near the floodplain, although some sites have been deforested for small-scale agriculture.

4.2.2. Training data

We used two training datasets of labeled polygons for four land-cover categories: forest (on unmodified soil), ADE, bare earth/open ground, and wetlands (Figure 4.3). The first is derived from field excavations and mapping of archaeological sites for the ADE category (Schmidt et al., 2014). Polygons for the other three categories were drawn from satellite imagery based on a qualitative land-cover assessment. Unmodified forest polygons were drawn in the interior of uplands in areas with no indications forest disturbance and distant from bluffs where known archaeological sites occur. Bare ground polygons correspond to cleared areas, typically in or adjacent to modern villages. Wetland polygons were drawn in topographic lows between uplands, although most of the area represented by these are masked out from the imagery for analysis by our floodplain mask (see next section). This dataset consists of 60 polygons ranging from 4,000 to 3,000,000 m^2 in area, with an average of 450,000 m^2.

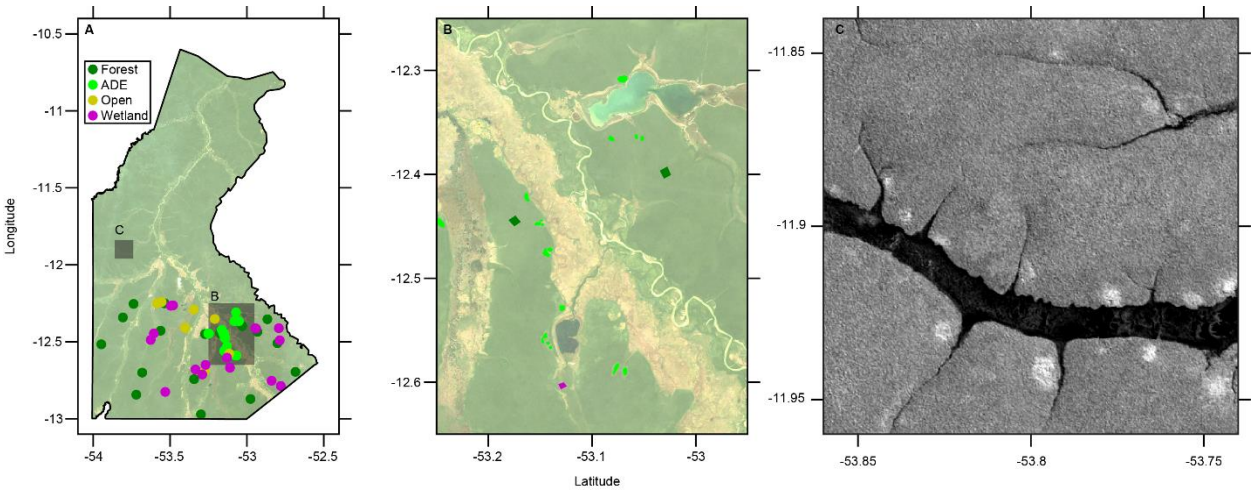

Figure 4.3: Training data. A: Locations of 60 training data polygons for ground-truthed dataset, colored by category (see legend). B: Inset showing spatial distribution of mapped ADE sites in the Kuikuro territory. Colors are the same as in A; location of inset shown by shaded rectangle in A. C: NIR (band 4) showing distinct bright patches that represent likely ADE deposits; location of inset shown by shaded rectangle in A. Satellite imagery is Landsat-5 composite, as described in the text.

For the second dataset, we instead used polygons for the ADE class drawn around distinct bright patches of forest in the near-infrared (NIR) (Landsat band 4) that likely represent ADE deposits that have been relatively undisturbed for centuries, in contrast to the recently cultivated ADE deposits in the Kuikuro territory (Figure 4.3C). While we do not have direct field evidence for ADE in most of these patches, several of them are associated with known archaeological sites, and their spatial pattern is consistent with patterns of known sites elsewhere in the XIT. We manually drew polygons around 45 of these patches and 12 areas of nearby unaltered forest, and used the same polygons for open and wetland as in the first dataset.

4.2.3. Imagery sources

Due to the recent modification of the forest landscape by fires, we used Landsat 5 satellite imagery from 1985-2005 before significant burning of upland forest. We use the atmospherically-corrected surface reflectance dataset from the Enhanced Thematic Mapper sensor, which consists of six reflectance bands in the visible and shortwave infrared (450-2350 nm), as well as a brightness temperature band computed from longwave infrared (10.4-12.5 μm). To leverage seasonal differences in vegetation, we computed two composite images over the XIT in Google Earth Engine: one for the wet season (October 1 – March 30) and one for the dry season (May 1 – August 31). To do this, we calculated the pointwise median of all cloud-free pixels for each season between January 1, 1985 and January 1, 2005 on a 30 m UTM grid (zone 22S); the cloud mask was taken from the associated quality attribute layer for each image. Over the XIT, the median number of cloud-free measurements at each point which we use to compute the composite image is 84 for the dry season and 20 for the wet season, with a maximum of 219 and 51 and a minimum of 77 and 7. Since our analysis focuses on the forest uplands, we mask out the floodplains to reduce the overall variation in the image. We computed a floodplain mask

using a topographic threshold of 6 m above the closest channel with drainage area greater than 30 km^2, using topographic and hydrographic data from MERIT Hydro (Yamazaki et al., 2019, 2017). We combined the two images (wet and dry season composite) into a single 14-band image which we used for the classification.

4.2.4. Classification algorithm

We used a random forest classifier in Google Earth Engine (Belgiu & Dra, 2016; Breiman, 2001; Pal, 2005). This method is an ensemble learning method that uses a set of many decision trees and takes the mode of the results; we use 100 trees for each classifier instance. This ensemble approach improves the tendency to overfit the training data for a single decision tree. The random forest classifier is a pixel-wise algorithm without spatial relationships between data points (pixels). For training, the classifier takes as input a dataset where each data point consists of the values of the imagery bands plus the categorical label for the corresponding classification. The trained classifier can then be applied to any image consisting of the same bands as the input training data; we applied the classifier to the XIT composite image. The result of this process is a 4-class categorical classification image over the XIT, at the same resolution as the Landsat imagery (30 m).

As a result of the point-based nature of the classifier and the noise inherent to remote sensing imagery, the resulting classification image exhibits pixel-scale noise that likely does not reflect true short-wavelength features. To reduce this noise and focus on the larger-scale features, we applied a focal mode filter to the raw image to produce a cleaned classification image. At each point, this filter takes the mode of all pixels within a circular window of radius 2 pixels. The final result of this filtering step is a 4-class categorical classification image over the XIT, with pixel-scale noise removed.

4.2.5. Accuracy assessment

To assess the accuracy of the classification algorithm we used a partitioning method, in which we randomly divided the training data into a training set, which we input to train the classifier, and a validation set that we withhold from training, which we used to measure the success of the classifier in reproducing our assigned categorical labels. We divided the polygons using a random number generator for each polygon: polygons whose random number is less than 0.8 are assigned to the training set, and the remainder compose the validation set, such that on average 80% of polygons were used for training and 20% for validation. Given the small number of polygons in our training dataset relative to typical machine-learning applications, we iterated this process repeatedly, using a different random split to train and validate the classifier each iteration. Each iteration produces an accuracy matrix comparing the assigned class from the training data to the output classification; we summed the resulting accuracy matrices to yield a cumulative accuracy matrix across 100 iterations. To compute our final classification map, we used all of the training polygons to train the classifier.

4.3. Results

4.3.1. Accuracy of classifier

We show the cumulative accuracy matrix from 100 iterations of training and validating the classifier in Table 4.1, for the cleaned classification image using the ground-truthed training data. The accuracy matrix has rows corresponding to the input class (from our training polygons) and columns corresponding to the output classification. Entries along the diagonal correspond to correct identification by the classifier; entries off the diagonal are errors. For forest on unmodified soils, we observe that the classifier correctly classifies 93% percent correctly, with

nearly all of the rest classified as ADE. Since ADE is our variable of interest, we consider the the forest pixels incorrectly classified as ADE to be false positives (red shading, first row, second column). For known ADE, we observe that the classifier correctly identifies 88% of pixels (true positives, green shading), misidentifying the rest as unmodified forest (second row, first column); we consider this error to be false negatives (blue shading). However, given the much larger area of the forest polygons compared to the ADE polygons, the number of pixels represented by false positives is of the same order of magnitude as the false negatives. The poor accuracy of the wetland class is because most of the wetland area is masked out by the floodplain mask; the misidentified pixels represent only a small fraction of the total. In Table 4.2 we show the cumulative accuracy matrix for 100 iterations using the NIR-derived training data. We observe substantially improved accuracy, particularly with regards to the false positive rate

	Pixels				***Percentage***			
	Forest	**ADE**	**Open**	**Wetland**	**Forest**	**ADE**	**Open**	**Wetland**
Forest	309620	22974	0	0	93.1%	6.9%	0.0%	0.0%
ADE	12185	88934	0	0	12.1%	87.9%	0.0%	0.0%
Open	0	110	3490	0	0.0%	3.1%	96.9%	0.0%
Wetland	28	98	0	0	22.2%	77.8%	0.0%	0.0%

Table 4.1: Cumulative accuracy matrix for ground-truthed training data. Rows correspond to the input classes; columns to the output classification. The results are given in terms of pixels (left), and percentage (right) normalized by rows such that each row adds up to 100%. Green shaded cells are true positives (ADE correctly identified), red shaded cells are false positives (forest identified as ADE), and blue shaded cells are false negatives (ADE identified as forest).

	Pixels				***Percentage***			
	Forest	**ADE**	**Open**	**Wetland**	**Forest**	**ADE**	**Open**	**Wetland**
Forest	2525974	11390	0	0	99.6%	0.4%	0.0%	0.0%
ADE	29701	445718	0	0	6.2%	93.8%	0.0%	0.0%
Open	115	62	3140	0	3.5%	1.9%	94.7%	0.0%
Wetland	105	15	0	0	87.5%	12.5%	0.0%	0.0%

Table 4.2: Cumulative accuracy matrix for training data derived from NIR imagery. Table format same as Table 4.1.

(forest pixels misidentified as ADE). The false positive rate is 0.4%, and the false negative rate is 6.2%.

4.3.2. Classification of XIT

We show classification maps produced by the classifier using the ground-truthed training data in Figure 4.4 and using the NIR-derived training data in Figure 4.5. The classification map using the ground-truthed dataset predicts 2480 km^2 of ADE across the XIT; using the NIR-derived training data predicts 710 km^2 of ADE in the region.

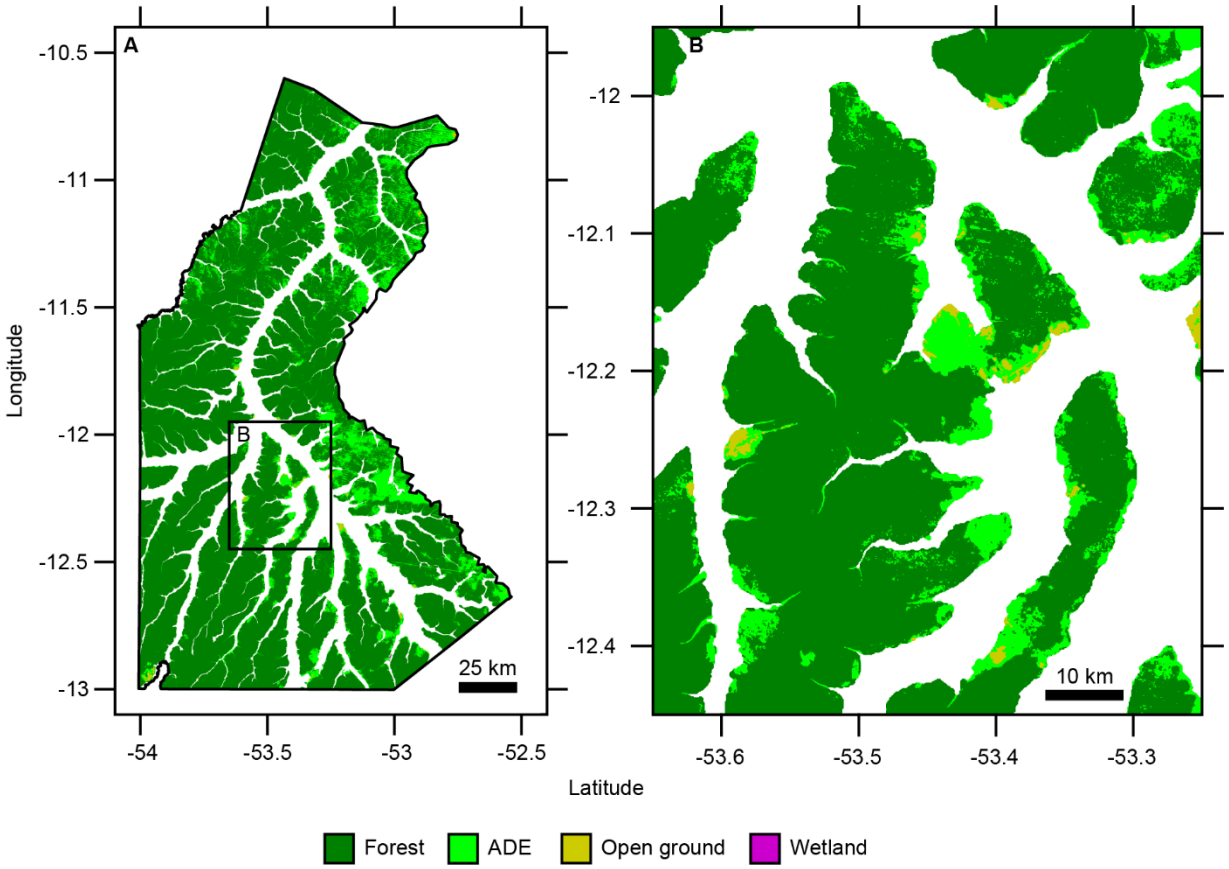

Figure 4.4 A: Classification map of XIT using ground-truthed data, with land cover classes colored as shown in legend. White regions within XIT boundary correspond to masked floodplain areas. B: Inset of central XIT, showing local patterns of ADE deposits.

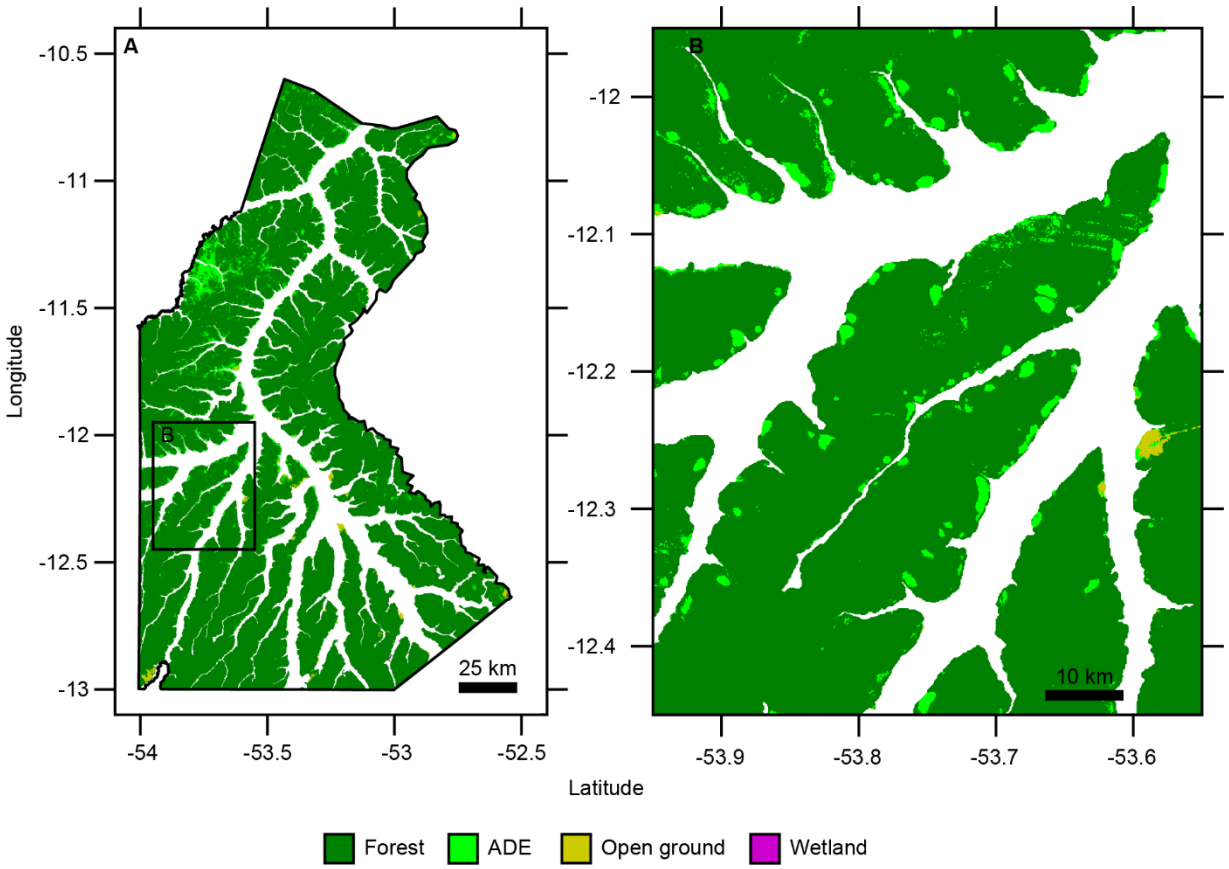

Figure 4.5 A: Classification map of XIT using NIR-derived data, with land cover classes colored as shown in legend. White regions within XIT boundary correspond to masked floodplain areas. B: Inset of central XIT, showing local patterns of ADE deposits.

4.4. Discussion

4.4.1. Comparison of the two results

Our two training datasets yield different results in several ways. The classifier gives substantially higher accuracy using the NIR-derived dataset than using the ground-truthed dataset. This is unsurprising, since the ADE polygons in the NIR-derived dataset were chosen for their distinct characteristics in remote sensing imagery, rather than from direct observations of the soil. As a result, the ADE training data have a narrower distribution in the imagery space. The results using the ground-truthed data predict 3.5 times more ADE in the XIT than using the

NIR-derived dataset, this may be in large part due to the higher false positive rate. The classification map using the ground-truthed data shows large swaths of predicted ADE that may not be realistic, and further shows obvious artifacts from the satellite imagery, such as striping and edge effects along Landsat tile boundaries.

The ADE sites used for the ground-truthed data have been recently cultivated (within the past century) by the Kuikuro. Conversely, the NIR-derived polygons elsewhere in the XIT likely represent regions that were depopulated following colonialism and population declines, and have not experienced substantial human land use since abandonment. As a result of these land use differences and resulting vegetation differences, the two types of ADE deposits show distinct remote sensing signatures. The deposits near the Kuikuro village are noticeably lighter than surrounding forest in the visible bands, but darker in the NIR. The patches elsewhere are not substantially different from the surrounding forest in the visible wavelengths, but are markedly brighter in the NIR, and to a lesser extent short-wave infrared (band 5). As a result of these differences, the classification maps produced with each predict different patterns of ADE. Beyond apparent noise/false positives in the east and northeast of the XIT, the map using ground-truthed data largely predicts ADE deposits near the Kuikuro village and the archaeological sites used for training data. Conversely, the map using NIR-derived polygons largely omits the known archaeological sites near the Kuikuro village that have been recently cultivated, but identifies many sites in the north and west of the XIT not identified by the ground-truthed data.

4.4.2. Spatial patterns and relationships with landscape structure

Similarly to the well-studied sites in the Kuikuro territory (Heckenberger et al., 2003), both classification maps predict that ADE deposits are primarily located along the edges of the

uplands, near the slope down to the floodplain (Figure 4.4B, 4.5B). Many predicted ADE regions are located where a small tributary joins the floodplain a larger river, in some cases spanning both sides of the tributary. The predicted deposits are largely 50-200 ha in size, which is comparable to the size of the well-studied sites. This pattern is consistent throughout the XIT, and strongly suggests an environmental preference for ancient settlements near the interface of the uplands and the floodplains. This pattern has been observed throughout Amazonia (Denevan, 1996). McMichael et al. (2014) used a maximum-entropy model based on a a database of known ADE locations across the Amazon and environmental data such as topography and climate, and predicted that ADE is most likely to be found near rivers and bluffs. Our analysis uses remote sensing data, rather than circumstantial evidence, to predict the geographic location and extent of discrete ADE deposits, and demonstrates that the ADE sites of the XIT, even those unmapped and unstudied, are near-universally found along bluff edges.

As discussed in Chapter 3 of this thesis, much of the Amazon lowlands are characterized by clear bluffs separating floodplains from uplands and terraces, and in many places this is the result of a rapid fluvial response to late Quaternary climate change since deglaciation. The close correspondence between the landscape structure and patterns of human settlement and land use is an example of the complex ways in which geologic factors and environmental history can influence human society.

4.4.3. Spatial extent and implications for carbon storage

Past research has demonstrated organic carbon densities in the upper 1 m of soil of 10-25 kg/m^2 for ADE (Alho et al., 2019; Schmidt et al., 2021). In addition to the organic content, charcoal may make up 30-50% of the carbon in these soils (Glaser et al., 2000). For comparison, typical latosols of the region have average carbon densities of 7.5 kg/m^2 (Cerri et al., 2000). If

we take as a crude approximation that ADE on average contains 10 kg/m^2 additional anthropogenic C beyond the natural abundance, then a 100 ha ADE deposit (typical size of studied and predicted sites) contains 10,000 tonnes of anthropogenic C. From our cleaned classification image using the NIR-derived data, we estimate 710 km^2 of ADE within the XIT. The XIT is 26500 km^2 in total with 20000 km^2 of uplands, meaning that 2.7% of the total area and 3.6% of the upland area is composed of ADE. Applying the same estimate of ADE carbon abundance gives 7 Mt of anthropogenic C sequestered in ADE in the XIT, comparable to the annual CO_2 emissions of Honduras (Climate Watch, n.d.). This estimate represents a more conservative assessment of the areal extent of ADE than the results using the ground-truthed data, which likely overpredict the abundance. The low false positive rate of the NIR-derived classifier means that this estimate is likely reasonably reliable for the areal extent of ADE in the XIT.

4.4.4. Implications for Amazonia

The Amazon rainforest is 5,500,000 km^2. If the entire region has a comparable fraction of ADE deposits, this would mean 150,000 km^2 of ADE, an area the size of Illinois, and potentially 1.5 Pg of anthropogenic carbon. This quantity is comparable to the annual CO_2 emissions of the USA, and about 1% of the entire above- and below-ground organic carbon mass of the entire Amazon (Gatti et al., 2021). However, there is substantial uncertainty as to whether it is reasonable to extrapolate values for the XIT to the entire Amazon. While the upper Xingu region was densely occupied in the past with major human alteration of the landscape (Heckenberger et al., 2003), it is unclear whether such dense habitation occurred throughout the Amazon basin. Evidence suggests that some regions, particularly along major rivers were more densely occupied and for a longer duration than the upper Xingu basin and feature substantially more

extensive and fertile ADE, but other regions were likely more sparsely settled. Nevertheless, ADE is widespread throughout the region (McMichael et al., 2014; WinklerPrins & Aldrich, 2010).

McMichael et al. (2014) produce a likelihood map for finding ADE throughout the Amazon, and predict a high likelihood in many, although not all, parts of the region. ADE thus represents a substantial carbon sink beyond what is typical of tropical soils, even if 1.5 Pg may be an overestimate. Moreover, the practices used to create ADE in the past could be applied in the present to sequester additional carbon in tropical soils (Schmidt et al., 2021).

4.4.5. Future directions

With a few exceptions, the bright patches in the NIR that we use in our analysis do not have confirmed ADE from field investigation. As a result, our use of these features as putative ADE deposits is speculation. However, given their distinct signature and clear distribution, it would be straightforward to investigate the soil properties of these locations to test this hypothesis. If these sites are confirmed to be ADE deposits, then the classification map produced using the NIR-derived training data is likely the most reliable estimate of the locations of ADE in the XIT.

The random forest classifier we use does not consider the spatial relationships among pixels when assigning a class designation. Since ADE occurs in discrete clusters, one potential improvement would be to use a fully convolutional neural net that performs object-based classification. Such an algorithm would likely reduce the short-wavelength noise that the random forest classifier produces.

While this study demonstrates the potential usefulness of remote sensing and machine learning for ADE identification within a region, the XIT is only a small part of the Amazon

rainforest. Due to regional variations in vegetation and forest ecology, a single trained classifier will not be applicable over the entire region, and a classification algorithm must be trained on data within the region of interest to be analyzed. The upper Xingu basin is located near the forest-savanna boundary in the southern Amazon (Brando et al., 2014). This transitional ecosystem may be particularly sensitive to changes in soil properties or moisture such as result from ADE, making the XIT an ideal test case for the detection of ADE through remote sensing of vegetation.

4.5. Conclusions

ADE is an important part of Amazonian cultural heritage and potentially a major carbon reservoir. Remote sensing imagery and machine learning techniques offer powerful tools to map the extent and distribution of ADE deposits beyond what is practical through field methods. We demonstrate the applicability of ADE detection from remote sensing in the XIT, and find a strong correspondence between the topography of the region and patterns of past human settlement and land use, with a clear preference for the edges of uplands adjacent to river floodplains and tributary streams. Our systematic analysis thus confirms and extends prior studies based on local field research. We also use our results to show that ADE may potentially represent a large carbon sink through past human action, sequestered to the present within the soil.

Acknowledgments

Many have contributed to making this research possible. Michael Heckenberger has led archaeological research in the Upper Xingu since 1994 in partnership with the Kuikuro

indigenous community. Morgan Schmidt compiled training data and contributed to interpretations of the results. The Kuikuro Indigenous Association of the Upper Xingu (Associação Indígena Kuikuro do Alto Xingu (AIKAX)) authorized the research and owns the intellectual property including all data, images, and maps. Chief Afukaka has been fundamental in supporting the archaeological research and many in the Kuikuro community have contributed to field data collection over the years including Tabata, Yumu, Laqui, Kagito, Kamasinua, Dunga, Anselmo, Takumã, Kumessi, Hulke, Jahila, Uga, Wate, Daniel, and others. Other colleagues whose contributions to research and field data collection must be acknowledged include Carlos Fausto, Bruna Franchetto, Joshua Toney, Christian Russell, Jennifer Watling, Wetherbee Dorshow, Helena Lima, and Bruno Moraes. Luiz Leal Gomez and Josh Himmelstein contributed to the classification algorithms. We acknowledge support from MIT Abdul Latif Jameel Water and Food Systems Lab (J-WAFS), MIT-Air Force AI Accelerator, and NASA Earth and Space Science Fellowship (to SLG).

References

Alho, C. F. B. V., Samuel-Rosa, A., Martins, G. C., Hiemstra, T., Kuyper, T. W., & Teixeira, W. G. (2019). Spatial variation of carbon and nutrients stocks in Amazonian Dark Earth. *Geoderma*, *337*(September 2018), 322–332. https://doi.org/10.1016/j.geoderma.2018.09.040

Belgiu, M., & Dra, L. (2016). Random forest in remote sensing: A review of applications and future directions. *ISPRS Journal of Photogrammetry and Remote Sensing*, *114*, 24–31. https://doi.org/10.1016/j.isprsjprs.2016.01.011

Bizzi, L. A., Schobbenhaus, C., Vidotti, R. M., & Gonçalves, J. H. (2003). *Geologia, Tectônica e*

Recursos Minerais do Brasil: texto, mapas e SIG. Brasilia: CPRM-Serviço Geológico do Brasil.

Brando, P. M., Balch, J. K., Nepstad, D. C., Morton, D. C., Putz, F. E., Coe, M. T., … Soares-Filho, B. S. (2014). Abrupt increases in Amazonian tree mortality due to drought-fire interactions. *Proceedings of the National Academy of Sciences of the United States of America*, *111*(17), 6347–6352. https://doi.org/10.1073/pnas.1305499111

Braswell, B. H., Palace, M. W., Bush, M. B., Neves, E. G., Mcmichael, C. H., Czarnecki, C., … Raczka, M. (2012). Detection of Amazonian Black Earth Sites using Hyperspectral Satellite Imagery. In *AGU Fall Meeting Abstracts*.

Breiman, L. (2001). Random forests. *Machine Learning*, *45*(1), 5–32.

Cerri, C. C., Bernoux, M., Arrouays, D., Feigl, B. J., & Piccolo, M. C. (2000). Carbon Stocks in Soils of the Brazilian Amazon. In R. Lal, J. M. Kimble, & B. A. Stewart (Eds.), *Global climate change and tropical ecosystems* (pp. 33–50). Boca Raton: CRC Press.

Climate Watch. (n.d.). Historical GHG Emissions. Retrieved July 16, 2021, from https://data.worldbank.org/indicator/EN.ATM.CO2E.KT

Coe, M. T., Brando, P. M., Deegan, L. A., Macedo, M. N., Neill, C., & Silverio, D. V. (2017). The forests of the Amazon and Cerrado moderate regional climate and are the key to the future. *Tropical Conservation Science*, *10*, 1940082917720671.

Damian, J. M., Durigan, M. R., Cherubin, M. R., Maia, S. M. F., Ogle, S. M., de Camargo, P. B., … Cerri, C. E. P. (2021). Deforestation and land use change mediate soil carbon changes in the eastern Brazilian Amazon. *Regional Environmental Change*, *21*(3), 1–12.

Denevan, W. M. (1996). A bluff model of riverine settlement in prehistoric Amazonia. *Annals of the Association of American Geographers*, *86*(4), 654–681. https://doi.org/j.1467-

8306.1996.tb01771.x

Denevan, W. M. (2004). Semi-intensive pre-European cultivation and the origins of anthropogenic dark earths in Amazonia. In B. Glaser & W. I. Woods (Eds.), *Amazonian dark earths: explorations in space and time* (pp. 135–143). Springer.

Fick, S. E., & Hijmans, R. J. (2017). WorldClim 2: new 1-km spatial resolution climate surfaces for global land areas. *International Journal of Climatology*, *37*(12), 4302–4315.

Gatti, L. V, Basso, L. S., Miller, J. B., Gloor, M., Domingues, L. G., Cassol, H. L. G., … Peters, W. (2021). Amazonia as a carbon source linked to deforestation and climate change. *Nature*, *595*(7867), 388–393.

Glaser, B., Balashov, E., Haumaier, L., Guggenberger, G., & Zech, W. (2000). Black carbon in density fractions of anthropogenic soils of the Brazilian Amazon region. *Organic Geochemistry*, *31*, 669–678.

Glaser, B., & Birk, J. J. (2012). State of the scientific knowledge on properties and genesis of Anthropogenic Dark Earths in Central Amazonia (terra preta de índio). *Geochimica et Cosmochimica Acta*, *82*, 39–51. https://doi.org/10.1016/j.gca.2010.11.029

Heckenberger, M. J., Kuikuro, A., Kuikuro, U. T., Russell, J. C., Schmidt, M., Fausto, C., & Franchetto, B. (2003). Amazonia 1492: Pristine forest or cultural parkland? *Science*, *301*(5640), 1710–1714. https://doi.org/10.1126/science.1086112

Kim, D.-H., Sexton, J. O., Noojipady, P., Huang, C., Anand, A., Channan, S., … Townshend, J. R. (2014). Global, Landsat-based forest-cover change from 1990 to 2000. *Remote Sensing of Environment*, *155*, 178–193.

Lehmann, J., Kern, D. C., Glaser, B., & Woods, W. I. (Eds.). (2003). *Amazonian Dark Earths: Origin Properties Management*. New York: Kluwer Academic Publishers.

https://doi.org/10.1007/1-4020-2597-1

Lehner, B., Verdin, K., & Jarvis, K. (2008). New global hydrography derived from spaceborne elevation data. *Eos, Transactions, AGU*, *89*(10), 93–94.

McMichael, C. H., Palace, M. W., Bush, M. B., Braswell, B. H., Hagen, S., Neves, E. G., … Czarnecki, C. (2014). Predicting pre-Columbian anthropogenic soils in Amazonia. *Proceedings of the Royal Society B: Biological Sciences*, *281*(1777), 23–28. https://doi.org/10.1098/rspb.2013.2475

Neves, E. G., Petersen, J. B., Bartone, R. N., & Da Silva, C. A. (2003). Historical and socio-cultural origins of Amazonian dark earth. In J. Lehmann, D. C. Kern, B. Glaser, & W. I. Woods (Eds.), *Amazonian Dark Earths: Origin Properties Management* (pp. 29–50). New York: Kluwer Academic Publishers.

Nottingham, A. T., Meir, P., Velasquez, E., & Turner, B. L. (2020). Soil carbon loss by experimental warming in a tropical forest. *Nature*, *584*(7820), 234–237.

Pal, M. (2005). Random forest classifier for remote sensing classification. *International Journal of Remote Sensing*, *26*(1), 217–222. https://doi.org/10.1080/01431160412331269698

Pekel, J.-F., Cottam, A., Gorelick, N., & Belward, A. S. (2016). High-resolution mapping of global surface water and its long-term changes. *Nature*, *540*(7633), 418–422.

Sanchez, P. A. (2019). *Properties and Management of Soils in the Tropics*. Cambridge University Press.

Schmidt, M. J., Goldberg, S. L., Heckenberger, M. J., Fausto, C., Franchetto, B., Watling, J., … Perron, J. T. (2021). Intentional creation of carbon-rich dark earth soils in the Amazon. *Nature (in Prep)*.

Schmidt, M. J., Py-Daniel, A. R., de Paula Moraes, C., Valle, R. B. M., Caromano, C. F.,

Texeira, W. G., … Heckenberger, M. J. (2014). Dark earths and the human built landscape in Amazonia: a widespread pattern of anthrosol formation. *Journal of Archaeological Science*, *42*, 152–165.

Sombroek, W., Ruivo, M. D. L., Fearnside, P. M., Glaser, B., & Lehmann, J. (2003). Amazonian dark earths as carbon stores and sinks. In *Amazonian dark earths* (pp. 125–139). Springer.

WinklerPrins, A. M. G. A., & Aldrich, S. P. (2010). Locating Amazonian dark earths: creating an interactive GIS of known locations. *Journal of Latin American Geography, 9*(3), 33–50. https://doi.org/10.1353/lag.2010.0029

Yamazaki, D., Ikeshima, D., Sosa, J., Bates, P. D., Allen, G. H., & Pavelsky, T. M. (2019). MERIT Hydro: A High-Resolution Global Hydrography Map Based on Latest Topography Dataset. *Water Resources Research*, *55*(6), 5053–5073. https://doi.org/10.1029/2019WR024873

Yamazaki, D., Ikeshima, D., Tawatari, R., Yamaguchi, T., O'Loughlin, F., Neal, J. C., … Bates, P. D. (2017). A high-accuracy map of global terrain elevations. *Geophysical Research Letters*, *44*(11), 5844–5853. https://doi.org/10.1002/2017GL072874